Universität der Bundeswehr München

A continuum damage model for anisotropic ductile metals based on experiments and numerical simulations

Sanjeev Koirala

Vollständiger Abdruck der von der Fakultät für Bauingenieurwesen und Umweltwissenschaften der Universität der Bundeswehr München zur Erlangung des akademischen Grades eines

Doktor-Ingenieurs (Dr.-Ing.)

genehmigten Dissertation.

Vorsitzender:	Prof. Dr.-Ing. Josef Kiendl, UniBw München
Gutachter/in:	1. Prof. Dr.-Ing. habil. Michael Brünig, UniBw München
	2. Prof. Dr.-Ing. habil. Dr. h.c. Holm Altenbach, Otto-von-Guericke-Universität, Magdeburg
	3. Prof. Dr.-Ing. habil. Jörg Schröder, Uni DUE, Essen

Die Dissertation wurde am 18.03.2024 bei der Universität der Bundeswehr München eingereicht und durch die Fakultät für Bauingenieurwesen und Umweltwissenschaften am 13.07.2024 angenommen. Die mündliche Prüfung fand am 14.08.2024 statt.

sanjeev.koirala@unibw.de; koiralasanz@gmail.com

Universität der Bundeswehr München
Institut für Mechanik und Statik
Werner-Heisenberg-Weg 39
85579 Neubiberg
www.unibw.de/mechanik-und-statik

In loving memory of my father.

Abstract

The doctoral thesis centers on exploring the damage and failure behavior of anisotropic ductile metals through a combined approach of experimental and numerical analyses. The research involves a series of experiments with both uniaxially and biaxially loaded specimens, emphasizing different loading ratios and loading directions. Digital image correlation is used to analyze the strain fields in critical areas of the specimens, while scanning electron microscopy is employed to analyze fractured surfaces, providing insights into various damage mechanisms. The thermodynamically consistent anisotropic continuum damage model, developed by Brünig [22], is further enhanced to incorporate the influence of plastic anisotropy on the damage behavior. Hoffman yield criterion, taking strength-differential into account, is used to model the anisotropic plastic behavior of the investigated aluminum alloy sheets. Using this yield criterion, generalized anisotropic stress invariants along with the generalized stress triaxiality and the generalized Lode parameter are introduced to characterize the stress state in the anisotropic ductile metal.

Moreover, a damage criterion expressed in terms of the anisotropic stress invariants is proposed. To understand the effect of plastic anisotropy on damage evolution on the micro-level, numerical simulations of a unit-cell containing a spherical void are performed. With the help of micro-mechanical studies, the stress-state and loading direction dependent parameters are determined, which describe the evolution of macroscopic damage strains.

The constitutive relations of the proposed continuum damage model are implemented into the commercial software package Ansys Classic APDL through a user-defined subroutine (UMAT). This involves employing a numerical algorithm based on the inelastic predictor-elastic corrector approach. The results obtained from experiments are then compared with corresponding numerical simulations, demonstrating the utility of the experimental-numerical methodology in gaining insights into the impact of plastic anisotropy on ductile damage and fracture behavior.

Kurzfassung

In dieser Arbeit wird das Schädigungs- und Versagensverhalten anisotroper duktiler Metalle durch einen kombinierten Ansatz aus experimentellen und numerischen Analysen untersucht. Die Forschung umfasst eine Reihe von Experimenten mit einachsig und zweiachsig belasteten Proben, wobei unterschiedliche Belastungsverhältnisse und Belastungsrichtungen berücksichtigt werden. Mit Hilfe der digitalen Bildkorrelation werden die Dehnungsfelder in kritischen Bereichen der Proben analysiert, während die Rasterelektronenmikroskopie zur Analyse von Bruchflächen eingesetzt wird, was Einblicke in verschiedene Schädigungsmechanismen ermöglicht. Das thermodynamisch konsistente anisotrope Kontinuumsschädigungsmodell, das von Brünig [22] entwickelt wurde, wird erweitert, um den Einfluss der plastischen Anisotropie auf das Schädigungsverhalten einzubeziehen. Zur Modellierung des anisotropen plastischen Verhaltens der untersuchten Bleche aus einer Aluminiumlegierung wird das Hoffman-Fließkriterium verwendet, das unterschiedliches Verhalten bei Zug- und Druckbelastung berücksichtigt. Unter Verwendung dieses Fließkriteriums werden verallgemeinerte anisotrope Spannungsinvarianten sowie die verallgemeinerte Spannungstriaxialität und der verallgemeinerte Lode-Parameter eingeführt, um den Spannungszustand in dem anisotropen duktilen Metall zu charakterisieren.

Darüber hinaus wird eine Schädigungbedingung vorgeschlagen, die mit den anisotropen Spannungsinvarianten formuliert ist. Um die Auswirkungen der plastischen Anisotropie auf die Schädigungsentwicklung auf der Mikroebene zu untersuchen, werden numerische Simulationen mit repräsentativen Volumenelementen mit einer kugelförmigen Pore durchgeführt. Mit Hilfe dieser mikromechanischen Untersuchungen werden die vom Spannungszustand und von der Belastungsrichtung abhängigen Parameter bestimmt, die die Entwicklung der makroskopischen Schädigungsverzerrungen beschreiben.

Die konstitutiven Gleichungen des Kontinuumsschädigungsmodells werden in das kommerzielle Softwarepaket Ansys Classic APDL durch ein benutzerdefiniertes Unterprogramm (UMAT) implementiert. Dabei wird ein numerischer Algorithmus verwendet, der auf dem Ansatz des inelastischen Prädiktors und des elastischen Korrektors basiert. Die aus Experimenten gewonnenen Ergebnisse werden dann mit denen aus entsprechenden numerischen Simulationen

verglichen, um die Effektivität der experimentell-numerischen Methodik für die Gewinnung von Erkenntnissen über die Auswirkungen der plastischen Anisotropie auf das duktile Schädigungs- und Bruchverhalten zu demonstrieren.

Acknowledgments

This thesis is the result of my work as a scientific research assistant at the Universität der Bundeswehr München.

First of all I would like to express my sincere gratitude to Prof. Michael Brünig for providing me the opportunity to work as a research assistant. His continuous guidance and support have not only enabled me to excel in my scientific endeavors but have also contributed significantly to my personal development during this period.

I would also thank Prof. Holm Altenbach and Prof. Jörg Schröder for taking the time to review this thesis and Prof. Josef Kiendl for chairing the examination.

I also wish to extend my thanks to all my current and former colleagues, both in scientific and non-scientific roles, at the institute. I value the insightful discussions and the friendly atmosphere. Special appreciation goes to my esteemed colleagues, Dr. Steffen Gerke, Dr. Moritz Zistl and Dr. Zhichao Wei, for many scientific discussions, constructive feedback, and the enjoyable moments we've experienced together. I would also like to thank Wolfgang Saur (Institut für Werkstoffe des Bauwesens, BAU 3) for his invaluable support to conduct the experiments.

Finally, I express my heartfelt thanks to my mother, father (unfortunately no longer with us), and brother for their support, encouragement, and joy that they have brought into my life wherever I have been. My biggest thanks to my amazing wife and son for unwavering support, love, and understanding throughout this journey.

Contents

1 Introdcution

Recent technological advancements have led to the development of more advanced and sophisticated materials. These materials are not only required to meet strength and ductility standards but also need to be as lightweight as possible. Lightweight materials, such as aluminum and its alloys, are widely utilized in various fields including automotive, aerospace, building construction, and offshore platforms. This widespread usage is attributed to their favorable strength-to-density ratio, contributing to improved fuel efficiency. However, to fully realize their potential, it is crucial to comprehend their elastic-plastic, damage, and fracture behavior under various loading conditions. For instance, damage induced by deformation and load can adversely affect the stiffness of ductile metals [76, 78] or the failure of the entire structure due to the fatigue [89]. Therefore, it is imperative to carefully analyze the inelastic behavior of the material for accurate numerical modeling that can effectively describe the deformation and failure behavior of structures.

Puttick [93] conducted the experimental investigation of the ductile fracture process in metals in 1959. Furthermore, McClintock [82] developed a fracture criterion by studying the growth and coalescence of voids. Since then, numerous researchers have conducted studies to comprehend the damage processes that lead to ductile fracture in metals. It is well established that primary damage mechanism in ductile metals involves the nucleation, growth and coalescence of micro-defects, coupled with the subsequent development of macro-cracks leading to the complete failure. Moreover, ductile damage is characterized by the occurrence of significant plastic strains prior to the progression of damage [50].

In addition, it has been demonstrated that the plastic anisotropy in sheet metals is a consequence of the manufacturing processes. The plastic behavior of anisotropic ductile metals plays a significant role on the development of damage and the failure process as well as on the magnitude of the load at the fracture of the material. In this context, it is essential to systematically explore the plastic, damage and fracture behavior, as well as the failure mechanisms of specimens fabricated from anisotropic metals. This should be achieved through reproducible tests covering a broad range of relevant uniaxial and multiaxial loads. With these experimental findings, it becomes possible to develop phenomenological material models and conduct numerical simulations to predict the properties of materials under various loading conditions. This, in turn, facilitates the assessment of safety, service life, and load-bearing capacity of innovative structures in lightweight construction.

In this doctoral thesis, the primary focus is on further development and implementation of a phenomenological continuum damage model. The objective is to understand and characterize the damage and failure behavior of anisotropic ductile sheet metals, with a specific emphasis on plastic anisotropy. Moreover, a series of novel experiments is carried out to investigate the influence of material anisotropy, and the outcomes from the developed material model are validated against the experimental results.

1.1 Scientific background

The investigation of the origin and behavior of voids in various materials has been a significant focus of interest for more than five decades. In particular, this attention is driven by the importance of understanding the impact of void growth leading to the material failure. This section provides an overview of scientific work on the deformation and damage behavior of ductile metals. First, the experimental findings of micro-mechanical damage mechanisms are summarized and corresponding constitutive modeling approaches are presented. Subsequently, plastic anisotropy and its influence on the damage and failure behavior are discussed in particular. This overview is followed by the specific objectives of the work.

1.1.1 Damage mechanisms in ductile metals

Fig. 1.1 illustrates X-ray tomography images of a round notched bar captured at various stages of tensile loading [92]. In the initial stage (Fig. 1.1(a)), numerous voids of varying shapes and sizes are dispersed. Upon further plastic deformation, voids enlarge, and a cluster of voids forms, resulting in coalescence as can be observed in Fig. 1.1(c). Eventually, a macro-crack is generated at a certain point (Fig. 1.1(d)). Similar investigations have been performed in [60, 80, 115] to study the mechanism of pore growth and coalescence under tensile stress. Furthermore, extensive research has been conducted on ductile damage under shear loading [1, 108]. Voids nucleate due to the detachment of the ductile matrix from the second-phase particles, leading to the rotation and elongation of these particles and the development of micro-cracks. At the material's failure, a localized band of plastic deformation is formed [97]. According to the findings by Anand and Spitzig [2], this failure under shear stress is induced by local plastic bands, where the formation or growth of pores does not necessarily have to occur within them.

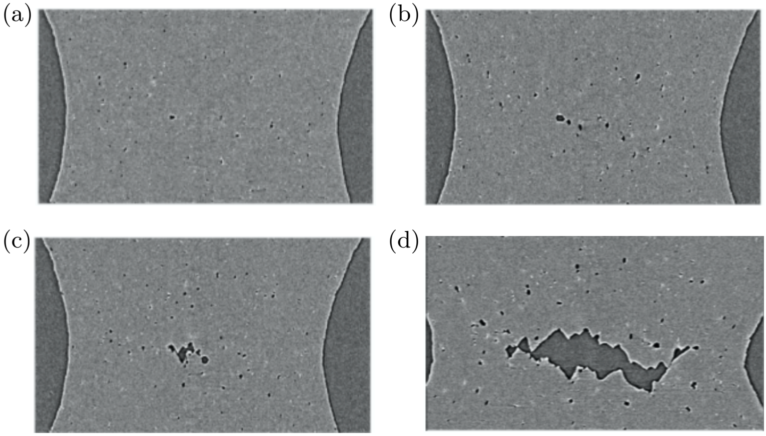

Figure 1.1: X-ray tomography of an aluminum alloy showing damage process leading to the cracking [92].

1.1.2 Numerical ductile damage models

In the context of modeling ductile damage and failure in metals, two fundamental approaches are commonly utilized. The first approach involves micro-mechanical studies focusing on voids and micro-defects. In this method, one or more internal variables, which represent the volume fraction of voids, serve as a representation of damage in the material. McClintock [82] and Rice and Tracey [95] examined and simulated the progression of microvoids within an elastoplastic matrix. They noted that the expansion of voids is mainly influenced by the stress triaxiality. However, the phenomenon of void interaction and coalescence was not studied in detail in prior studies. Therefore, Needleman [87] analyzed the tensile deformation of a square with periodic cylindrical voids, considering an elastic-plastic medium and plane strain conditions.

Furthermore, Gurson [55] carried out numerical studies on a representative volume element containing a spherical void and proposed a constitutive model for a ductile porous medium. The model introduced a single parameter, the void volume fraction, on a yield criterion interpreted as a damage variable. This model can predict only the growth of voids, while the coalescence of voids was not taken into account. Therefore, additional terms were introduced by Tvergaard [110, 111], enhancing the flexibility and accuracy of Gurson's model resulting in popular model known as the Gurson-Tvergaard-Needleman (GTN) model. Since then, numerous modifications have been made in various aspects, including the effects of the shape of the void [53, 54] and its size [117]. Similarly, void shearing mechanism was incorporated in [120], material failure under shear loading was accounted in [84, 86].

The alternative approach is based on the continuum damage mechanics (CDM) framework, where damage processes are phenomenologically described. Damage variables, whether scalars, vectors, or tensors, are introduced into the macroscopic constitutive material laws, accounting for local phenomena such as microvoids and micro-cracks. Kachanov [66] introduced an internal scalar variable to measure the ongoing deterioration (damage) of the material and the concept of effective stress. Rabotnov [94] then provided a physical interpretation for the damage variable as the decrease in the effective cross-section area due to the evolution of micro-cracks. Building upon the concepts of the aforementioned authors, Lemaitre [76] introduced a continuum damage model in which the effective stress and strain equivalence concept allowed for damage measurements, representing the reduction in elastic properties [78]. Moreover, numerous researchers [3, 18, 106, 109] extended and modified the original Lemaitre model to incorporate various phenomena. Nevertheless, the models mentioned rely on a scalar-valued damage representation, which, as noted by Chow and Wang [42, 43], may lead to questionable conclusions in the failure analysis of ductile metals, particularly when considering damage-induced material anisotropy. In this context, several authors [48, 71, 104] used vectors as damage variables. Furthermore, the approach of describing material anisotropy induced by damage using a second-order damage tensor was explored, as seen in [16, 44, 67]. Similarly, Boehler [17] used fourth-order tensor to describe the damage in elastic materials.

Moreover, the damage behavior of ductile sheet metals is influenced by plastic anisotropy. In metal forming processes, the anisotropic plastic behavior significantly influences the localization of plastic strains, leading to the initiation of anisotropic damage. Benzerga and Besson [15] included plastic anisotropy in their constitutive model for porous materials. The Hill yield criterion [57], which accounts for the anisotropic plastic behavior, was incorporated in Rousselier [98] and Gurson type damage model for ductile metals. It was observed that plastic anisotropy might affect void growth and have detrimental effects in aluminum sheets. Additionally, a new yield function, an extension of the isotropic Gurson model, was proposed in studies such as [68, 69, 83], to investigate the impact of void shape and size effects on anisotropic ductile metals. Furthermore, Badreddine and Saanouni [7] and Badreddine et al. [8] introduced an anisotropic ductile damage model that considers significant anisotropic plastic deformation. The damage was described using a second-order symmetric tensor, while the anisotropic plasticity was characterized by the quadratic Hill yield criterion. Numerical studies have shown that even small changes in the yield condition caused by anisotropies have an effect on ductile damage. It should be noted that the identification of the material parameters and the validation of the model presented in [7, 8] was only based on one-dimensional tensile and deep drawing tests, so that the general validity of the constitutive equations for a wide range of stress conditions is not assured.

1.2 Objectives

While there has been extensive research on the damage and fracture behavior of isotropic ductile metals, there is a limited body of studies specifically addressing the damage behavior of anisotropic ductile metals. Furthermore, the specimens and experimental methods used to investigate the influence of plastic anisotropy on damage behavior across a wide range of stress-states are not well-developed. A key objective of this work is to develop novel experimental series that facilitate the analysis of the deformation and damage behavior, as well as the anisotropic damage development of anisotropic metallic specimens under varying stress triaxialities. To achieve this goal, a comprehensive experimental methodology is developed and presented, allowing for a systematic study of the loading-direction-dependent damage and failure mechanisms.

Moreover, the phenomenological model developed by Brünig [22, 24, 25] has so far been successfully used in numerical simulations of various experiments with isotropic ductile metals. The effectiveness of the continuum damage model for various loading conditions and stress-states has been well demonstrated, e.g., [33, 35, 36, 39, 40]. However, the extension of this damage model for anisotropic ductile metals, commonly encountered in real-life applications, has not been explored yet. Therefore, another main task of this thesis is to modify the damage model taking plastic anistoropy into account. The anisotropic plastic behavior is modeled using the Hoffman yield criterion [58] taking the strength-differential effect into account. The evolution of isochoric plastic strains is determined by Hill's plastic potential function, resulting in a non-associated flow rule. Utilizing the Hoffman criterion, generalized anisotropic stress invariants, as well as the generalized stress triaxiality and the generalized Lode parameter, have been introduced. The damage condition for anisotropic ductile metals is expressed in terms of the generalized stress invariants.

Additionally, micro-mechanical numerical analyses of a representative volume element (RVE) containing micro-defects are conducted. This numerical study aids in comprehending the impact of anisotropic behavior on various damage and failure processes at the micro-scale, as well as their influence on macroscopic damage laws. Material parameters are identified from the numerical results of the RVE and incorporated into the damage model to account for stress-state and loading-direction dependence.

Ultimately, the enhanced continuum damage model, considering plastic anisotropy, is implemented in Ansys through a user-defined subroutine. A comparative analysis is conducted between the numerical results and experimental data.

1.3 Outline of the thesis

The thesis is organized as follows: Chapter 2 provides a concise overview of the constitutive framework of the phenomenological continuum damage model, including the necessary modifications to capture the damage behavior of anisotropic ductile metals. Chapter 3 focuses on the finite element method and the numerical implementation of the derived constitutive equations. The experimental procedure is presented in Chapter 4 and the method to identify the material parameters from the experiments is discussed in Chapter 5. Chapter 6 describes the numerical aspects to further identify the material parameters. The experimental and numerical results including the biaxial specimens are presented in Chapter 7 and in the concluding Chapter 8, the work is summarized and future research topics are suggested.

2 Continuum damage model

Brünig [24] developed a novel continuum damage model to describe deformations and damage behavior of ductile metals. However, this phenomenological model only considers isotropic plasticity. In this work, the continuum model is enhanced to describe the effect of anisotropic plastic behavior on damage and failure mechanisms. The fundamentals and the required mechanical quantities to adequately define the macroscopic phenomenological damage model are discussed in the following section.

2.1 Kinematics

Fig. 2.1 shows the basic idea behind the continuum damage model. The kinematics of the damage mechanics is based on the different configurations, which follows the previous ideas of Murakami [85]. The key points are summarized as follows:

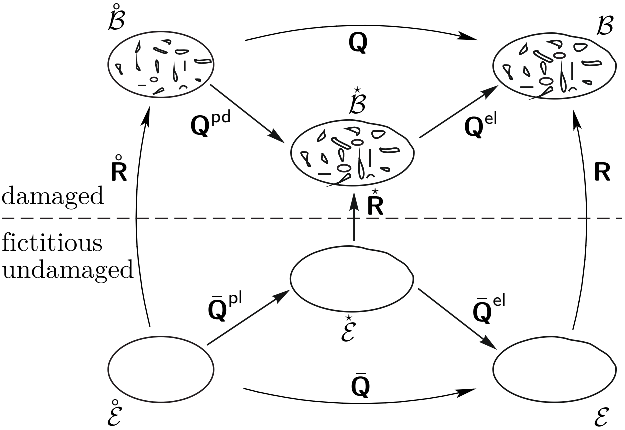

Figure 2.1: Configurations and metric transformation tensors.

- Introduction of the initial undeformed configuration $\mathring{\mathcal{B}}$, which might have initial damage in the material and the current damaged configuration $\mathcal{B}$. Additionally, a fictitious stress free state is considered in the damaged configurations $\overset{\star}{\mathcal{B}}$.
- Usage of the base vectors and the associated metric coefficients containing the scalar products.
- Introduction of the fictitious undamaged configurations $\mathring{\mathcal{E}}$, $\overset{\star}{\mathcal{E}}$ and $\mathcal{E}$ by removing the damage in the three previously introduced damaged configurations.
- Metric transformation tensors in a mixed variant representation are employed to describe and relate the kinematics of undamaged and damaged configurations, respectively.

2.1.1 Damaged configurations

As shown in the Fig. 2.1, the continuum body in the initial configuration $\mathring{\mathcal{B}}$ may contain micro-defects due to the manufacturing process. The quantities related to this configuration are based on the stretched base vectors $\mathring{\boldsymbol{g}}_i$ and the metric coefficients are given as $\mathring{G}_{ij} = \mathring{\boldsymbol{g}}_i \cdot \mathring{\boldsymbol{g}}_j$. Moreover, the base vectors corresponding to elastic-plastic-damaged and fictitious stress free configuration are $\boldsymbol{g}_i$ and $\overset{\star}{\boldsymbol{g}}_i$, respectively. Similarly, $G_{ij} = \boldsymbol{g}_i \cdot \boldsymbol{g}_j$ and $\overset{\star}{G}_{ij} = \overset{\star}{\boldsymbol{g}}_i \cdot \overset{\star}{\boldsymbol{g}}_j$ are the associated metric coefficients to the base vectors $\boldsymbol{g}_i$ and $\overset{\star}{\boldsymbol{g}}_i$, respectively. The total deformations between the initial and current configuration are given by the metric transformation tensor

$$
\begin{aligned}
\mathbf{Q} &= Q^{i}_{.j} \boldsymbol{g}_i \otimes \boldsymbol{g}^j \\
&= \mathring{G}^{ik} G_{kj} \boldsymbol{g}_i \otimes \boldsymbol{g}^j \\
&= \mathring{G}^{ij} \boldsymbol{g}_i \otimes \boldsymbol{g}_j = \mathbf{F}\mathbf{F}^{\mathsf{T}} = \mathbf{B},
\end{aligned}
\tag{2.1}
$$

where $\mathbf{F} = \boldsymbol{g}_i \otimes \mathring{\boldsymbol{g}}^i$ is the deformation gradient and related to both the reference and current configuration. As can be seen in Eq. (2.1), $\mathbf{Q}$ is equal to the left Cauchy-Green or Finger deformation tensor $\mathbf{B}$ in the mixed variant representation.

The metric transformation tensor $\mathbf{Q}$ is multiplicatively decomposed into its inelastic (plastic and damage) and elastic parts

$$\mathbf{Q} = \mathbf{Q}^{\mathsf{pd}}\mathbf{Q}^{\mathsf{el}} \tag{2.2}$$

with the elastic metric transformation tensor

$$\mathbf{Q}^{\mathsf{el}} = \left(Q^{\mathsf{el}}\right)^{i}_{.j}\, \boldsymbol{g}_i \otimes \boldsymbol{g}^j = \overset{\star}{G}{}^{ik} G_{kj} \boldsymbol{g}_i \otimes \boldsymbol{g}^j \tag{2.3}$$

and the inelastic metric transformation tensor

$$\mathbf{Q}^{\mathsf{pd}} = \left(Q^{\mathsf{pd}}\right)^{i}_{.j}\, \boldsymbol{g}_i \otimes \boldsymbol{g}^j = \overset{\circ}{G}{}^{ik} \overset{\star}{G}_{kj} \boldsymbol{g}_i \otimes \boldsymbol{g}^j . \tag{2.4}$$

It is evident that $\mathbf{Q}^{\mathsf{el}}$ is symmetric while $\mathbf{Q}^{\mathsf{pd}}$ is a non-symmetric tensor. With the help of $\mathbf{Q}$, the logarithmic Hencky strain tensor is defined as

$$\mathbf{A} = \frac{1}{2} \ln \mathbf{Q} = \frac{1}{2} (\ln Q)^{i}_{.j} \boldsymbol{g}_i \otimes \boldsymbol{g}^j = A^{i}_{.j} \boldsymbol{g}_i \otimes \boldsymbol{g}^j \tag{2.5}$$

and to describe the reversible deformations, the elastic part of the Hencky strain tensor

$$\mathbf{A}^{\mathsf{el}} = \frac{1}{2} \ln \mathbf{Q}^{\mathsf{el}} \tag{2.6}$$

is introduced. Furthermore, following Lehmann [75], the symmetric strain rate is described by

$$\dot{\mathbf{H}} = \frac{1}{2} \mathbf{Q}^{-1} \dot{\mathbf{Q}} = \dot{H}^{i}_{.j} \boldsymbol{g}_i \otimes \boldsymbol{g}^j . \tag{2.7}$$

Moreover, utilizing the non-symmetric metric transformation tensor $\mathbf{Q}$ and its Oldroyd rate

$$\dot{\mathbf{Q}} = \overset{\circ}{G}{}^{ik} \dot{G}_{kj} \boldsymbol{g}_i \otimes \boldsymbol{g}^j \tag{2.8}$$

the symmetric strain rate $\dot{\mathbf{H}}$ can be additively decomposed as follows

$$\begin{aligned}\dot{\mathbf{H}} &= \frac{1}{2}\mathbf{Q}^{-1}\dot{\mathbf{Q}} \\ &= \frac{1}{2}\mathbf{Q}^{\mathsf{el}-1}\mathbf{Q}^{\mathsf{pd}-1}(\dot{\mathbf{Q}}^{\mathsf{pd}}\mathbf{Q}^{\mathsf{el}} + \mathbf{Q}^{\mathsf{pd}}\dot{\mathbf{Q}}^{\mathsf{el}}) \\ &= \frac{1}{2}\mathbf{Q}^{\mathsf{el}-1}\mathbf{Q}^{\mathsf{pd}-1}\dot{\mathbf{Q}}^{\mathsf{pd}}\mathbf{Q}^{\mathsf{el}} + \frac{1}{2}\mathbf{Q}^{\mathsf{el}-1}\dot{\mathbf{Q}}^{\mathsf{el}} \\ &= \dot{\mathbf{H}}^{\mathsf{pd}} + \dot{\mathbf{H}}^{\mathsf{el}}\end{aligned} \tag{2.9}$$

where $\dot{\mathbf{H}}^{\mathsf{pd}}$ and $\dot{\mathbf{H}}^{\mathsf{el}}$ are the inelastic and elastic strain rate, respectively.

2.1.2 Fictitious undamaged configurations

The damage that occurred in the body is hypothetically removed, and the fictitious undamaged configurations are introduced. In particular, removing the pre-existing initial damage that might be present in the initial configuration $\overset{\circ}{\mathcal{B}}$, we get the initial fictitious undamaged configuration $\overset{\circ}{\mathcal{E}}$ with base vectors $\overset{\circ}{\boldsymbol{e}}_i$. Similarly, $\mathcal{E}$ is the current fictitious undamaged configuration with base vectors $\boldsymbol{e}_i$ and $\overset{\star}{\mathcal{E}}$ is the stress free intermediate configuration with base vectors $\overset{\star}{\boldsymbol{e}}_i$. Only elastic-plastic deformations take place in these configurations. Analog to the metric coefficients in damaged configurations, the corresponding metric coefficients for the undamaged fictitious configurations are

$$\begin{aligned}\overset{\circ}{E}_{ij} &= \overset{\circ}{\boldsymbol{e}}_i \cdot \overset{\circ}{\boldsymbol{e}}_j \ , \\ E_{ij} &= \boldsymbol{e}_i \cdot \boldsymbol{e}_j \ , \\ \overset{\star}{E}_{ij} &= \overset{\star}{\boldsymbol{e}}_i \cdot \overset{\star}{\boldsymbol{e}}_j \ .\end{aligned} \tag{2.10}$$

Furthermore, using these metric coefficients, the undamaged metric transformation tensor is given as

$$\bar{\mathbf{Q}} = \bar{Q}^{i}_{.j}\boldsymbol{e}_i \otimes \boldsymbol{e}^j = \overset{\circ}{E}{}^{ik}E_{kj}\boldsymbol{e}_i \otimes \boldsymbol{e}^j. \tag{2.11}$$

With the help of the damage deformation gradient

$$\tilde{\mathbf{F}} = \boldsymbol{g}_i \otimes \boldsymbol{e}^i \tag{2.12}$$

the undamaged metric transformation tensor can be pushed forward to the current damaged configuration $\mathcal{B}$ as done in Brünig [24]. Hence, the effective metric transformation tensor with respect to the current configuration base vectors is given as

$$\bar{\mathbf{Q}} = \bar{Q}^{i}_{.j}\boldsymbol{g}_i \otimes \boldsymbol{g}^j \tag{2.13}$$

which is multiplicatively decomposed, as shown in Fig. 2.1

$$\bar{\mathbf{Q}} = \bar{\mathbf{Q}}^{\mathsf{pl}}\bar{\mathbf{Q}}^{\mathsf{el}} \tag{2.14}$$

into its undamaged elastic part

$$\bar{\mathbf{Q}}^{\mathsf{el}} = \overset{\star}{E}{}^{ik}E_{kj}\boldsymbol{g}_i \otimes \boldsymbol{g}^j \tag{2.15}$$

and into its undamaged plastic part

$$\bar{\mathbf{Q}}^{\mathsf{pl}} = \overset{\circ}{E}{}^{ik}\overset{\star}{E}_{kj}\boldsymbol{g}_i \otimes \boldsymbol{g}^j. \tag{2.16}$$

Again, similar to the definition of strain tensors in the damaged configurations, the effective Hencky strain tensor is introduced as

$$\bar{\mathbf{A}} = \frac{1}{2}\ln\bar{\mathbf{Q}} = \frac{1}{2}(\ln\bar{Q})^{i}_{.j}\boldsymbol{g}_i \otimes \boldsymbol{g}^j = \bar{A}^{i}_{.j}\boldsymbol{g}_i \otimes \boldsymbol{g}^j \tag{2.17}$$

and the elastic part of the effective Hencky strain tensor is given by

$$\bar{\mathbf{A}}^{\mathsf{el}} = \frac{1}{2}\ln\bar{\mathbf{Q}}^{\mathsf{el}}. \tag{2.18}$$

Similarly, the effective strain rate is additively decomposed into

$$\begin{aligned}
\dot{\mathbf{H}} &= \frac{1}{2}\bar{\mathbf{Q}}^{-1}\dot{\bar{\mathbf{Q}}} \\
&= \frac{1}{2}\bar{\mathbf{Q}}^{\mathsf{el}-1}\bar{\mathbf{Q}}^{\mathsf{pl}-1}\dot{\bar{\mathbf{Q}}}^{\mathsf{pl}}\bar{\mathbf{Q}}^{\mathsf{el}} + \frac{1}{2}\bar{\mathbf{Q}}^{\mathsf{el}-1}\dot{\bar{\mathbf{Q}}}^{\mathsf{el}} \\
&= \dot{\mathbf{H}}^{\mathsf{pl}} + \dot{\mathbf{H}}^{\mathsf{el}}
\end{aligned} \tag{2.19}$$

where $\dot{\mathbf{H}}^{\mathsf{pl}}$ is the plastic strain rate tensor and $\dot{\mathbf{H}}^{\mathsf{el}}$ is the elastic one.

2.1.3 Damage metric transformation tensor

To describe the damage between the damaged and undamaged configurations in a kinematic way, the damage metric transformation tensors are introduced as

$$\begin{aligned}
\mathring{\mathbf{R}} &= \mathring{R}^{i}_{.j}\,\boldsymbol{g}_i \otimes \boldsymbol{g}^j = \mathring{E}^{ik}\mathring{G}_{kj}\,\boldsymbol{g}_i \otimes \boldsymbol{g}^j \\
\overset{\star}{\mathbf{R}} &= \overset{\star}{R}{}^{i}_{.j}\,\boldsymbol{g}_i \otimes \boldsymbol{g}^j = \overset{\star}{E}{}^{ik}\overset{\star}{G}_{kj}\,\boldsymbol{g}_i \otimes \boldsymbol{g}^j \\
\mathbf{R} &= R^{i}_{.j}\,\boldsymbol{g}_i \otimes \boldsymbol{g}^j = E^{ik}G_{kj}\,\boldsymbol{g}_i \otimes \boldsymbol{g}^j
\end{aligned} \tag{2.20}$$

where $\mathring{\mathbf{R}}$ characterizes the initial damage present in the initial configuration $\mathring{\mathcal{B}}$. Similarly, the metric transformation tensors $\overset{\star}{\mathbf{R}}$ and $\mathbf{R}$ represent the internal state variable describing the current damage state of the material. Following Murakami [85] and Brünig [24], unless the elastic deformations are small, the damage should be characterized by $\overset{\star}{\mathbf{R}}$, as $\mathbf{R}$ depends on the current state of deformation and cannot properly describe the damage. The damage metric transformation tensor $\overset{\star}{\mathbf{R}}$ describes the actual damage state in the current configuration, irrespective of the current elastic deformation and relates the elastically unloaded configuration $\overset{\star}{\mathcal{B}}$ and the corresponding elastically unloaded configuration $\overset{\star}{\mathcal{E}}$ in the damaged and undamaged configurations, respectively. Hence, using $\overset{\star}{\mathbf{R}}$, the corresponding Hencky damage strain tensor is given as

$$\mathbf{A}^{\mathsf{da}} = \frac{1}{2}\ln \overset{\star}{\mathbf{R}} \tag{2.21}$$

and the damage strain rate can be defined as

$$\dot{\mathbf{H}}^{\mathsf{da}} = \frac{1}{2}\overset{\star}{\mathbf{R}}{}^{-1}\dot{\overset{\star}{\mathbf{R}}}. \tag{2.22}$$

2.1.4 Total deformation

Using the kinematics as shown in Fig. 2.1, the total deformation between the initial configuration $\mathring{\mathcal{B}}$ and the final configuration $\mathcal{B}$ is characterized with the help of the metric transformation tensor $\mathbf{Q}$. Furthermore, $\mathbf{Q}$

can be multiplicatively decomposed as

$$\mathsf{Q} = \mathring{\mathsf{R}}^{-1}\bar{\mathsf{Q}}^{\mathsf{pl}}\overset{\star}{\mathsf{R}}\mathsf{Q}^{\mathsf{el}} \tag{2.23}$$

which includes the multiplicative decomposition of the damage and the metric transformation tensors. Thus, the deformations due to pre-existing damage, plastic deformation, complete damage and the elastic deformations are defined. Using the equations Eq. (2.23) and Eq. (2.7) and with some manipulations

$$\begin{aligned}\dot{\mathsf{H}} &= \frac{1}{2}\mathsf{Q}^{-1}\dot{\mathsf{Q}} \\ &= \dot{\mathsf{H}}^{\mathsf{el}} + \mathsf{R}^{-1}\dot{\bar{\mathsf{H}}}^{\mathsf{pl}}\mathsf{R} + \mathsf{Q}^{\mathsf{el}-1}\dot{\mathsf{H}}^{\mathsf{da}}\mathsf{Q}^{\mathsf{el}}\end{aligned} \tag{2.24}$$

where the strain rate tensor is additively decomposed into an elastic, an effective plastic and a damage part. According to Murakami [85] and Brünig [24], the mechanical state of the material in the current damaged configuration $\mathcal{B}$ is equivalent to that one in the corresponding fictitious undamaged configurations $\mathcal{E}$. This means that the elastic and the effective elastic metric transformation tensor coincide

$$\mathsf{Q}^{\mathsf{el}} = \bar{\mathsf{Q}}^{\mathsf{el}} \tag{2.25}$$

which leads to the equivalence of the elastic strain tensors $\mathsf{A}^{\mathsf{el}} = \bar{\mathsf{A}}^{\mathsf{el}}$ as well as the equivalence of the elastic strain rates $\dot{\mathsf{H}}^{\mathsf{el}} = \dot{\bar{\mathsf{H}}}^{\mathsf{el}}$.

2.2 Thermodynamics

The constitutive equations characterizing the material behavior are restricted by thermodynamics theory. Hence, the continuum damage model should be thermodynamically consistent. Using the basic equations of thermodynamics, we can relate the energies with the stresses and deformations. Thus, by considering the undamaged configurations, the constitutive equations for the elastic-plastic material behavior are formulated. Moreover, the constitutive equations for the elastic-plastic-damaged material behavior are established using the damaged configurations. In this thesis, only the isothermal processes are taken into account so that the temperature is not considered as the state variable.

2.2.1 Fictitious undamaged configurations

In this section, the thermodynamics of elastic-plastic behavior related to the effective undamaged configuration is discussed. The effective Kirchhoff stress tensor with respect to the base vectors of the current damaged configuration is introduced as

$$\bar{\mathbf{T}} = \bar{T}^{i}_{.j} \boldsymbol{g}_i \otimes \boldsymbol{g}^j . \tag{2.26}$$

The scalar product of $\bar{\mathbf{T}}$ with its work conjugate pair $\dot{\mathbf{H}}$ gives us the rate of the effective specific mechanical work $\dot{\bar{w}}$ as

$$\rho_0 \dot{\bar{w}} = \bar{\mathbf{T}} \cdot \dot{\mathbf{H}} \tag{2.27}$$

where ρ_0 is the density of the material in the initial configuration. The work rate $\dot{\bar{w}}$ can be additively decomposed into elastic and plastic parts using Eq. (2.19)

$$\rho_0 \dot{\bar{w}} = \rho_0 \dot{\bar{w}}^{\mathsf{el}} + \rho_0 \dot{\bar{w}}^{\mathsf{pl}} \quad = \bar{\mathbf{T}} \cdot \dot{\mathbf{H}}^{\mathsf{el}} + \bar{\mathbf{T}} \cdot \dot{\mathbf{H}}^{\mathsf{pl}} . \tag{2.28}$$

Moreover, the specific Helmholtz free energy $\bar{\phi}$ for the undamaged configuration is the summation of effective elastic and plastic part. As the hardening of the material has no effect on the elastic behavior, see Brünig [22], the specific free energy is given as

$$\bar{\phi} = \bar{\phi}^{\mathsf{el}}(\bar{\mathbf{A}}^{\mathsf{el}}) + \bar{\phi}^{\mathsf{pl}}(\gamma) \tag{2.29}$$

where γ is a internal scalar variable characterizing plastic material behavior. Then, the rate of the specific free energy $\dot{\bar{\phi}}$ is obtained as

$$\dot{\bar{\phi}} = \frac{\partial \bar{\phi}^{\mathsf{el}}}{\partial \bar{\mathbf{A}}^{\mathsf{el}}} \cdot \dot{\bar{\mathbf{A}}}^{\mathsf{el}} + \dot{\bar{\phi}}^{\mathsf{pl}} . \tag{2.30}$$

Hence, the second law of thermodynamics or the Clausius-Duham inequality can be written as

$$\bar{\mathbf{T}} \cdot \dot{\bar{\mathbf{H}}}^{\mathsf{el}} + \bar{\mathbf{T}} \cdot \dot{\bar{\mathbf{H}}}^{\mathsf{pl}} - \rho_0 \frac{\partial \bar{\phi}^{\mathsf{el}}}{\partial \bar{\mathbf{A}}^{\mathsf{el}}} \cdot \dot{\bar{\mathbf{A}}}^{\mathsf{el}} - \rho_0 \dot{\bar{\phi}}^{\mathsf{pl}} \geq 0. \tag{2.31}$$

According to Lehmann [74] and Brünig [22], considering the isotropic elastic material behavior, one reaches at the hyperelastic constitutive law

$$\bar{\mathbf{T}} = \rho_0 \frac{\partial \bar{\phi}^{\mathsf{el}}}{\partial \bar{\mathbf{A}}^{\mathsf{el}}}. \tag{2.32}$$

The irreversible parts remaining in Eq. (2.31), $\bar{\mathbf{T}} \cdot \dot{\bar{\mathbf{H}}}^{\mathsf{pl}} - \rho_0 \dot{\bar{\phi}}^{\mathsf{pl}} \geq 0$, form the Kelvin inequality characterizing the internal dissipation.

2.2.2 Damaged configurations

In addition to the elastic and plastic parts, for the damaged configuration, damage deformation processes are also taken into account as in Eq. (2.24). Similarly, the rate of the specific mechanical work $\dot{w}$ consists of elastic, plastic and damage parts. Moreover, the scalar product of the Kirchhoff stress tensor for the damaged configuration $\mathbf{T} = T^{i}_{\cdot j} \boldsymbol{g}_i \otimes \boldsymbol{g}^j$ and its work conjugate part $\dot{\mathbf{H}}$ gives the specific mechanical work

$$\rho_0 \dot{w} = \mathbf{T} \cdot \dot{\mathbf{H}}. \tag{2.33}$$

Using Eq. (2.24) we obtain

$$\rho_0 \dot{w} = \mathbf{T} \cdot \dot{\mathbf{H}}^{\mathsf{el}} + \mathbf{R}\mathbf{T}\mathbf{R}^{-1} \cdot \dot{\bar{\mathbf{H}}}^{\mathsf{pl}} + \tilde{\mathbf{T}} \cdot \dot{\mathbf{H}}^{\mathsf{da}} \tag{2.34}$$

where $\tilde{\mathbf{T}} = \mathbf{Q}^{\mathsf{el}} \mathbf{T} \mathbf{Q}^{\mathsf{el}-1}$ represents the work conjugate stress tensor of the damage strain rate $\dot{\mathbf{H}}^{\mathsf{da}}$ introduced in Eq. (2.22). Furthermore, the specific free energy function for the damaged configurations can be decomposed into the elastic, plastic and damage parts as

$$\phi = \phi^{\mathsf{el}}(\mathbf{A}^{\mathsf{el}}, \mathbf{A}^{\mathsf{da}}) + \phi^{\mathsf{pl}}(\gamma) + \phi^{\mathsf{da}}(\mu). \tag{2.35}$$

As demonstrated by Lemaitre [76] and Cordebois and Sidoroff [44], damage affects the elastic properties of the material. Consequently, the elastic part of specific free energy function ϕ^{el} is dependent on both elastic and damage variables. The internal plastic state variable γ corresponds to the formation of dislocations in crystal lattices along certain slip planes and the internal damage variable μ describes the formation, growth and coalescence of microdefects. It is also assumed that the damage and plastic phenomena are independent of each other, see Lemaitre [77]. Hence, using Eq. (2.34) and Eq. (2.35), the Clausisus-Duham inequality can be written as

$$\begin{aligned}\rho_0\dot{w} - \rho_0\dot{\phi} &= \mathbf{T}\cdot\dot{\mathbf{H}}^{\mathsf{el}} + \mathbf{R}\mathbf{T}\mathbf{R}^{-1}\cdot\dot{\bar{\mathbf{H}}}^{\mathsf{pl}} + \tilde{\mathbf{T}}\cdot\dot{\mathbf{H}}^{\mathsf{da}} \\ &\quad - \rho_0\frac{\partial\phi^{\mathsf{el}}}{\partial\mathbf{A}^{\mathsf{el}}}\cdot\dot{\mathbf{A}}^{\mathsf{el}} - \rho_0\frac{\partial\phi^{\mathsf{el}}}{\partial\mathbf{A}^{\mathsf{da}}}\cdot\dot{\mathbf{A}}^{\mathsf{da}} - \rho_0\dot{\phi}^{\mathsf{pl}} - \rho_0\dot{\phi}^{\mathsf{da}} \geq 0.\end{aligned} \tag{2.36}$$

This, for the reversible part leads to

$$\mathbf{T}\cdot\dot{\mathbf{H}}^{\mathsf{el}} - \rho_0\frac{\partial\phi^{\mathsf{el}}}{\partial\mathbf{A}^{\mathsf{el}}}\cdot\dot{\mathbf{A}}^{\mathsf{el}} = 0 \tag{2.37}$$

which as in Eq. (2.32), results in thermic state equation given as

$$\mathbf{T} = \rho_0\frac{\partial\phi^{\mathsf{el}}}{\partial\mathbf{A}^{\mathsf{el}}}. \tag{2.38}$$

Assuming that the plastic and damage behavior can be separated into two parts, we arrive at the restriction for damage behavior

$$\tilde{\mathbf{T}}\cdot\dot{\mathbf{H}}^{\mathsf{da}} - \rho_0\frac{\partial\phi^{\mathsf{el}}}{\partial\mathbf{A}^{\mathsf{da}}}\cdot\dot{\mathbf{A}}^{\mathsf{da}} - \rho_0\dot{\phi}^{\mathsf{da}} \geq 0. \tag{2.39}$$

The remaining plastic dissipation part in Eq. (2.36) has been considered in the undamaged configurations and is already given in Eq. (2.31).

2.3 Constitutive equations

Within the framework of the thermodynamic considerations discussed above, constitutive laws for the undamaged and fictitious damaged configurations are formulated.

2.3.1 Undamaged configurations

The elastic and plastic material laws for the undamaged material are formulated considering the undamaged configurations. This effective elastic material law is completely unaffected by the damage mechanisms. The isotropic material behavior is given by the Helmholtz free energy function as

$$\rho_0 \bar{\phi}^{\mathsf{el}}\left(\bar{\mathbf{A}}^{\mathsf{el}}\right) = G\bar{\mathbf{A}}^{\mathsf{el}} \cdot \bar{\mathbf{A}}^{\mathsf{el}} + \frac{1}{2}\left(K - \frac{2}{3}G\right)\left(\operatorname{tr}\bar{\mathbf{A}}^{\mathsf{el}}\right)^2 \tag{2.40}$$

where G is the shear modulus and K the bulk modulus of the matrix material. Making use of the hyperelastic relation in Eq. (2.32), the effective stress tensor is given as

$$\bar{\mathbf{T}} = \rho_0 \frac{\partial \bar{\phi}^{\mathsf{el}}}{\partial \bar{\mathbf{A}}^{\mathsf{el}}} = 2G\bar{\mathbf{A}}^{\mathsf{el}} + \left(K - \frac{2}{3}G\right)\operatorname{tr}\bar{\mathbf{A}}^{\mathsf{el}}\mathbf{1}. \tag{2.41}$$

Further, differentiating to the corresponding strain the elastic tangent modulus is given as

$$\bar{\mathbb{C}}^{\mathsf{el}} = \frac{\mathrm{d}\bar{\mathbf{T}}}{\mathrm{d}\bar{\mathbf{A}}^{\mathsf{el}}} = 2G\mathbb{1} + \left(K - \frac{2}{3}G\right)\mathbf{1}\otimes\mathbf{1} \tag{2.42}$$

where $\mathbb{1}$ is the fourth order identity tensor.
Due to the manufacturing processes like rolling, the sheet metals undergo severe plastic deformations. These processes introduce preferential orientations to the grains, leading to a direction-dependent behavior known as anisotropy [59], which is difficult to avoid [65]. The other origin of anisotropy is alignment in the microstructure and especially the distribution of second phase particles such as inclusions. Material anisotropy significantly influences the distribution of stresses and strains, impacting the shape of the final parts, their thickness, and potential instabilities, such as wrinkling in deep-drawn parts.

Furthermore, experimental studies done by Spitzig and Richmond [101], Wilson [119], Bai and Wierzbicki [9] and Wei et al. [116], revealed that the yield stresses in aluminum alloys were different for uniaxial tension and compression tests. This difference in yield stresses known as strength-differential (SD) effect should be taken into account for the investigated material. Hence, including anisotropy and SD effect, the beginning of plastic yielding is modeled using the Hoffman yield criterion [58]

$$f^{\mathsf{pl}} = \mathbf{C} \cdot \bar{\mathbf{T}} + \sqrt{\frac{1}{2}\bar{\mathbf{T}} \cdot \boldsymbol{D}\bar{\mathbf{T}}} - c = 0 \tag{2.43}$$

where $\mathbf{C} = C^{i}_{.j}\, \boldsymbol{g}_i \otimes \boldsymbol{g}^j$ is the second order tensor containing the coefficients characterizing the SD effect. The components are

$$[C^{i}_{.j}] = \begin{bmatrix} C_1 & 0 & 0 \\ 0 & C_2 & 0 \\ 0 & 0 & C_3 \end{bmatrix}.$$

Similarly, $\boldsymbol{D} = D^{i.k}_{.j.l}\, \boldsymbol{g}_i \otimes \boldsymbol{g}^j \otimes \boldsymbol{g}_k \otimes \boldsymbol{g}^l$ is the fourth order tensor including anisotropic material parameters of the Hoffman yield criterion and the components can be written in the matrix form as

$$[D^{i.k}_{.j.l}] = \begin{bmatrix} C_4 + C_5 & -C_4 & -C_5 & 0 & 0 & 0 \\ -C_4 & C_4 + C_6 & -C_6 & 0 & 0 & 0 \\ -C_5 & -C_6 & C_5 + C_6 & 0 & 0 & 0 \\ 0 & 0 & 0 & C_7 & 0 & 0 \\ 0 & 0 & 0 & 0 & C_8 & 0 \\ 0 & 0 & 0 & 0 & 0 & C_9 \end{bmatrix}$$

and c is the equivalent yield stress of the undamaged material. It is supposed that the principal axes of anisotropy coincide with the principal axes of stress tensor. These principal axes lie in the x-direction of rolling direction (RD, 0°), in the y-direction transversely in the plane of the sheet (TD, 90°) and in the z-direction normal to this plane as shown in Fig. 2.2. Stress invariants have been extensively used to describe the stress state expressed in terms of principal stresses, namely the stress triaxiality and the Lode parameter, of the isotropic ductile metals in McClintock [82], Rice and Tracey [95] and in Bao and Wierzbicki [10]. Brünig et al. [30] performed micro-simulations and developed stress state dependent functions using stress invariants for isotropic metals. However, for the case of anisotropy, all the stress components should be used to define the stress state of anisotropic materials.

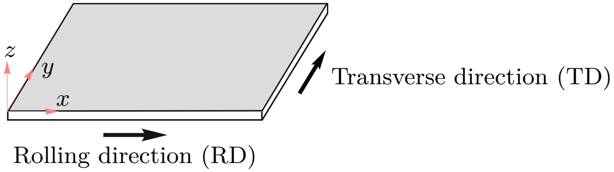

Figure 2.2: Schematic of rolling direction (RD) and transverse direction (TD) in a metal sheet.

Therefore, the stress triaxiality and the Lode parameter have to be defined for anisotropic materials. Park et al. [90] and Rickhey and Hong [96] defined the stress triaxiality taking anisotropic equivalent stress into account but the mean stress was still calculated utilizing the principal stresses. Also, the principal stresses are used to calculate the Lode parameter. In this context, using the Hoffman yield condition (Eq. (2.43)), the first stress invariant is newly defined as

$$\bar{I}_1^{\mathsf{H}} = \frac{1}{a}\mathbf{C}\cdot\bar{\mathbf{T}} \quad \text{with} \quad a = \frac{1}{3}\,\mathrm{tr}\,\mathbf{C}. \tag{2.44}$$

Similarly, the second deviatoric stress invariant taking Hoffman yield condition into account is given as

$$\bar{J}_2^{\mathsf{H}} = \frac{1}{2}\bar{\mathbf{T}}\cdot\boldsymbol{D}\bar{\mathbf{T}} \tag{2.45}$$

and finally the third deviatoric stress invariant is

$$\bar{J}_3^{\mathsf{H}} = \det(\boldsymbol{D}\bar{\mathbf{T}}). \tag{2.46}$$

With these generalized stress invariants based on the Hoffman yield condition, the stress triaxiality

$$\bar{\eta}^{\mathsf{H}} = \frac{\bar{I}_1^{\mathsf{H}}}{3\sqrt{3\bar{J}_2^{\mathsf{H}}}} \tag{2.47}$$

and the Lode Parameter

$$\bar{L}^{\mathsf{H}} = \frac{-3\sqrt{3}\,\bar{J}_3^{\mathsf{H}}}{2\left(\bar{J}_2^{\mathsf{H}}\right)^{(3/2)}} \tag{2.48}$$

are newly introduced to characterize the stress state of the anisotropic materials. Making use of Eqs. (2.44) and (2.45), the yield condition Eq. (2.43) can be rewritten as

$$f^{\mathsf{pl}} = a\bar{I}_1^{\mathsf{H}} + \sqrt{\bar{J}_2^{\mathsf{H}}} - c = 0\ . \tag{2.49}$$

Only a small change in plastic volume was observed during the experiments done by Spitzig et al. [103]. Therefore, ignoring the effect of $\bar{I}_1^{\mathsf{H}}$, a plastic potential function is chosen as

$$g^{\mathsf{pl}} = \sqrt{\bar{J}_2^{\mathsf{H}}} \tag{2.50}$$

which leads to the non-associated flow rule and the effective plastic strain rate tensor is given as

$$\dot{\bar{\mathbf{H}}}^{\mathsf{pl}} = \dot{\lambda}\frac{\partial g^{\mathsf{pl}}}{\partial \bar{\mathbf{T}}} = \dot{\lambda}\frac{1}{2\sqrt{\bar{J}_2^{\mathsf{H}}}}\boldsymbol{D}\bar{\mathbf{T}} = \dot{\gamma}\bar{\mathbf{N}} \tag{2.51}$$

where $\dot{\gamma}$ is a non-negative scalar factor and $\bar{\mathbf{N}}$ is the normalized effective deviatoric stress tensor given by

$$\dot{\gamma} = \dot{\lambda}\frac{\|\boldsymbol{D}\,\bar{\mathbf{T}}\|}{2\sqrt{\bar{J}_2^{\mathsf{H}}}} \quad \text{and} \quad \bar{\mathbf{N}} = \frac{\boldsymbol{D}\,\bar{\mathbf{T}}}{\|\boldsymbol{D}\,\bar{\mathbf{T}}\|}. \tag{2.52}$$

2.3.2 Damaged configurations

Based on the thermodynamic consideration of the damaged configurations, the constitutive equations for the deformation behavior of an anisotropically damaged material are formulated. Under external loading, the presence of microdefects leads to an elevation of stress levels in the remaining effective load-carrying area. Conversely, it causes a reduction in the stored energy in the damaged material compared to the undamaged material. To describe these phenomena within the constitutive framework of a phenomenological elastic–plastic–damage model, the damaged elastic strain energy ϕ^{el}, representing the elastic behavior of the damaged aggregate, is selected as a function of $\mathbf{A}^{\mathsf{el}}$ and $\mathbf{A}^{\mathsf{da}}$. Assuming isotropic linear-elastic material in the initial undamaged state, the function ϕ^{el} is assumed to be a quadratic function of the elastic strain and a linear function of the damage and given as

$$\begin{aligned}\rho_0\phi^{\mathsf{el}}\left(\mathbf{A}^{\mathsf{el}},\mathbf{A}^{\mathsf{da}}\right) &= G\,\mathbf{A}^{\mathsf{el}}\cdot\mathbf{A}^{\mathsf{el}} + \frac{1}{2}\left(K-\frac{2}{3}G\right)\left(\operatorname{tr}\mathbf{A}^{\mathsf{el}}\right)^2 \\ &\quad + \eta_1\operatorname{tr}\mathbf{A}^{\mathsf{da}}\left(\operatorname{tr}\mathbf{A}^{\mathsf{el}}\right)^2 + \eta_2\operatorname{tr}\mathbf{A}^{\mathsf{da}}\mathbf{A}^{\mathsf{el}}\cdot\mathbf{A}^{\mathsf{el}} \\ &\quad + \eta_3\operatorname{tr}\mathbf{A}^{\mathsf{el}}\mathbf{A}^{\mathsf{da}}\cdot\mathbf{A}^{\mathsf{el}} + \eta_4\,\mathbf{A}^{\mathsf{el}}\cdot\left(\mathbf{A}^{\mathsf{el}}\mathbf{A}^{\mathsf{da}}\right).\end{aligned} \tag{2.53}$$

The additional parameters η_1 to η_4 consider worsening effect of damage on the elastic material behavior as seen in experiments. Again, differentiation of Eq. (2.53) to the corresponding strain, like in Eq. (2.32), gives the Kirchhoff stress tensor as

$$\begin{aligned}\mathbf{T} = \rho_0\frac{\partial\phi^{\mathsf{el}}}{\partial\mathbf{A}^{\mathsf{el}}} &= 2\left(G+\eta_2\operatorname{tr}\mathbf{A}^{\mathsf{da}}\right)\mathbf{A}^{\mathsf{el}} \\ &+ \left[\left(K-\frac{2}{3}G+2\eta_1\operatorname{tr}\mathbf{A}^{\mathsf{da}}\right)\operatorname{tr}\mathbf{A}^{\mathsf{el}} + \eta_3\left(\mathbf{A}^{\mathsf{da}}\cdot\mathbf{A}^{\mathsf{el}}\right)\right]\mathbf{1} \\ &+ \eta_3\operatorname{tr}\mathbf{A}^{\mathsf{el}}\mathbf{A}^{\mathsf{da}} + \eta_4\left(\mathbf{A}^{\mathsf{el}}\mathbf{A}^{\mathsf{da}}+\mathbf{A}^{\mathsf{da}}\mathbf{A}^{\mathsf{el}}\right).\end{aligned} \tag{2.54}$$

Furthermore, the total differential of Eq. (2.54) is given by

$$\begin{aligned}\mathrm{d}\mathbf{T} &= \frac{\partial\mathbf{T}}{\partial\mathbf{A}^{\mathsf{el}}}\mathrm{d}\mathbf{A}^{\mathsf{el}} + \frac{\partial\mathbf{T}}{\partial\mathbf{A}^{\mathsf{da}}}\mathrm{d}\mathbf{A}^{\mathsf{da}} \\ &= \mathbb{C}^{\mathsf{el}}\mathrm{d}\mathbf{A}^{\mathsf{el}} + \mathbb{C}^{\mathsf{da}}\mathrm{d}\mathbf{A}^{\mathsf{da}}\end{aligned} \tag{2.55}$$

which leads to the elastic-damage tangent modulus

$$\begin{aligned}\mathbb{C}^{\mathsf{el}} = \frac{\partial \mathbf{T}}{\partial \mathbf{A}^{\mathsf{el}}} &= 2\left(G + \eta_2 \operatorname{tr} \mathbf{A}^{\mathsf{da}}\right) \mathbb{1} \\ &+ \left(K - \frac{2}{3}G + 2\eta_1 \operatorname{tr} \mathbf{A}^{\mathsf{da}}\right) \mathbf{1} \otimes \mathbf{1} \\ &+ \eta_3 \left(\mathbf{A}^{\mathsf{da}} \otimes \mathbf{1} + \mathbf{1} \otimes \mathbf{A}^{\mathsf{da}}\right) + \eta_4 \mathbb{A}^{\mathsf{da}}\end{aligned} \tag{2.56}$$

with the fourth-order damage tensor

$$\mathbb{A}^{\mathsf{da}} = \left[(A^{\mathsf{da}})^{i\cdot}_{\cdot l}\,\delta^{k\cdot}_{\cdot j} + (A^{\mathsf{da}})^{k\cdot}_{\cdot j}\,\delta^{i\cdot}_{\cdot l}\right] \boldsymbol{g}_i \otimes \boldsymbol{g}^j \otimes \boldsymbol{g}_k \otimes \boldsymbol{g}^l \tag{2.57}$$

and the damage tangent modulus

$$\begin{aligned}\mathbb{C}^{\mathsf{da}} = \frac{\partial \mathbf{T}}{\partial \mathbf{A}^{\mathsf{da}}} &= 2\eta_1 \operatorname{tr} \mathbf{A}^{\mathsf{el}} \mathbf{1} \otimes \mathbf{1} + 2\eta_2\, \mathbf{A}^{\mathsf{el}} \otimes \mathbf{1} + \eta_3\, \mathbf{1} \otimes \mathbf{A}^{\mathsf{el}} \\ &+ \eta_3 \operatorname{tr} \mathbf{A}^{\mathsf{el}} \mathbb{1} + \eta_4\, \mathbb{A}^{\mathsf{el}}\end{aligned} \tag{2.58}$$

with the fourth-order elastic tensor given by

$$\mathbb{A}^{\mathsf{el}} = \left[(A^{\mathsf{el}})^{i\cdot}_{\cdot l}\,\delta^{k\cdot}_{\cdot j} + (A^{\mathsf{el}})^{k\cdot}_{\cdot j}\,\delta^{i\cdot}_{\cdot l}\right] \boldsymbol{g}_i \otimes \boldsymbol{g}^j \otimes \boldsymbol{g}_k \otimes \boldsymbol{g}^l. \tag{2.59}$$

In analogy to the yield criterion for plasticity (Eq. (2.43)), to characterize the onset and evolution of damage in metals with plastic anisotropy, the damage condition

$$f^{\mathsf{da}} = \alpha I_1^{\mathsf{H}} + \beta \sqrt{J_2^{\mathsf{H}}} - \sigma = 0 \tag{2.60}$$

is introduced, where I_1^{H} and J_2^{H} are the generalized first and second deviatoric Hoffman invariants of the Kirchhoff stress tensor in Eq. (2.54) taking the hydrostatic and deviatoric stress effects caused by the shape and orientation of micro-defects. σ is the equivalent damage stress which can be seen as the material resistance to the propagation of micro-cracks. The effective Kirchhoff stress tensor $\bar{\mathbf{T}}$ and the Kirchhoff stress tensor $\mathbf{T}$ are identical at the onset of damage meaning that at this point the generalized Hoffman invariants are equal. Similarly, the stress triaxiality (η^{H}) and the Lode parameter (L^{H}) with respect to the damage configurations, coincide at the onset of damage with $\bar{\eta}^{\mathsf{H}}$ and $\bar{L}^{\mathsf{H}}$ with respect to the undamaged configurations (i.e, $\eta^{\mathsf{H}} = \bar{\eta}^{\mathsf{H}}$, $L^{\mathsf{H}} = \bar{L}^{\mathsf{H}}$).

As has been discussed and shown in several literature, Bao and Wierzbicki [10], Bonora et al. [19], and Brünig et al. [26], damage mechanisms are strongly stress-state dependent. High positive stress triaxialities indicate that the damage process is mainly by void growth and coalescence whereas for small positive or negative stress triaxialities, damage is due to the formation of micro-shear-cracks. Between these two regions, for moderate positive stress triaxialities, both damage mechanisms play a role, see Fig. 2.3. Furthermore, Bao and Wierzbicki [11] and Brünig et al. [34] concluded that the damage doesn't occur after certain value of high negative stress triaxialities.

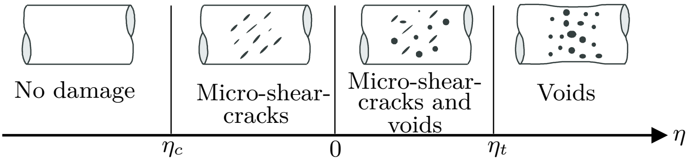

Figure 2.3: Various damage processes categorized based on stress triaxiality η.

In addition, for the isotropic ductile metals, the damage mode parameters α and β are only dependent on the stress-state [30]. For anisotropic ductile metals, Brünig et al. [38] conducted a series of experiments and showed that the damage mode parameters are not only stress-state dependent, but also depend on the loading direction with respect to the rolling direction. Therefore, in this work, α and β are function of stress-state and loading direction. The identification procedure of these parameters will be discussed in the later part.

The damage rule models the growth in macroscopic strains resulting from the nucleation, growth, and coalescence of micro-defects. Given that the strength-differential (SD) effect is already incorporated in the damage condition (Eq. (2.60)), it is not explicitly considered in the damage potential function. This choice not only simplifies the derivation but also facilitates the numerical implementation of the damage law. Therefore, the damage potential function is selected as follows

$$g^{\mathsf{da}}\left(I_1, J_2^{\mathsf{H}}\right) = \tilde{\alpha} I_1 + \tilde{\beta}\sqrt{J_2^{\mathsf{H}}} \tag{2.61}$$

where $I_1 = \operatorname{tr}\mathbf{T}$ is the first stress invariant of the Kirchhoff stress tensor $\mathbf{T}$ and $J_2^{\mathsf{H}} = \frac{1}{2}\mathbf{T}\cdot\boldsymbol{D}\mathbf{T}$ is the second stress invariant based on Hoffman yield criteria related to the damaged configurations. For the anisotropic materials, $\tilde{\alpha}$ and $\tilde{\beta}$ are the stress and loading direction dependent parameters, whose detailed process of identifying is elaborated in Chapter 6. This leads to the non-associated anisotropic damage rule, to describe the macroscopic irreversible strains caused by different damage processes (Fig. 2.3) on the micro-level, as

$$\begin{aligned} \dot{\mathbf{H}}^{\mathsf{da}} &= \dot{\mu}\frac{\partial g^{\mathsf{da}}}{\partial \mathbf{T}} \\ &= \dot{\mu}\left(\frac{\tilde{\alpha}}{\sqrt{3}}\mathbf{1} + \delta\tilde{\beta}\mathbf{N}\right) \end{aligned} \tag{2.62}$$

where $\dot{\mu}$ is the equivalent damage strain rate. δ is a scalar and $\mathbf{N}$ is the normalized deviatoric part of Kirchhoff stress tensor given by

$$\delta = \frac{\|\boldsymbol{D}\,\mathbf{T}\|}{2\sqrt{J_2^{\mathsf{H}}}} \quad \text{and} \quad \mathbf{N} = \frac{\boldsymbol{D}\,\mathbf{T}}{\|\boldsymbol{D}\,\mathbf{T}\|}. \tag{2.63}$$

3 Numerical method

The finite-element method (FEM) is used to solve the discretized equilibrium equations. The numerical simulations are carried out with the commercial finite-element software Ansys classic Mechanical (APDL) version 18.0. The mechanical constitutive laws used in this work, are implemented as a user material routine (UMAT) within the Ansys interface [4]. At the starting of the time increment, the actual strain increment, stresses, strains and other state variables are passed to the UMAT whereas, the updated stresses, state variables and the material Jacobian matrix must be returned to the Ansys at the end of the time step. In the following, only fundamentals of FEM are discussed while the numerical integration of the constitutive model is provided in detail.

3.1 Finite element method

The finite-element method is a popular tool to solve the mathematical model of a physical problem which generally is nonlinear in nature. In engineering, the physical problem often includes a structure or a body under certain loads [14]. To solve the mathematical problem, the body or the domain is divided into different sub-domains or finite elements. Then, the loads are applied incrementally and within these elements satisfying the equilibrium requirements, the solution is approximated using polynomial form. The force equilibrium on a body, for quasi-static condition, is given by balance of momentum as

$$\operatorname{div}\left(\frac{\rho}{\rho_0}\mathbf{T}\right) + \rho\boldsymbol{b} = \mathbf{0} \tag{3.1}$$

where $\boldsymbol{b}$ is the vector of body force density. Multiplying Eq. (3.1) by a test function $\delta\boldsymbol{u}$, which can be interpreted as a virtual displacement and integrating over the volume, one gets the weak form of the equilibrium equation. Furthermore, with the boundary condition and the divergence theorem, the variational formulation of the weak form of the equilibrium equation

$$\delta\mathsf{\Pi} = \int_{\mathring{\mathcal{B}}} \left(\frac{\rho}{\rho_0} \mathbf{\mathsf{T}} \right) \cdot \operatorname{grad}^T \delta\boldsymbol{u} \, \mathrm{d}\mathring{\mathrm{v}} - \rho_0 \int_{\mathring{\mathcal{B}}} \boldsymbol{b} \cdot \delta\boldsymbol{u} \, \mathrm{d}\mathring{\mathrm{v}} - \int_{\partial\mathring{\mathcal{B}}} \bar{\mathbf{\mathsf{t}}} \cdot \delta\boldsymbol{u} \, \mathrm{d}\mathring{\mathrm{a}} = 0 \tag{3.2}$$

is obtained, where B is a initial volume, ∂B its initial surface and $\bar{\mathbf{\mathsf{t}}}$ is the stress vector on the initial surface. Newton-Raphson method is used to solve the nonlinear equations. For this purpose, the nonlinear equations are approximated by the linear ones, incremental quantities are determined and the process is repeated until the original nonlinear equations are satisfied. Using a consistent linearization procedure [64], Eq. (3.2) is expanded using Taylor series and neglecting the higher order terms

$$\delta\mathsf{\Pi}\left(\delta\boldsymbol{u}, \boldsymbol{u} + \varDelta\boldsymbol{u}\right) = \delta\mathsf{\Pi}\left(\delta\boldsymbol{u}, \boldsymbol{u}\right) + \frac{\partial\delta\mathsf{\Pi}}{\partial\boldsymbol{u}} \cdot \varDelta\boldsymbol{u} = 0. \tag{3.3}$$

Moreover, using the shape functions and the material law, the stiffness matrix and the load vector at the element level are obtained. In addition, assembling the element stiffness matrices and the load vectors, we obtain the system of linearized equations as

$$\mathbf{K}\,\varDelta\mathbf{U} = \mathbf{R} \tag{3.4}$$

where $\mathbf{K}$ is the tangent stiffness matrix, $\varDelta\mathbf{U}$ denotes the vector of the displacement increment and $\mathbf{R}$ is a force vector representing the residual or unbalanced force which is given by the difference between the applied and the internal forces. Eq. (3.4) is solved iteratively using Newton-Raphson until $\mathbf{R}$ is less than the prescribed tolerance value.

3.2 Numerical integration of the constitutive rate equations

3.2.1 Scalar rate equations

Fictitious undamaged configurations

The rate of the plastic strain is determined as only elastic-plastic deformation occur in this configuration. Using the plastic consistency condition $\dot{f}^{\mathsf{pl}} = 0$ we arrive at

$$\dot{c} = \frac{\|\boldsymbol{D}\,\bar{\mathbf{T}}\|}{2\sqrt{\boldsymbol{D}\bar{\mathbf{T}}\cdot\bar{\mathbf{T}}}}\bar{\mathbf{N}}\cdot\dot{\bar{\mathbf{T}}} + \mathbf{C}\cdot\dot{\bar{\mathbf{T}}}. \tag{3.5}$$

The rate of the effective stress tensor is given as

$$\dot{\bar{\mathbf{T}}} = \frac{\partial\bar{\mathbf{T}}}{\partial\mathbf{A}^{\mathsf{el}}}\dot{\bar{\mathbf{H}}}^{\mathsf{el}} = 2G\dot{\bar{\mathbf{H}}}^{\mathsf{el}} + \left(K - \frac{2}{3}G\right)\operatorname{tr}\dot{\bar{\mathbf{H}}}^{\mathsf{el}}\mathbf{1}. \tag{3.6}$$

Assuming the plastic incompressibility $\operatorname{tr}\dot{\bar{\mathbf{H}}} = \operatorname{tr}\dot{\bar{\mathbf{H}}}^{\mathsf{el}}$, making use of the scalar product $\bar{\mathbf{N}}\cdot\dot{\bar{\mathbf{T}}} = 2G\bar{\mathbf{N}}\cdot\dot{\bar{\mathbf{H}}}^{\mathsf{el}}$ and Eq. (2.19), the plastic consistency condition can be written further as

$$\begin{aligned}\dot{c} &= \tilde{G}\left(\dot{\varepsilon} - k\dot{\gamma}\right)\\ &= \tilde{G}k\left(\frac{1}{k}\dot{\varepsilon} - \dot{\gamma}\right)\end{aligned} \tag{3.7}$$

with

$$\tilde{G} = \frac{\|\boldsymbol{D}\,\bar{\mathbf{T}}\|}{2\sqrt{\boldsymbol{D}\bar{\mathbf{T}}\cdot\bar{\mathbf{T}}}}G \quad\text{and}\quad k = \left(\frac{2G}{\tilde{G}}\mathbf{C}\cdot\bar{\mathbf{N}} + 1\right). \tag{3.8}$$

Similarly, the scalar strain rate measure $\dot{\varepsilon}$ is given by

$$\dot{\varepsilon} = \left(\frac{2G}{\tilde{G}}\mathbf{C} + \bar{\mathbf{N}}\right)\cdot\dot{\bar{\mathbf{H}}} + \frac{1}{\tilde{G}}\left(K - \frac{2}{3}G\right)\operatorname{tr}\dot{\bar{\mathbf{H}}}\operatorname{tr}\mathbf{C} \tag{3.9}$$

Damaged configurations

In the damaged configurations, the total strain rate contains extra damage strain as can be seen in Eq. (2.24). Following the plastic consistency condition, the equivalent stress rate $\dot{c}$ is given by

$$\begin{aligned}\dot{c} &= \tilde{G}\bar{\mathbf{N}}\cdot\dot{\mathbf{H}}^{\mathsf{el}} + \tilde{G}\mathbf{C}\cdot\dot{\mathbf{H}}^{\mathsf{el}} + \left(K-\frac{2}{3}G\right)\operatorname{tr}\dot{\mathbf{H}}^{\mathsf{el}}\operatorname{tr}\mathbf{C}\\ &= \mathbf{C}_3\cdot\dot{\mathbf{H}}^{\mathsf{el}}\\ &= \mathbf{C}_3\cdot\dot{\mathbf{H}} - \mathbf{R}^{-1}\mathbf{C}_3\mathbf{R}\cdot\dot{\mathbf{H}}^{\mathsf{pl}} - \mathbf{Q}^{\mathsf{el}-1}\mathbf{C}_3\mathbf{Q}^{\mathsf{el}}\cdot\dot{\mathbf{H}}^{\mathsf{da}}\\ &= \dot{\varepsilon}_1 - k_1\dot{\gamma} - k_2\dot{\mu}\end{aligned} \tag{3.10}$$

with the tensor

$$\mathbf{C}_3 = \left[\tilde{G}\bar{\mathbf{N}} + 2G\mathbf{C} + \left(K-\frac{2}{3}G\right)\mathbf{1}\operatorname{tr}\mathbf{C}\right] \tag{3.11}$$

and the scalars as

$$\dot{\varepsilon}_1 = \mathbf{C}_3\cdot\dot{\mathbf{H}}, \tag{3.12}$$

$$k_1 = \mathbf{R}^{-1}\mathbf{C}_3\mathbf{R}\cdot\mathbf{N} \tag{3.13}$$

and

$$k_2 = \mathbf{Q}^{\mathsf{el}-1}\mathbf{C}_3\mathbf{Q}^{\mathsf{el}}\cdot\left(\tilde{\alpha}\mathbf{1} + \tilde{\beta}\mathbf{N}\right). \tag{3.14}$$

The time derivative of the damage condition (Eq. (2.60)) results in the damage consistency condition $\dot{f}^{\mathsf{da}} = 0$, which makes sure that the current stress-state fulfills the current damage condition. Making use of the damage consistency condition, the rate of the equivalent damage stress is given as

$$\dot{\sigma} = \alpha\,\mathbf{C}\cdot\dot{\mathbf{T}} + \beta\frac{\sqrt{\boldsymbol{D}\mathbf{T}\cdot\boldsymbol{D}\mathbf{T}}}{\sqrt{\mathbf{T}\cdot\boldsymbol{D}\mathbf{T}}}\mathbf{N}\cdot\dot{\mathbf{T}}\,. \tag{3.15}$$

The rate of the Kirchhoff stress tensor in Eq. (2.60) is given by

$$
\begin{aligned}
\dot{\mathbf{T}} = {} & 2\left(G+\eta_2\mathrm{tr}\mathbf{A}^{\mathrm{da}}\right)\dot{\mathbf{H}}^{\mathrm{el}} + \left(K-\frac{2}{3}G+2\eta_1\,\mathrm{tr}\,\mathbf{A}^{\mathrm{da}}\right)\mathrm{tr}\,\dot{\mathbf{H}}^{\mathrm{el}}\mathbf{1} \\
& + \eta_3\left(\mathbf{A}^{\mathrm{da}}\cdot\dot{\mathbf{H}}^{\mathrm{el}}\right)\mathbf{1} + \eta_3\,\mathrm{tr}\,\dot{\mathbf{H}}^{\mathrm{el}}\mathbf{A}^{\mathrm{da}} + \eta_4\left(\dot{\mathbf{H}}^{\mathrm{el}}\mathbf{A}^{\mathrm{da}}+\mathbf{A}^{\mathrm{da}}\dot{\mathbf{H}}^{\mathrm{el}}\right) \\
& + 2\eta_2\,\mathrm{tr}\,\dot{\mathbf{H}}^{\mathrm{da}}\mathbf{A}^{\mathrm{el}} + 2\eta_1\,\mathrm{tr}\,\dot{\mathbf{H}}^{\mathrm{da}}\,\mathrm{tr}\,\mathbf{A}^{\mathrm{el}}\mathbf{1} + \eta_3\left(\dot{\mathbf{H}}^{\mathrm{da}}\cdot\mathbf{A}^{\mathrm{el}}\right)\mathbf{1} \\
& + \eta_3\,\mathrm{tr}\,\mathbf{A}^{\mathrm{el}}\dot{\mathbf{H}}^{\mathrm{da}} + \eta_4\left(\mathbf{A}^{\mathrm{el}}\dot{\mathbf{H}}^{\mathrm{da}}+\dot{\mathbf{H}}^{\mathrm{da}}\mathbf{A}^{\mathrm{el}}\right).
\end{aligned}
\tag{3.16}
$$

Furthermore, the scalar product between the normalized deviatoric stress tensor and the rate of the Kirchhoff stress tensor from the Eq. (3.15) can be determined as

$$
\begin{aligned}
\mathbf{N}\cdot\dot{\mathbf{T}} = {} & 2\left(G+\eta_2\,\mathrm{tr}\,\mathbf{A}^{\mathrm{da}}\right)\mathbf{N}\cdot\dot{\mathbf{H}}^{\mathrm{el}} + \eta_3\left(\mathbf{N}\cdot\mathbf{A}^{\mathrm{da}}\right)\mathrm{tr}\,\dot{\mathbf{H}}^{\mathrm{el}} \\
& + \eta_4\left(\mathbf{N}\mathbf{A}^{\mathrm{da}}+\mathbf{A}^{\mathrm{da}}\mathbf{N}\right)\cdot\dot{\mathbf{H}}^{\mathrm{el}} + 2\eta_2\left(\mathbf{N}\cdot\mathbf{A}^{\mathrm{el}}\right)\mathrm{tr}\,\dot{\mathbf{H}}^{\mathrm{da}} \\
& + \eta_3\,\mathrm{tr}\,\mathbf{A}^{\mathrm{el}}\mathbf{N}\cdot\dot{\mathbf{H}}^{\mathrm{da}} + \eta_4\left(\mathbf{N}\mathbf{A}^{\mathrm{el}}+\mathbf{A}^{\mathrm{el}}\mathbf{N}\right)\cdot\dot{\mathbf{H}}^{\mathrm{da}}.
\end{aligned}
\tag{3.17}
$$

Similarly, the scalar product between the tensor $\mathbf{C}$ (Eq. (2.43)), which characterizes the SD effect, and the rate of the Kirchhoff stress tensor is given as

$$
\begin{aligned}
\mathbf{C}\cdot\dot{\mathbf{T}} = {} & 2\left(G+\eta_2\mathrm{tr}\mathbf{A}^{\mathrm{da}}\right)\mathbf{C}\cdot\dot{\mathbf{H}}^{\mathrm{el}} + \eta_3\,\mathrm{tr}\,\mathbf{C}\left(\mathbf{A}^{\mathrm{da}}\cdot\dot{\mathbf{H}}^{\mathrm{el}}\right) \\
& + \left(K\,\mathrm{tr}\,\mathbf{C}-\frac{2}{3}G\,\mathrm{tr}\,\mathbf{C}+2\eta_1\,\mathrm{tr}\,\mathbf{C}\,\mathrm{tr}\,\mathbf{A}^{\mathrm{da}}\right)\mathrm{tr}\,\dot{\mathbf{H}}^{\mathrm{el}} \\
& + \eta_3\,\mathrm{tr}\,\dot{\mathbf{H}}^{\mathrm{el}}\left(\mathbf{A}^{\mathrm{da}}\cdot\mathbf{C}\right) + 2\eta_4\mathbf{C}\cdot\left(\dot{\mathbf{H}}^{\mathrm{el}}\mathbf{A}^{\mathrm{da}}\right) \\
& + 2\eta_2\,\mathrm{tr}\,\dot{\mathbf{H}}^{\mathrm{da}}\mathbf{C}\cdot\mathbf{A}^{\mathrm{el}} + 2\eta_1\,\mathrm{tr}\,\mathbf{C}\,\mathrm{tr}\,\dot{\mathbf{H}}^{\mathrm{da}}\,\mathrm{tr}\,\mathbf{A}^{\mathrm{el}} \\
& + \eta_3\,\mathrm{tr}\,\mathbf{C}\left(\dot{\mathbf{H}}^{\mathrm{da}}\cdot\mathbf{A}^{\mathrm{el}}\right) + \eta_3\,\mathrm{tr}\,\mathbf{A}^{\mathrm{el}}\mathbf{C}\cdot\dot{\mathbf{H}}^{\mathrm{da}} + 2\eta_4\mathbf{C}\cdot\left(\mathbf{A}^{\mathrm{el}}\dot{\mathbf{H}}^{\mathrm{da}}\right)
\end{aligned}
\tag{3.18}
$$

Furthermore, arranging the common terms in Eq. (3.18)

$$
\begin{aligned}
\mathbf{C}\cdot\dot{\mathbf{T}} = {} & \left(K\,\mathrm{tr}\,\mathbf{C} - \frac{2}{3}G\,\mathrm{tr}\,\mathbf{C} + 2\,\mathrm{tr}\,\mathbf{C}\eta_1\,\mathrm{tr}\,\mathbf{A}^{\mathrm{da}} + \eta_3\mathbf{A}^{\mathrm{da}}\cdot\mathbf{C}\right)\mathrm{tr}\,\dot{\mathbf{H}}^{\mathrm{el}} \\
& + \left([2G + 2\eta_2\mathrm{tr}\mathbf{A}^{\mathrm{da}}]\mathbf{C} + \eta_3\,\mathrm{tr}\,\mathbf{C}\mathbf{A}^{\mathrm{da}}\right)\cdot\dot{\mathbf{H}}^{\mathrm{el}} \\
& + 2\eta_4\mathbf{C}\cdot\left(\dot{\mathbf{H}}^{\mathrm{el}}\mathbf{A}^{\mathrm{da}}\right) + \left(2\eta_1\,\mathrm{tr}\,\mathbf{C}\,\mathrm{tr}\,\mathbf{A}^{\mathrm{el}} + 2\eta_2\mathbf{C}\cdot\mathbf{A}^{\mathrm{el}}\right)\mathrm{tr}\,\dot{\mathbf{H}}^{\mathrm{da}} \\
& + \eta_3\,\mathrm{tr}\,\mathbf{C}\left(\dot{\mathbf{H}}^{\mathrm{da}}\cdot\mathbf{A}^{\mathrm{el}}\right) + \eta_3\,\mathrm{tr}\,\mathbf{A}^{\mathrm{el}}\mathbf{C}\cdot\dot{\mathbf{H}}^{\mathrm{da}} \\
& + 2\eta_4\mathbf{C}\cdot\left(\mathbf{A}^{\mathrm{el}}\dot{\mathbf{H}}^{\mathrm{da}}\right).
\end{aligned}
\tag{3.19}
$$

Taking the common terms from both the scalar product in Eq. (3.17) and Eq. (3.19), the rate of the equivalent damage stress can be further manipulated as

$$
\begin{aligned}
\dot{\sigma} = {} & \left[\frac{\alpha}{a}\left(K\,\mathrm{tr}\,\mathbf{C} - \frac{2}{3}G\,\mathrm{tr}\,\mathbf{C} + 2\,\mathrm{tr}\,\mathbf{C}\eta_1\,\mathrm{tr}\,\mathbf{A}^{\mathrm{da}} + \eta_3\mathbf{A}^{\mathrm{da}}\cdot\mathbf{C}\right)\right. \\
& \quad \left. + \beta_k\mathbf{N}\cdot\mathbf{A}^{\mathrm{da}}\right]\mathrm{tr}\,\dot{\mathbf{H}}^{\mathrm{el}} \\
& + \left[\frac{\alpha}{a}\left([2G + 2\eta_2\mathrm{tr}\mathbf{A}^{\mathrm{da}}]\mathbf{C} + \eta_3\,\mathrm{tr}\,\mathbf{C}\mathbf{A}^{\mathrm{da}} + 2\eta_4\mathbf{A}^{\mathrm{da}}\mathbf{C}\right)\right. \\
& \quad \left. + \beta_k\left(2G + 2\eta_2\,\mathrm{tr}\,\mathbf{A}^{\mathrm{da}}\right)\mathbf{N} + \beta_k\eta_4\left(\mathbf{N}\mathbf{A}^{\mathrm{da}} + \mathbf{A}^{\mathrm{da}}\mathbf{N}\right)\right]\cdot\dot{\mathbf{H}}^{\mathrm{el}} \\
& + \left[\frac{\alpha}{a}\left(2\eta_1\,\mathrm{tr}\,\mathbf{C}\,\mathrm{tr}\,\mathbf{A}^{\mathrm{el}} + 2\eta_2\mathbf{C}\cdot\mathbf{A}^{\mathrm{el}}\right) + 2\beta_k\eta_2\mathbf{N}\cdot\mathbf{A}^{\mathrm{el}}\right]\mathrm{tr}\,\dot{\mathbf{H}}^{\mathrm{da}} \\
& + \left[\frac{\alpha}{a}\left(\eta_3\,\mathrm{tr}\,\mathbf{A}^{\mathrm{el}}\mathbf{C} + 2\eta_4\mathbf{A}^{\mathrm{el}}\mathbf{C} + \eta_3\,\mathrm{tr}\,\mathbf{C}\mathbf{A}^{\mathrm{el}}\right)\right. \\
& \quad \left. + \beta_k\eta_3\,\mathrm{tr}\,\mathbf{A}^{\mathrm{el}}\mathbf{N} + \beta_k\eta_4\left(\mathbf{N}\mathbf{A}^{\mathrm{el}} + \mathbf{A}^{\mathrm{el}}\mathbf{N}\right)\right]\cdot\dot{\mathbf{H}}^{\mathrm{da}}.
\end{aligned}
\tag{3.20}
$$

As shown above (Eq. (2.24)), the strain rate in the damaged configurations is additively decomposed as

$$
\dot{\mathbf{H}}^{\mathrm{el}} = \dot{\mathbf{H}} - \mathbf{R}^{-1}\dot{\mathbf{H}}^{\mathrm{pl}}\mathbf{R} - \mathbf{Q}^{\mathrm{el}-1}\dot{\mathbf{H}}^{\mathrm{da}}\mathbf{Q}^{\mathrm{el}}.
\tag{3.21}
$$

Furthermore, replacing $\mathrm{tr}\,\dot{\mathbf{H}}^{\mathrm{el}}$ and $\mathrm{tr}\,\dot{\mathbf{H}}^{\mathrm{da}}$ in Eq. (3.20) with $\mathbf{1}\cdot\dot{\mathbf{H}}^{\mathrm{el}}$ and $\mathbf{1}\cdot\dot{\mathbf{H}}^{\mathrm{da}}$, respectively, Eq. (3.20) is simplified and can be written in a compact form as

$$\dot{\sigma} = \mathbf{C}_1 \cdot \dot{\mathbf{H}} - \mathbf{R}^{-1}\mathbf{C}_1\mathbf{R} \cdot \dot{\mathbf{H}}^{\mathsf{pl}} - \left(\mathbf{Q}^{\mathsf{el}-1}\mathbf{C}_1\mathbf{Q}^{\mathsf{el}} - \mathbf{C}_2\right) \cdot \dot{\mathbf{H}}^{\mathsf{da}} \tag{3.22}$$

where $\mathbf{C}_1$ and $\mathbf{C}_2$ are the two second-order tensors given as

$$\begin{aligned}
\mathbf{C}_1 = \Bigg[\frac{\alpha}{a}\left(K \operatorname{tr}\mathbf{C} - \frac{2}{3}G \operatorname{tr}\mathbf{C} + 2\operatorname{tr}\mathbf{C}\eta_1 \operatorname{tr}\mathbf{A}^{\mathsf{da}} + \eta_3\mathbf{A}^{\mathsf{da}} \cdot \mathbf{C}\right) \\
+ \beta_k \mathbf{N} \cdot \mathbf{A}^{\mathsf{da}}\Bigg]\mathbf{1} + \frac{\alpha}{a}\left[\left(2G + 2\eta_2 \operatorname{tr}\mathbf{A}^{\mathsf{da}}\right)\mathbf{C} + \eta_3 \operatorname{tr}\mathbf{C}\mathbf{A}^{\mathsf{da}}\right. \\
\left. + 2\eta_4 \mathbf{A}^{\mathsf{da}} \operatorname{tr}\mathbf{C}\right] + \beta_k\left(2G + 2\eta_2 \operatorname{tr}\mathbf{A}^{\mathsf{da}}\right)\mathbf{N} \\
+ \beta_k\eta_4\left(\mathbf{N}\mathbf{A}^{\mathsf{da}} + \mathbf{A}^{\mathsf{da}}\mathbf{N}\right)
\end{aligned} \tag{3.23}$$

and

$$\begin{aligned}
\mathbf{C}_2 = \left[\frac{\alpha}{a}\left(2\eta_1 \operatorname{tr}\mathbf{C} \operatorname{tr}\mathbf{A}^{\mathsf{el}} + 2\eta_2\mathbf{C} \cdot \mathbf{A}^{\mathsf{el}}\right) + 2\beta_k\eta_2\mathbf{N} \cdot \mathbf{A}^{\mathsf{el}}\right]\mathbf{1} \\
+ \frac{\alpha}{a}\left(\eta_3 \operatorname{tr}\mathbf{A}^{\mathsf{el}}\mathbf{C} + 2\eta_4\mathbf{A}^{\mathsf{el}}\mathbf{C} + \eta_3 \operatorname{tr}\mathbf{C}\mathbf{A}^{\mathsf{el}}\right) \\
+ \beta_k\eta_3 \operatorname{tr}\mathbf{A}^{\mathsf{el}}\mathbf{N} + \beta_k\eta_4\left(\mathbf{N}\mathbf{A}^{\mathsf{el}} + \mathbf{A}^{\mathsf{el}}\mathbf{N}\right).
\end{aligned} \tag{3.24}$$

Furthermore, utilizing the Eq. (2.51) and Eq. (2.62), the rate of the equivalent damage stress (Eq. (3.22)) can be written as follows

$$\dot{\sigma} = \dot{\varepsilon}_2 - k_3\dot{\gamma} - k_4\dot{\mu} \tag{3.25}$$

with the scalar coefficients

$$\dot{\varepsilon}_2 = \mathbf{C}_1 \cdot \dot{\mathbf{H}}, \tag{3.26}$$

$$k_3 = \mathbf{R}^{-1}\mathbf{C}_1\mathbf{R} \cdot \dot{\mathbf{N}} \tag{3.27}$$

and

$$k_4 = \left(\mathbf{Q}^{\mathsf{el}-1}\mathbf{C}_1\mathbf{Q}^{\mathsf{el}} - \mathbf{C}_2\right) \cdot \left(\frac{\tilde{\alpha}}{\sqrt{3}}\mathbf{1} + \delta\tilde{\beta}\mathbf{N}\right). \tag{3.28}$$

3.2.2 Numerical integration

The task of the numerical integration algorithm is to calculate the incremental quantities over each incremental load or the time increment, using the current values of the deformations, stresses and other state variables together with the constitutive equations. Since the inelastic constitutive relations are formulated in rate form, it is necessary to do time discretization over the time interval $\Delta t = t_{\mathsf{n+1}} - t_n$. In the current work, all the quantities are known at time $t_n = t$. Furthermore, a suitable integration algorithm has to be chosen to numerically integrate the constitutive rate equations discussed above. For this, some implicit and explicit methods are possible. Wilkins [118] introduced the radial return technique for the elastic-plastic problems, which uses an elastic predictor followed by plastic corrector. It was further generalized by Krieg and Krieg [72] and Hughes [63]. Furthermore, Doghri [47] and de Souza Neto et al. [45] used radial return method for solving elastoplastic damage problems in ductile metals. However, these methods are primarily applicable to associated material laws, which makes them less suitable for the theory of the continuum damage model presented here. An explicit method using inelastic predictor followed by elastic corrector integration algorithm is used in this work, which gives good approximation of the succeeding yield surface in a less number of increments. This method was introduced by Nemat-Nasser and Li [88] for the elastic-plastic problems and then extensively used in [23, 24] for solving elastic-plastic-damage problems in ductile metals. In this method, all of the incremental deformation is first considered as an inelastic one (plastic-damage) and then subsequently corrected to account for the elastic deformation, which generally is small for metals. One of the advantages of this method is the numerical stability for both small and large step sizes. In the following part, using the scalar rate equations for both configurations, the numerical integration is discussed in detail.

Fictitious undamaged configurations

The effective plastic strain rate is determined in this configuration. For that purpose, the scalar rate equation given in Eq. (3.7) is numerically integrated over the time interval $t_{\mathsf{n}} < \Theta \leq t_{\mathsf{n+1}}$ with $t_{\mathsf{n+1}} = t_n + \Delta t$, which leads to

$$\mathit{\Delta} c = \tilde{G}k\left(\frac{1}{k}\mathit{\Delta}\varepsilon - \mathit{\Delta}\gamma\right). \tag{3.29}$$

In the inelastic predictor step, assuming that the total strain increment is only plastic, the effective plastic strain increment is given by

$$\mathit{\Delta}\gamma_{\mathrm{pr}} = \frac{1}{k}\mathit{\Delta}\varepsilon \tag{3.30}$$

and the predictor of the associated effective stress is given as

$$c_{\mathsf{pr}} = c\left(\gamma_{\mathsf{n}} + \mathit{\Delta}\gamma_{\mathrm{pr}}\right). \tag{3.31}$$

Obviously, this assumption results to an overestimation of increment of both the effective plastic strain $\mathit{\Delta}\gamma$ and the corresponding effective stress $\mathit{\Delta}c$. This overestimation is corrected by an elastic corrector step as

$$\mathit{\Delta}_{\mathsf{er}}\gamma = \frac{1}{k}\mathit{\Delta}\varepsilon - \mathit{\Delta}\gamma \tag{3.32}$$

and

$$\mathit{\Delta}_{\mathsf{er}}c = c_{\mathsf{pr}} - c_{\mathsf{n+1}} = c_{\mathsf{pr}} - c_{\mathsf{n}} - \tilde{G}k\mathit{\Delta}_{\mathsf{er}}\gamma. \tag{3.33}$$

In addition, as shown in Fig. 3.1, another way to estimate the error of the effective stress is

$$\mathit{\Delta}_{\mathsf{er}}c \approx \frac{\partial c}{\partial \gamma_{\mathsf{pr}}}\mathit{\Delta}_{\mathsf{er}}\gamma. \tag{3.34}$$

Now, from equations Eq. (3.33) and Eq. (3.34), the error of effective plastic strain increment can be calculated as

$$\mathit{\Delta}_{\mathsf{er}}\gamma = \left(c_{\mathsf{pr}} - c_{\mathsf{n}}\right)\left[\frac{\partial c}{\partial \gamma_{pr}} + \tilde{G}k\right]^{-1}. \tag{3.35}$$

Thus, the total current effective plastic strain increment is given as

$$\varDelta\gamma = \frac{\varDelta\varepsilon}{k} - (c_{\mathsf{pr}} - c_{\mathsf{n}}) \left[\frac{\partial c}{\partial \gamma_{pr}} + \tilde{G}k \right]^{-1} . \tag{3.36}$$

Similarly, the total current effective plastic strain is determined as

$$\gamma_{\mathsf{n+1}} = \gamma_{\mathsf{n}} + \varDelta\gamma. \tag{3.37}$$

and the current effective stress can be calculated using

$$c_{\mathsf{n+1}} = c_{\mathsf{n}} + \varDelta c\,. \tag{3.38}$$

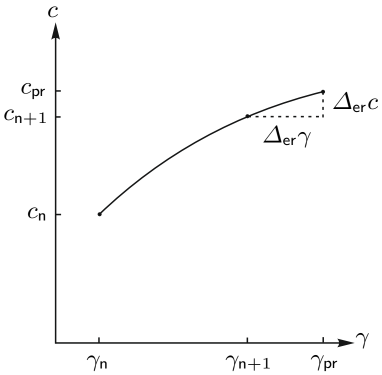

Figure 3.1: Illustration of the integration algorithm.

Damaged configurations

Similar to the integration algorithm in the undamaged configurations, the scalar rate equations Eq. (3.10) and Eq. (3.22) are integrated over the time interval $t_{\mathsf{n}} < \varTheta \leq t_{\mathsf{n+1}}$ with $t_{\mathsf{n+1}} = t_n + \varDelta t$ leading to

$$\varDelta c = \varDelta\varepsilon_1 - k_1\varDelta\gamma - k_2\varDelta\mu \tag{3.39}$$

and

$$\mathit{\Delta}\sigma = \mathit{\Delta}\varepsilon_2 - k_3 \mathit{\Delta}\gamma - k_4 \mathit{\Delta}\mu. \tag{3.40}$$

It is assumed that in the inelastic predictor step, all the elastic increments $\mathit{\Delta}\varepsilon^{\mathrm{el}} = \mathbf{0}$, Eq. (3.39) and Eq. (3.40) lead to

$$\boldsymbol{k}\mathit{\Delta}\boldsymbol{f}_{\mathsf{pr}} = \mathit{\Delta}\boldsymbol{e} \tag{3.41}$$

where $\boldsymbol{k}$ is the matrix with coefficients

$$\boldsymbol{k} = \begin{bmatrix} k_1 & k_2 \\ k_3 & k_4 \end{bmatrix}, \tag{3.42}$$

$\boldsymbol{f}_{\mathsf{pr}}$ denotes the vector of inelastic predictor strain increments

$$\mathit{\Delta}\boldsymbol{f}_{\mathsf{pr}} = \begin{bmatrix} \mathit{\Delta}\gamma_{\mathsf{pr}} \\ \mathit{\Delta}\mu_{\mathsf{pr}} \end{bmatrix} \tag{3.43}$$

and $\mathit{\Delta}\boldsymbol{e}$ represents the vector of strain increments of the undamaged matrix and the damaged material, respectively

$$\mathit{\Delta}\boldsymbol{e} = \begin{bmatrix} \mathit{\Delta}\varepsilon_1 \\ \mathit{\Delta}\varepsilon_2 \end{bmatrix}. \tag{3.44}$$

At the end of the time increment, the predictor equivalent stresses are given as

$$c_{\mathsf{pr}} = c\left(\gamma_{\mathsf{n}} + \mathit{\Delta}\gamma_{\mathsf{pr}}\right) \tag{3.45}$$

and

$$\sigma_{\mathsf{pr}} = \sigma\left(\mu_{\mathsf{n}} + \mathit{\Delta}\mu_{\mathsf{pr}}\right). \tag{3.46}$$

Again, these assumptions result in overestimation of the equivalent inelastic strain increments and the respective equivalent stresses, the corresponding errors are approximated by the elastic corrector steps

$$\mathit{\Delta}_{\mathsf{er}}c \approx \frac{\partial c}{\partial \gamma_{\mathsf{pr}}} \mathit{\Delta}_{\mathsf{er}}\gamma = c_{\mathsf{pr}} - c_{\mathsf{n+1}} = c_{\mathsf{pr}} - c_{\mathsf{n}} - \mathit{\Delta}c \tag{3.47}$$

and

$$\mathit{\Delta}_{\mathsf{er}}\sigma \approx \frac{\partial \sigma}{\partial \mu_{\mathsf{pr}}} \mathit{\Delta}_{\mathsf{er}}\mu = \sigma_{\mathsf{pr}} - \sigma_{\mathsf{n+1}} = \sigma_{\mathsf{pr}} - \sigma_{\mathsf{n}} - \mathit{\Delta}\sigma. \tag{3.48}$$

Using Eqs. (3.39), (3.40), (3.47) and (3.48) the errors in inelastic strains $\mathit{\Delta}_{\mathsf{er}}\gamma$ and $\mathit{\Delta}_{\mathsf{er}}\mu$ can be calculated using the system of equations as

$$\boldsymbol{a}\, \mathit{\Delta}_{\mathsf{er}}\boldsymbol{f} = \mathit{\Delta}\boldsymbol{c}_{\mathsf{pr}}. \tag{3.49}$$

with

$$\boldsymbol{a} = \begin{bmatrix} k_1 + \frac{\partial c}{\partial \gamma_{\mathsf{pr}}} & k_2 \\ k_3 & k_4 + \frac{\partial \sigma}{\partial \mu_{\mathsf{pr}}} \end{bmatrix}, \tag{3.50}$$

$$\mathit{\Delta}_{\mathsf{er}}\boldsymbol{f} = \begin{bmatrix} \mathit{\Delta}_{\mathsf{er}}\gamma \\ \mathit{\Delta}_{\mathsf{er}}\mu \end{bmatrix} \tag{3.51}$$

and

$$\mathit{\Delta}\boldsymbol{c}_{\mathsf{pr}} = \begin{bmatrix} c_{\mathsf{pr}} - c_{\mathsf{n}} \\ \sigma_{\mathsf{pr}} - \sigma_{\mathsf{n}} \end{bmatrix}. \tag{3.52}$$

Solving the given system of equations, the increment of equivalent strains is given by

$$\mathit{\Delta}\boldsymbol{f} = \mathit{\Delta}\boldsymbol{f}_{\mathsf{pr}} - \mathit{\Delta}\boldsymbol{f}_{\mathsf{er}}. \tag{3.53}$$

Hence, the current equivalent inelastic strains are calculated by

$$\gamma_{\mathsf{n+1}} = \gamma_{\mathsf{n}} + \mathit{\Delta}\gamma \text{ and } \mu_{\mathsf{n+1}} = \mu_{\mathsf{n}} + \mathit{\Delta}\mu. \tag{3.54}$$

and the corresponding equivalent stresses as

$$c_{\mathsf{n+1}} = c_{\mathsf{n}} + \mathit{\Delta}c \text{ and } \sigma_{\mathsf{n+1}} = \sigma_{\mathsf{n}} + \mathit{\Delta}\sigma. \tag{3.55}$$

3.2.3 Tensorial quantities

Fictitious undamaged configurations

With the help of the determined effective plastic strain, the respective tensorial quantities are calculated. The increment of the effective plastic strain tensor Eq. (2.51) is written as

$$\mathit{\Delta}\bar{\mathbf{H}}^{\mathsf{pl}} = \mathit{\Delta}\gamma\bar{\mathbf{N}}_{\mathsf{m}} \tag{3.56}$$

where the mean value of the normalized stress tensor $\bar{\mathbf{N}}_{\mathsf{m}}$ is calculated using the midpoint method as

$$\bar{\mathbf{N}}_{\mathsf{m}} = \frac{1}{2}\left(\bar{\mathbf{N}}_{\mathsf{n}} + \bar{\mathbf{N}}_{\mathsf{n+1}}\right). \tag{3.57}$$

It can be seen that at current time step, $\bar{\mathbf{N}}_{\mathsf{n}}$ is known but $\bar{\mathbf{N}}_{\mathsf{n+1}}$ is unknown. Using the definition of the normalized stress tensor (Eq. (2.52))

$$\left\|\boldsymbol{D}\,\bar{\mathbf{T}}_{\mathsf{n+1}}\right\|\bar{\mathbf{N}}_{\mathsf{n+1}} = \boldsymbol{D}\,\bar{\mathbf{T}}_{\mathsf{n+1}} \text{ and } \left\|\boldsymbol{D}\,\bar{\mathbf{T}}_{\mathsf{n}}\right\|\bar{\mathbf{N}}_{\mathsf{n}} = \boldsymbol{D}\,\bar{\mathbf{T}}_{\mathsf{n}} \tag{3.58}$$

the change in the normalized effective deviatoric stress tensor is given as

$$\begin{aligned}\left\|\boldsymbol{D}\,\bar{\mathbf{T}}_{\mathsf{n+1}}\right\|\bar{\mathbf{N}}_{\mathsf{n+1}} - \left\|\boldsymbol{D}\,\bar{\mathbf{T}}_{\mathsf{n}}\right\|\bar{\mathbf{N}}_{\mathsf{n}} &= \boldsymbol{D}\left(\bar{\mathbf{T}}_{\mathsf{n+1}} - \bar{\mathbf{T}}_{\mathsf{n}}\right)\\ &= \boldsymbol{D}\Big[2G\dot{\bar{\mathbf{H}}} - G\mathit{\Delta}\gamma\left(\bar{\mathbf{N}}_{\mathsf{n}} + \bar{\mathbf{N}}_{\mathsf{n+1}}\right)\\ &\quad + \left(K - \frac{2}{3}G\right)\operatorname{tr}\dot{\bar{\mathbf{H}}}\mathbf{1}\Big].\end{aligned} \tag{3.59}$$

After some manipulations

$$\begin{aligned}\bar{\mathbf{N}}_{\mathsf{n+1}} = \frac{1}{\left\|\boldsymbol{D}\,\bar{\mathbf{T}}_{\mathsf{n+1}}\right\|}\Big[&2G\boldsymbol{D}\dot{\bar{\mathbf{H}}} + \left(K - \frac{2}{3}G\right)\operatorname{tr}\dot{\bar{\mathbf{H}}}\boldsymbol{D}\mathbf{1}\\ &+ \left\|\boldsymbol{D}\,\bar{\mathbf{T}}_{\mathsf{n}}\right\|\bar{\mathbf{N}}_{\mathsf{n}} - G\mathit{\Delta}\gamma\boldsymbol{D}\left(\bar{\mathbf{N}}_{\mathsf{n}} + \bar{\mathbf{N}}_{\mathsf{n+1}}\right)\Big].\end{aligned} \tag{3.60}$$

As we can see in Eq. (3.60), $\bar{\mathbf{N}}_{\mathsf{n+1}}$ also appears on the right side of the equation, which is not known at the current step. One possibility is to use the approach by Nemat-Nasser and Li [88], where it was shown that the final orientation of the stress direction is coaxial with the deviatoric part of the total deformation rate tensor. So using this approach, $\bar{\mathbf{N}}^{\mathsf{f}}$ is given by

$$\bar{\mathbf{N}}^{\mathsf{f}} = \frac{\operatorname{dev}\mathit{\Delta}\mathbf{H}}{\|\operatorname{dev}\mathit{\Delta}\mathbf{H}\|}. \tag{3.61}$$

Hence, replacing $\bar{\mathbf{N}}_{\mathsf{n}+1}$ with $\bar{\mathbf{N}}^{\mathsf{f}}$, the new normalized effective deviatoric stress tensor $\bar{\mathbf{N}}_{\mathsf{n}+1}$ in Eq. (3.60) can be determined. Consequently, the associated plastic strain increment (Eq. (3.56)) can be calculated. Furthermore, with $\mathit{\Delta}\bar{\mathbf{H}}^{\mathsf{pl}}$ in hand, the elastic strain increment tensor is given as

$$\mathit{\Delta}\mathbf{H}^{\mathsf{el}} = \mathit{\Delta}\mathbf{H} - \mathit{\Delta}\bar{\mathbf{H}}^{\mathsf{pl}}. \tag{3.62}$$

The increment of the strain rate (Eq. (2.9)) is given as

$$\begin{aligned} \mathit{\Delta}\mathbf{H} = &= \frac{1}{2}\hat{\mathbf{Q}}^{-1}\left(\mathbf{Q} - \mathbf{Q}_{\mathsf{n}-1}\right) \\ &= \left(\mathbf{Q} + \mathbf{Q}_{\mathsf{n}-1}\right)^{-1}\left(\mathbf{Q} - \mathbf{Q}_{\mathsf{n}-1}\right). \end{aligned} \tag{3.63}$$

Furthermore, the elastic part of the metric transformation tensor can be calculated as

$$\mathbf{Q}^{\mathsf{el}} = \mathbf{Q}^{\mathsf{el}}_{\mathsf{n}-1}\left(\mathbf{1} - \mathit{\Delta}\mathbf{H}^{\mathsf{el}}\right)^{-1}\left(\mathbf{1} + \mathit{\Delta}\mathbf{H}^{\mathsf{el}}\right). \tag{3.64}$$

The elastic part of the Hencky strain tensor (Eq. (2.18)) is determined using the Padé approximation as done by Brünig [20, 21].

Damaged configurations

Analogous to the fictitious undamaged configurations, the tensorial quantities in the current damaged configurations are determined using the inelastic strain increments $\mathit{\Delta}\gamma$ and $\mathit{\Delta}\mu$. The damage evolution (Eq. (2.62)) law is given as

$$\Delta\mathbf{H}^{\mathrm{da}} = \Delta\mu\left(\frac{\tilde{\alpha}}{\sqrt{3}}\mathbf{1} + \tilde{\beta}\mathbf{N}_{\mathrm{m}}\right) \tag{3.65}$$

with the normalized mean value

$$\mathbf{N}_{\mathrm{m}} = \frac{1}{2}\left(\mathbf{N}_{\mathrm{n}} + \mathbf{N}_{\mathrm{n+1}}\right). \tag{3.66}$$

Furthermore, as illustrated above, the change in the normalized deviatoric stress tensor can be calculated as

$$\begin{aligned} \|\boldsymbol{D}\,\mathbf{T}_{\mathrm{n+1}}\|\mathbf{N}_{\mathrm{n+1}} - \|\boldsymbol{D}\,\mathbf{T}_{\mathrm{n}}\|\mathbf{N}_{\mathrm{n}} &= \boldsymbol{D}\left(\mathbf{T}_{\mathrm{n+1}} - \mathbf{T}_{\mathrm{n}}\right) \\ &= \boldsymbol{D}\Big[2G\dot{\bar{\mathbf{H}}} - 2G\Delta\gamma\bar{\mathbf{N}}_{\mathrm{m}} \\ &\qquad -2G\Delta\mu\left(\frac{\tilde{\alpha}}{\sqrt{3}}\mathbf{1} + \tilde{\beta}\mathbf{N}_{\mathrm{m}}\right) \\ &\qquad +\left(K - \frac{2}{3}G\right)\operatorname{tr}\dot{\bar{\mathbf{H}}}\mathbf{1}\Big]. \end{aligned} \tag{3.67}$$

It is assumed that at the initiation of damage, significant amount of plastic deformations are already present in the material. Thus, the change in the effective normalized deviatoric stress is taken to be negligible, i.e., $\bar{\mathbf{N}}_{\mathrm{n+1}} = \bar{\mathbf{N}}_{\mathrm{n}} = \bar{\mathbf{N}}_{\mathrm{m}}$. In addition, with the assumption $\mathbf{N}_{\mathrm{n+1}} \approx \bar{\mathbf{N}}^{\mathrm{f}}$, and with further manipulations, the new stress direction in the damaged configurations is determined as

$$\begin{aligned} \mathbf{N}_{\mathrm{n+1}} = \frac{1}{\|\boldsymbol{D}\,\mathbf{T}_{\mathrm{n+1}}\|}\Big[&2G\boldsymbol{D}\left(\dot{\mathbf{H}} - \Delta\gamma\bar{\mathbf{N}}_{\mathrm{n}}\right) + \left(K - \frac{2}{3}G\right)\operatorname{tr}\dot{\bar{\mathbf{H}}}\boldsymbol{D}\mathbf{1} \\ &+\|\boldsymbol{D}\,\mathbf{T}_{\mathrm{n}}\|\mathbf{N}_{\mathrm{n}} - G\Delta\mu\boldsymbol{D}\left(\frac{2\tilde{\alpha}}{\sqrt{3}}\mathbf{1} + \tilde{\beta}\bar{\mathbf{N}}^{\mathrm{f}} + \tilde{\beta}\mathbf{N}_{\mathrm{n}}\right)\Big]. \end{aligned} \tag{3.68}$$

Moreover, using the new stress direction, the mean value of the deviatoric stress direction is determined. Hence, the two inelastic strains increment $\Delta\bar{\mathbf{H}}^{\mathrm{pl}}$ (Eq. (3.56)) and $\Delta\mathbf{H}^{\mathrm{da}}$ (Eq. (3.65)) are calculated. The metric transformation tensor $\overset{\star}{\mathbf{R}}$ is given by

$$\overset{\star}{\mathbf{R}} = \overset{\star}{\mathbf{R}}_{\mathrm{n-1}}\left(1 - \Delta\mathbf{H}^{\mathrm{da}}\right)^{-1}\left(1 + \Delta\mathbf{H}^{\mathrm{da}}\right). \tag{3.69}$$

The elastic Hencky strain increment is determined by the integrated rate equation (2.24) as

$$\Delta \mathbf{H}^{\mathsf{el}} = \Delta \mathbf{H} - \mathbf{R}^{-1} \Delta \bar{\mathbf{H}}^{\mathsf{pl}} \mathbf{R} - \mathbf{Q}^{\mathsf{el}-1} \Delta \mathbf{H}^{\mathsf{da}} \mathbf{Q}^{\mathsf{el}}. \tag{3.70}$$

The current metric transformation tensors $\mathbf{Q}$ and $\mathbf{R}$ are still unknown. The metric transformation tensor in the damaged configurations is given as

$$\mathbf{R} = \mathbf{Q}^{\mathsf{el}-1} \overset{\star}{\mathbf{R}} \mathbf{Q}^{\mathsf{el}}. \tag{3.71}$$

Numerical simulations have shown that the elastic metric transformation tensor $\mathbf{Q}^{\mathsf{el}}$ is approximately equal to $\mathbf{1}$. Moreover, the calculation of the elastic metric transformation tensor is analogous to Eq. (3.64) and the total elastic Hencky strain $\mathbf{A}^{\mathsf{el}}$ as well as the total Hencky damage strain $\mathbf{A}^{\mathsf{el}}$ are determined using with the Padé approximation.

3.2.4 Consistent tangent moduli

One of the essential steps in the numerical implementation is the determination of the consistent tangent moduli. This ensures quadratic convergence in the global finite element method where Newton-Raphson scheme is implemented to obtain the solution of the incremental problem. In the following section, two consistent tangent moduli are introduced.

Fictitious undamaged configurations

Making use of the plastic consistency condition Eq. (3.7) and the plastic constitutive law

$$\mathrm{d}c = \frac{\partial c}{\partial \gamma} \mathrm{d}\gamma = \tilde{G} k \left(\frac{1}{k} \Delta \varepsilon - \Delta \gamma \right). \tag{3.72}$$

Furthermore, with Eq. (3.9) and Eq. (3.72)

$$\begin{aligned} \mathrm{d}\gamma = \left[\frac{\partial c}{\partial \gamma} + \tilde{G}k\right]^{-1} \tilde{G} \Bigg[& \left(\frac{2G}{\tilde{G}}\boldsymbol{\mathsf{C}} + \bar{\boldsymbol{\mathsf{N}}}\right) \cdot \dot{\boldsymbol{\mathsf{H}}} \\ & + \frac{1}{\tilde{G}}\left(K - \frac{2}{3}G\right) \operatorname{tr} \dot{\boldsymbol{\mathsf{H}}} \operatorname{tr} \boldsymbol{\mathsf{C}} \Bigg] . \end{aligned} \tag{3.73}$$

The differential of the rate equation Eq. (2.19) can be written as

$$\begin{aligned} \mathrm{d}\bar{\boldsymbol{\mathsf{H}}}^{\mathsf{el}} &= \mathrm{d}\bar{\boldsymbol{\mathsf{H}}} - \bar{\boldsymbol{\mathsf{N}}}_{\mathsf{m}} \mathrm{d}\gamma \\ &= \Bigg[\boldsymbol{1} \otimes \boldsymbol{1} - \left(\frac{\partial c}{\partial \gamma} + \tilde{G}k\right)^{-1} \left(\tilde{G}\bar{\boldsymbol{\mathsf{N}}}_{\mathsf{m}} \otimes \bar{\boldsymbol{\mathsf{N}}} + 2G\bar{\boldsymbol{\mathsf{N}}}_{\mathsf{m}} \otimes \boldsymbol{\mathsf{C}}\right) \\ &\quad - \left(\frac{\partial c}{\partial \gamma} + \tilde{G}k\right)^{-1} \left(K - \frac{2}{3}G\right) \operatorname{tr} \boldsymbol{\mathsf{C}}\, \bar{\boldsymbol{\mathsf{N}}}_{\mathsf{m}} \otimes \boldsymbol{1} \Bigg] \mathrm{d}\bar{\boldsymbol{\mathsf{H}}}. \end{aligned} \tag{3.74}$$

In addition, substituting Eq. (3.74) in Eq. (2.42), the elastic-plastic tangent modulus without prior damage is given as

$$\begin{aligned} \bar{\mathbb{C}}^{\mathsf{ep}} = \bar{\mathbb{C}}^{\mathsf{el}} - \left(\frac{\partial c}{\partial \gamma} + \tilde{G}k\right)^{-1} \Bigg[& 2G\left(\tilde{G}\bar{\boldsymbol{\mathsf{N}}}_{\mathsf{m}} \otimes \bar{\boldsymbol{\mathsf{N}}} + 2G\bar{\boldsymbol{\mathsf{N}}}_{\mathsf{m}} \otimes \boldsymbol{\mathsf{C}}\right) + \\ & 2G\left(K - \frac{2}{3}G\right) \operatorname{tr} \boldsymbol{\mathsf{C}}\, \bar{\boldsymbol{\mathsf{N}}}_{\mathsf{m}} \otimes \boldsymbol{1} \Bigg] . \end{aligned} \tag{3.75}$$

Damaged configurations

Making use of the equation Eq. (3.49)

$$\mathrm{d}\boldsymbol{f}_{\mathsf{er}} = \boldsymbol{a}^{-1}\mathrm{d}\boldsymbol{c}_{\mathsf{pr}} = \boldsymbol{a}^{-1}\boldsymbol{h}\,\mathrm{d}\boldsymbol{f}_{\mathsf{pr}} \quad \text{with} \quad \boldsymbol{h} = \begin{bmatrix} \frac{\partial c}{\partial \gamma} & 0 \\ 0 & \frac{\partial \sigma}{\partial \mu} \end{bmatrix} . \tag{3.76}$$

Substituting Eq. (3.76) into Eq. (3.53) and using Eq. (3.43)

$$\mathrm{d}\boldsymbol{f} = \mathrm{d}\boldsymbol{f}_{\mathsf{pr}} - \mathrm{d}\boldsymbol{f}_{\mathsf{er}} = \left(\boldsymbol{k}^{-1} - \boldsymbol{a}^{-1}\,\boldsymbol{h}\,\boldsymbol{k}^{-1}\right)\mathrm{d}\boldsymbol{e} = \boldsymbol{b}\,\mathrm{d}\boldsymbol{e} \tag{3.77}$$

with

$$\mathrm{d}\boldsymbol{e} = \begin{bmatrix} \mathrm{d}\varepsilon_1 \\ \mathrm{d}\varepsilon_2 \end{bmatrix}, \mathrm{d}\varepsilon_1 = \mathbf{C}_3 \cdot \dot{\mathbf{H}} \quad \text{and} \quad \mathrm{d}\varepsilon_2 = \mathbf{C}_1 \cdot \dot{\mathbf{H}}. \tag{3.78}$$

Furthermore, substituting the differential of the total strain rate tensor (Eq. (2.24)), the plastic flow rule and the damage rule in the total differential of the Kirchhoff stress tensor $\mathbf{T}$ (Eq. (2.55)), the elastic-plastic-damage tangent modulus $\mathbb{C}^{\mathsf{epd}}$ is given as

$$\begin{aligned} \mathrm{d}\mathbf{T} = {} & \mathbb{C}^{\mathsf{el}}\mathrm{d}\mathbf{H} - \left[\mathbb{C}^{\mathsf{el}}\left(\mathbf{R}^{-1}\bar{\mathbf{N}}_{\mathsf{m}}\mathbf{R}\right) \otimes (b_{11}\mathbf{C}_3 + b_{12}\mathbf{C}_1)\right]\mathrm{d}\mathbf{H} \\ & - \left[\mathbb{C}^{\mathsf{el}}\left(\frac{\tilde{\alpha}}{\sqrt{3}}\mathbf{1} + \tilde{\beta}\mathbf{Q}^{\mathsf{el}-1}\mathbf{N}_{\mathsf{m}}\mathbf{Q}^{\mathsf{el}}\right) \otimes (b_{21}\mathbf{C}_3 + b_{22}\mathbf{C}_1)\right]\mathrm{d}\mathbf{H} \\ & + \left[\mathbb{C}^{\mathsf{da}}\left(\frac{\tilde{\alpha}}{\sqrt{3}}\mathbf{1} + \tilde{\beta}\mathbf{N}_{\mathsf{m}}\right) \otimes (b_{21}\mathbf{C}_3 + b_{22}\mathbf{C}_1)\right]\mathrm{d}\mathbf{H} \\ = {} & \mathbb{C}^{\mathsf{epd}}\mathrm{d}\mathbf{H}. \end{aligned} \tag{3.79}$$

4 Experimental aspects

Experimental data are necessary to identify material parameters and to validate the proposed continuum damage model. In this Chapter, a brief overview of the experimental setups used to conduct uniaxial and biaxial tests is given. Furthermore, the detailed description of the digital image correlation (DIC) functionality, employed for recording displacements during the experiments, is provided. Following the experiments, the fracture surfaces are examined using scanning electron microscope, the operation of which is described in the final section.

4.1 1D test setup

Fig. 4.1 shows the experimental setup for uniaxial tests. The uniaxial tests are carried out in a uniaxial test machine type inspekt table 501 (produced by Hegewald&Peschke, Nossen, Germany). The test machine is designed for a maximum load of 50kN. The 1D specimens (tensile, compression and shear specimens), which will be discussed in Chapter 5, are clamped in the both sides (top and bottom) using the clamping jaws as shown in Fig. 4.1. The tests are displacement controlled with the machine velocity of 0.04mm/min. During the experiments, a stereo type setting using four cameras (two on the front and another two on the back side of the specimen) is used to capture the images of the surface of the specimen. Using this setting, the out-of-plane movements can be measured along with the changes in the thickness of the specimen. The captured images are then evaluated using the digital image correlation (DIC) software and one can get a complete information about the three-dimensional displacement fields. A detailed description of DIC system can be found in a later section of this Chapter.

Figure 4.1: Experimental setup for uniaxial tests.

4.2 Biaxial test setup

Shown in Fig. 4.3 is the test setup for the biaxial experiments. The biaxial experiments were performed using the biaxial test machine LFM-BIAX 20kN by Walter and Bai AG, Switzerland. It consists of four electromechanical cylinders, which can be individually controlled. Each cylinder is equipped with an integrated 1720 load cell allowing a load maximum of ±20kN. During the experiments, the specimens are clamped in the four heads of the cylinders and the applied forces $F_{i.j}$ along with the machine displacements $u^{\mathsf{M}}_{i.j}$ are measured, as illustrated in Fig. 4.2. Similar to the 1D tests, the images of the surfaces in the notched region of the specimens are captured during the experiments. Using the DIC software, the surface displacements $u_{i.j}$ in the central area on the symmetry axes of the specimen are evaluated as shown in Fig. 4.3. In the experiments, the ratio between the forces $\zeta = F_2/F_1$ is kept constant, but due to the misalignment of the machine, tolerances in the manufacturing of the specimen and unequal specimen clamping, result in slight deviation in the ratio ζ.

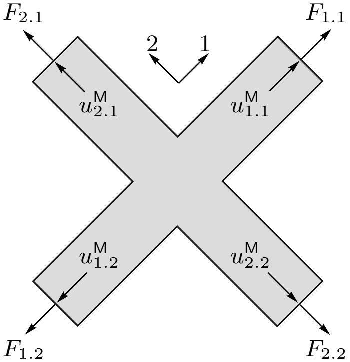

Figure 4.2: Schematic figure of biaxial specimen.

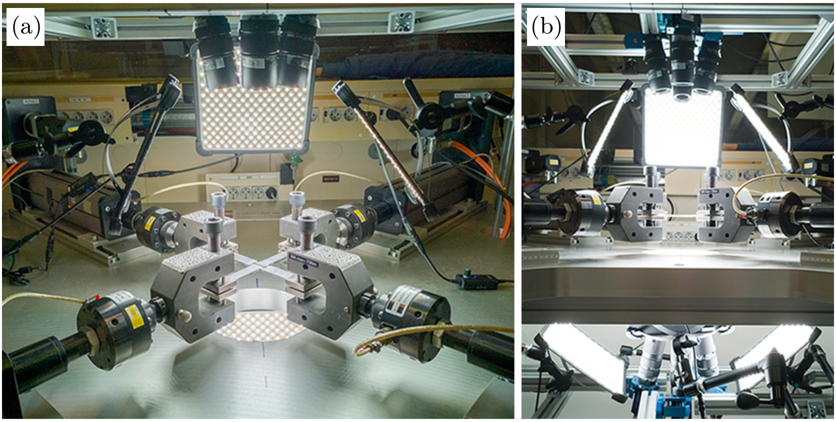

Figure 4.3: (a) Biaxial test machine (b) double sided DIC setup with 8 cameras and lighting system.

This unsymmetry can be avoided by displacement driven processes as described by Gerke et al. [51], which is also used in this work and can be summarized as

- A continuously increasing displacement $u^{\mathsf{M}}_{1.1}$ is applied in cylinder 1.1.

- The same displacement $u^{\mathsf{M}}_{1.1}$ is copied by the cylinder 1.2.
- The resulted force $F_{1.1}$ is multiplied by the load factor and applied to cylinder 2.1 which results in machine displacement $u^{\mathsf{M}}_{2.1}$.
- The resulted machine displacement $u^{\mathsf{M}}_{2.1}$ is copied by the cylinder 2.2.

4.3 Digital image correlation

Digital image correlation is a non-contact optical measurement technique used to measure the surface deformations of an object. The images of an object are taken, stored in digital form and then images are analysed to determine the full-field shape and deformations [105]. The typical hardware required for DIC includes the digital cameras, lenses, proper lighting system and a system with digital image acquisition components to capture the images from the cameras simultaneously. In this work, for the digital image acquisition, Q-400 system from LIMESS Messtechnik und Software GmbH consisting of camera and lenses is used and the captured images are evaluated using Istra4D software provided by Dantec Dynamics GmbH. In the following few important points for DIC are summarized.

Camera and lighting system setup

Six Typ Manta G-609B/C cameras, four above and two below the specimen, each equipped with 75mm lenses are installed to realize stereo-vision arrangement. Furthermore, the distance of the cameras from the specimen should be maintained in such a way that during the experiments, the area of interest of specimen always lies within the depth of field (DOF) and the field of view of the cameras. The lighting system consists of flexible LED lights type Fomex FL-B50 which provides brightness up to 1600 or 800 Lux and are arranged optimally to avoid shadows and reflections around the region of interest of the specimen (ROI).

Calibration

Calibration is a process to determine the imaging or projection parameters required to evaluate the specimen geometry from the images taken from the cameras.

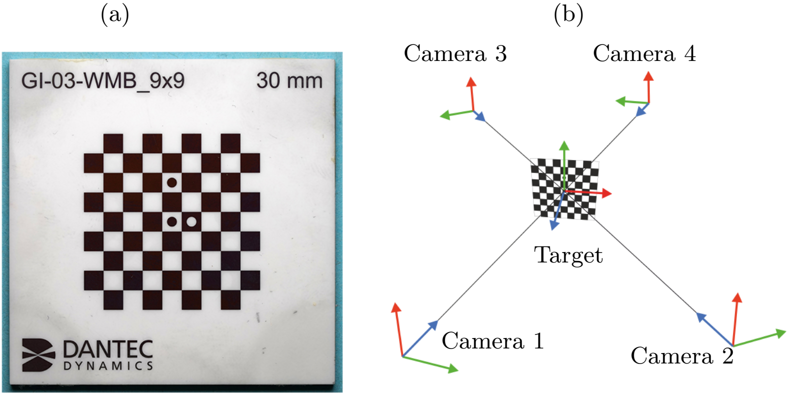

Figure 4.4: (a) Calibration target (b) positioning and coordinate system of the target and the cameras [122].

For this purpose, special calibration target provided by Dantec Dynamics is used, see Fig. 4.4. The calibration target has a checkerboard pattern on the surface with precisely defined grid spacing. To perform calibration, the target should be in the field of view of cameras, has to be within the depth of field and should be positioned at the same distance as the specimen for measurement. It should be tilted in different orientations and the corners of squared patterns are detected by the cameras. Thus, the imaging parameters of each camera (intrinsic parameters) and the relative position of one camera with respect to the other (extrinsic parameters) are determined.

Preparation of test samples, test execution and evaluation

It must be ensured that the surface of the test sample to be examined has different grayscale values as DIC calculates the deformation of the surface by tracking and matching the grayscale values at different times. To achieve this, the specimens are first sprayed with white acrylic lacquer and subsequently black graphite-based coating is sprayed to create a speckle pattern as shown in Fig. 4.5. This creates different grayscale values, which can be detected and evaluated by the evaluation software. The fineness of the speckle pattern depends on the camera system and the size of region of interest, but the diameter of speckle should be approximately 3 to 5 pixels.

Preparation is completed once the speckle pattern and calibration process are done. Then, the images of the ROI are captured by the cameras at a specified time interval. During the test, the ROI must remain within the DOF and changes in the DIC setup or lighting conditions should be avoided. The images of the surfaces are then stored for image analysis. The speckle pattern in ROI are divided into small subsets (facet) and grid spacing is introduced, see for example Fig. 4.5. In this work, the size of a facet is 33 pixels and grid spacing of 11 pixels is used. Then, the software determines the 3D position and the tangential plane of the surface of ROI for every grid points. Moreover, the facet size is determined depending on the size and roughness of the speckle pattern within ROI, but each facet should contain a part of speckle pattern with good contrast features. After that, the grayscale values of each subset in the reference image (undeformed image) are compared with the current image (deformed image). Thus, the entire surface displacement is calculated and can be visualized in the DIC software. Finally, the results from the experiments and corresponding numerical simulations can be compared.

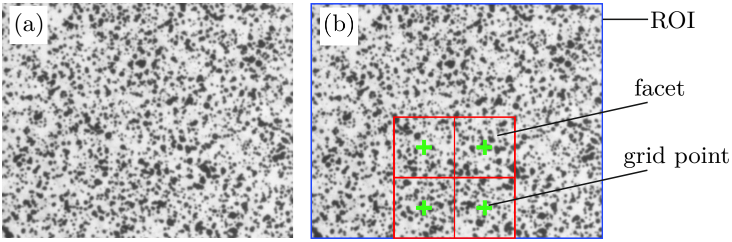

Figure 4.5: (a) Typical speckle pattern (b) example of ROI, facets and grid points.

4.4 Scanning electron microscopy

The scanning electron microscope (SEM) is an instrument which reveals the microstructural information like shape, size, physical and chemical properties of a specimen by creating magnified images [52]. To validate the different damage mechanisms described by the proposed continuum damage model, the images of the fractured surfaces of the specimen are put in the SEM and analyzed in detail. EVO MA 15 model SEM from Carl Zeiss microscopy GmbH is used in this work. Generally, in a scanning electron microscope, beam of electrons are created by electron source and accelerated to high energy. Further, they are modified by electromagnetic coils and lenses and a raster is created, which strike the surface to be analyzed. From the surface of the specimen, secondary electrons with low kinetic energy are ejected and they are spotted by the detectors. The measured signals from the detectors are then processed to a gray value of the pixel corresponding to the raster resulting into a complete image of the analyzed surface. To prevent the electron beam from being deflected by molecules and atoms from the atmospheric gases, which would significantly degrade image quality, the entire process takes place in a high vacuum.

5 Test specimens and identification of the material parameters

Using the experimental techniques presented in Chapter 4, the required material parameters are determined. The elastic and anisotropic plastic parameters for the investigated aluminum alloy are calibrated using uniaxially loaded specimens while the damage mode parameters are determined using both uniaxially and biaxially loaded specimens. Short overview of the material used and specimen is given. The process to determine the material parameters is discussed in detail.

5.1 Aluminum alloy EN AW-2017A

The material under investigation is the aluminum alloy EN AW-2017A (also known as EN AW-AlCu4MgSi), which is provided in the form of 4mm thick sheets. Mostly used in aerospace and automotive industries, EN AW-2017A has high strength, ductility and formability. The chemical composition of EN AW-2017A is shown in Table. 5.1. The microstructural examinations done by [81] revealed that due to the extrusion process, the aluminum alloy is anisotropic in nature. Similarly, anisotropic mechanical behavior of 2017 aluminum alloy was also reported in [62, 99]. Therefore, in this work, anisotropic behavior of EN AW-2017A is studied in detail.

Table 5.1: Chemical composition of EN AW-2017A (% weight)

Material	Cu	Fe	Mn	Mg	Si	Zn	Cr	Others	Al
EN AW-2017A	4.0	0.7	0.7	0.7	0.5	0.25	0.10	0.15	to balance

5.2 Test specimens

5.2.1 Uniaxially loaded specimens

For the determination of elastic and plastic anisotropic parameters, three types of test specimens are used. Fig. 5.1(a) shows an adapted flat dog-bone-shaped tension-compression specimen (TC-specimen), which is 101.0mm long with a square cross sectional area of 16.0mm^2. The central part of the TC-specimen is shortened to prevent the early occurrence of buckling during the compression tests. The TC-specimens are cut from 4mm thick aluminum sheets.

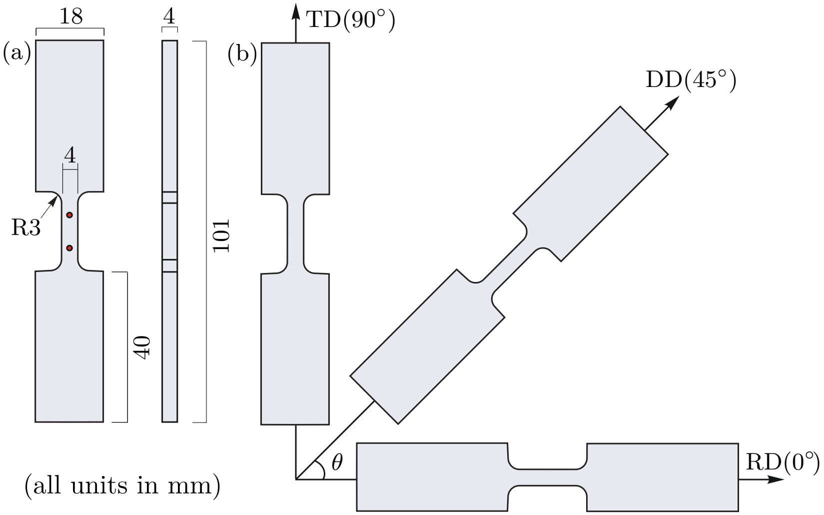

Figure 5.1: (a) TC-specimen and (b) different directions with respect to the rolling direction (RD).

Brünig et al. [32] performed tensile tests on specimens cut in various directions: 0°, 15°, 30°, 45°, 65°, 75° and 90° with respect to the rolling direction (RD) and determined the yield stresses as well as the Lankford coefficients. Furthermore, utilizing the results from the experiments including 0°, 45° and 90° and a anisotropic yield criterion [57], the experimental yield stresses and the Lankford coefficients were accurately predicted. Therefore, in this work, the TC-specimens cut in rolling direction (RD), diagonal direction (DD) and transverse direction (TD) with respect to the rolling direction (Fig. 5.1 (b)) are used to examine the anisotropy of the aluminum alloy. To determine Lankord coefficients, which will be further elaborated upon in the following subsection, TC-specimens are deemed unsuitable due to their non-compliance with established standards [46]. Consequently, conventional tensile specimens in the shape of a dog bone are used instead of TD-specimen (see Fig. (5.2)). Additionally, tensile specimens are also cut in RD, DD and TD, similar to TC-specimen to examine the plastic anisotropic behavior.

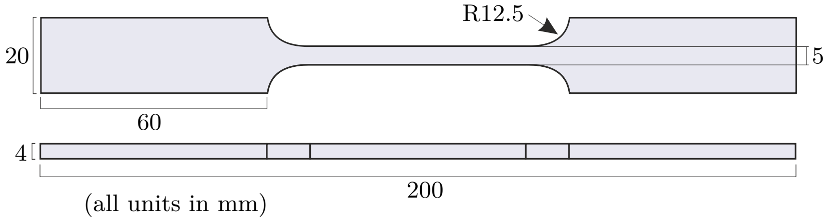

Figure 5.2: Tensile specimen.

Similarly, shear tests are carried out using the newly developed shear specimen, see Fig. 5.3(a). It is characterized by two parallel notches, which are arranged in central region of the specimen. As depicted in Fig. 5.3(b), each of the notches is 6.0mm long with cross section area of 12.0mm^2. Strains are localized in the notches during plastic deformation and nearly pure shear stress state is obtained in the cross section of the notches. Furthermore, shear specimens are also prepared in three distinct rolling directions, similar to TC-specimens, to assess the material's plastic anisotropic behavior.

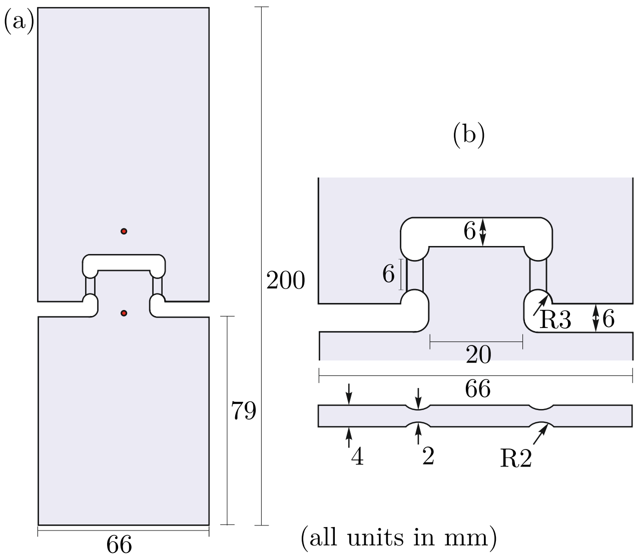

(all units in mm)

Figure 5.3: (a) Shear specimen (b) Central part of the shear specimen.

5.2.2 Biaxially loaded specimens

Uniaxial tests are not sufficient to determine the damage parameters and to study the damage behavior, which are strongly stress-state dependent. Special kind of test specimens are required to study the damage and fracture behavior under wide range of stress-states. In this context, Brünig et al. [27, 28] developed a new biaxially loaded specimens and studied the damage behavior of ductile metals in a broad range of stress triaxialites. But, the rotation of the central part and the coupling of arms of specimen resulting in transverse forces in the machine didn't make the specimen of first choice. Therefore, to solve this problem, Gerke et al. [51] developed two new biaxially loaded specimens, namely, X0- and H-specimen.
The outer dimensions of the H-specimen geometry is shown in Fig. 5.4(a). The H-specimen is triple symmetric and characterized by four notches arranged parallely in the central region, see Fig. 5.4(b). The strains are localized in these notches, where the final fracture also occurs, thus, making it possible to study different stress-state dependent damage mecha-

nisms leading to the final fracture. Loading only in vertical axis (axis 1) results in shear stress- state in all four notches, while tensile or compressive stress-state is obtained if the specimen is only loaded in horizontal axis (axis 2). Apart from the shear, tensile and compressive stress-states, it is possible to generate a wide range of stress-states in the notches by applying different loading combinations in axis 1 and axis 2. Furthermore, to study the effect of loading direction on the onset and evolution of damage in anisotropic ductile metals, the H-specimens are cut out from 4mm thick aluminum sheet in RD, DD and TD as shown in Fig. 5.4(a). The X0-specimen is the second specimen for investigating biaxial load cases, which also has four notched regions where local failure can occur. The outer dimensions of X0-specimen geometry is shown in Fig. 5.5(a), which is 240mm x 240mm. The notches are arranged at 45° angle to the axes with each of the notches measuring 6.0mm long. The holes in the center of the specimen, see Fig. 5.5(b), result in only two arms of the specimen connected at a time by a small double-sided notched area. The notches in the thickness direction, as shown in Fig. 5.5(c), have a radius of 2mm and reduce the central notched area to a thickness of 2mm. The cross section area of each of the notches is 12.0mm^2. If the same tensile load is applied to the both axes at the same time, tension dominated stress state with high hydrostatic stresses occurs in the notches. Similarly, shear dominated stress-state occurs when at the same time, tensile load is applied in one of the axes and a compressive load in applied on the other axes. Thus, by different loading combinations a broad spectrum of stress-state can be generated in the notches. Similar to the H-specimens, X0-specimens are also cut in RD, DD and TD to analyze the effect of anisotropic material characteristics on the damage behavior of the aluminum alloy sheets.

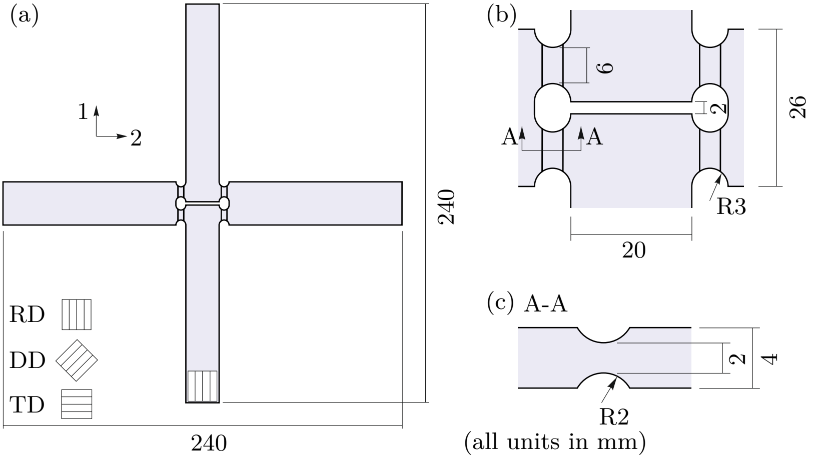

Figure 5.4: H-specimen geometry.

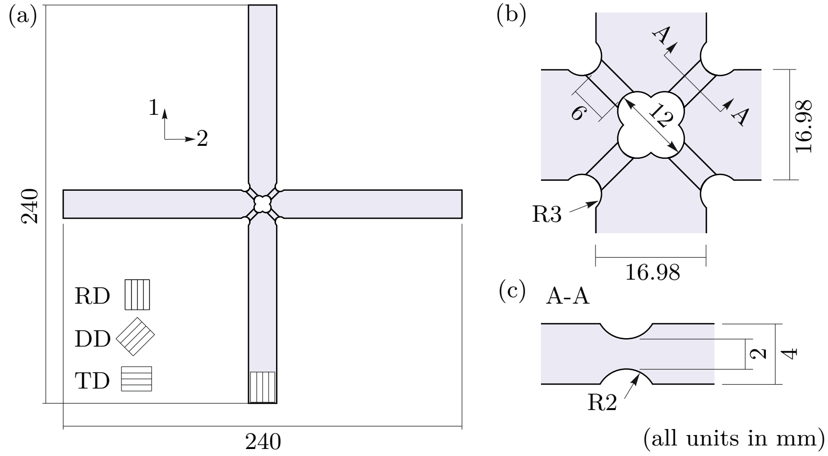

Figure 5.5: X0-specimen geometry.

5.2.3 Notation and evaluation points

Fig. 5.6(a) and Fig. 5.6(b) illustrate the used notations and the evaluation points for H-and X0-specimen, respectively. These are necessary to analyze the force-displacement diagrams in different directions. The first index indicates the axis and the second index indicates the direction in which either the force or the displacement is acting, respectively. For example, the force $F_{1.2}$ is acting on the specimen parallel to the axis 1 but in opposite direction, whereas $F_{1.1}$ is acting on the specimen in positive direction parallel to the axis 1. This notation also applies for the machine displacements $u^{\mathsf{M}}_{i.j}$ and for the surface displacements $u_{i.j}$. The surface displacements are evaluated with the help of ISTRA4D software for the red points as depicted in Fig. 5.6. For each axes, the relative displacement between the two points is given by $\varDelta u_i = u_{i.1} + u_{i.2}$. The forces acting on the specimen $F_{i.j}$ and the machine displacements $u^{\mathsf{M}}_{i.j}$ are passed to the DIC system from the biaxial testing machine.

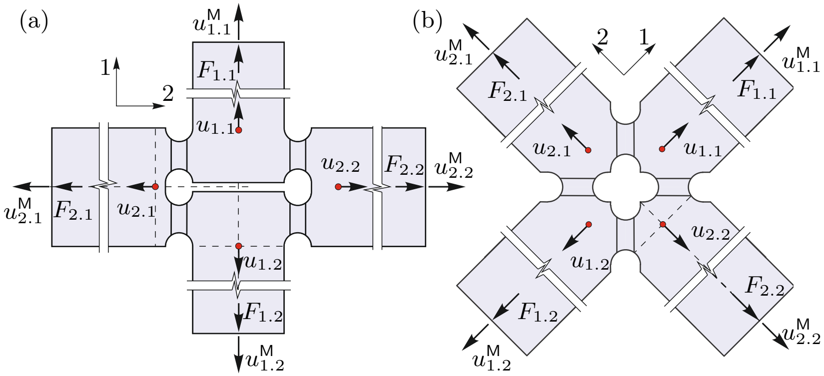

Figure 5.6: Notation and evaluation points for (a) H-specimen and (b) X0-specimen .

5.3 Material parameters identification

In the first part of this section, identification of the elastic and anisotropic plastic parameters is discussed. They are directly determined from the experimental results obtained from the uniaxially loaded specimens. With the elastic and anisotropic plastic material parameters in hand, numerical simulations using the Hoffman yield criterion (Eq. (2.43)) are carried out and the corresponding load-displacement curves are compared with the experimental results from the uni- and biaxially loaded specimens to develop the damage mode parameters in Eq. (2.60). Additionally, the approach to calibrate the stress-state dependent parameters in Eq. (2.62) is also discussed in detail.

5.3.1 Elastic and plastic anisotropic parameters

Using the TC-specimens, uniaxial tensile tests are carried out three times each for RD, DD and TD. The obtained load-displacement diagrams are depicted in Fig. 5.7, which show that the experiments are quite repeatable only with marginal differences.

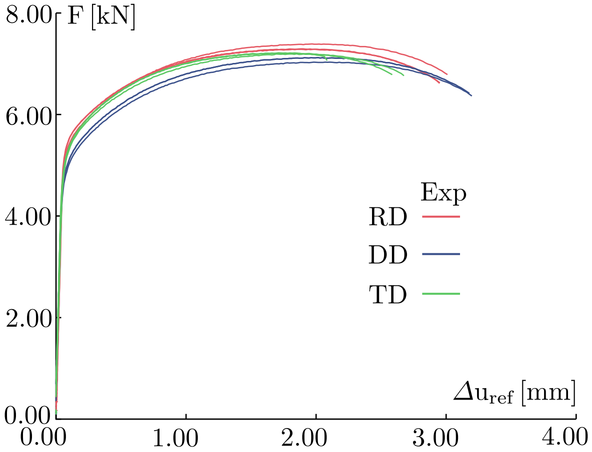

Figure 5.7: Load-displacement curves obtained from uniaxial tensile tests.

But, the curves between the rolling directions show obvious inconsistency. The curve for the specimen loaded in RD with respect to rolling direction is higher than the specimen loaded in DD and TD and this trend is maintained till the final fracture of the specimen. The displacement at the final failure is largest for loading in DD and the smallest for loading in TD.

The load-displacement diagram is converted to the equivalent stress-strain curves for both tension and compression tests and are shown in Fig. 5.8(a). Note that the tests are performed three times each for three different directions and only the representative curves are plotted in Fig. 5.8(a). In the elastic region, there are no differences in stress-strain response between loading in RD, DD and TD. Therefore, the material parameters for isotropic elastic behavior are determined where Young's modulus E = 74,000MPa and Poisson's ratio $\nu = 0.3$.

It is observed that the initial yield stresses under compression are smaller than under tension which is the SD effect as discussed in Chapter 2. The same kind of behavior was also reported in the recent experiments done by Wei et al. [116] for the aluminum alloy. Furthermore, there are no apparent differences in the initial yield stresses between RD, DD and TD under compression. But, for the tension tests, the initial yield stresses are different for RD, DD and TD as shown in Fig. 5.8(b). The plastic strain hardening behavior is fitted using the Voce law [114] for the respective current yield stresses

$$c = c_0 + R_0\gamma + R_\infty \left(1 - e^{-b\,\gamma}\right) \tag{5.1}$$

where c_0 is the initial yield stress, R_0 and R_∞ the hardening moduli, b is the hardening exponent and the equivalent plastic strain γ. A good quality of fitting is achieved (see Fig. 5.8(b)) and the parameters for loading in RD, DD and TD are given in Table. 5.2.

There are different methods for the determination of the anisotropic material parameters in Eq. (2.43) as summarized in Aretz [6]. One of the method is to use only the yield stresses from the uniaxial tensile and shear tests in RD, DD and TD. Another possible method is to use only the Lankford coefficients (r-value), which will be described in detail in the following section. One can also use the combined method using both the yield stresses and r-values to determine the anisotropic material parameters as shown recently by Brünig et al. [32].

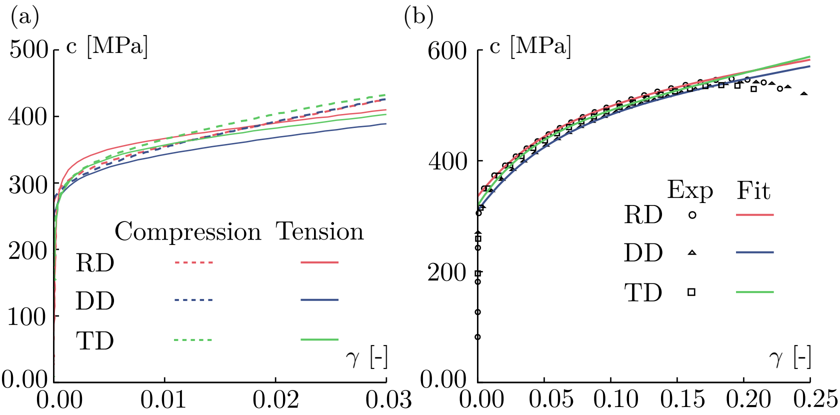

Figure 5.8: (a) Uniaxial equivalent stress-strain curve for tension and compression tests and (b) fitting of the equivalent stress-strain curve for tension tests after loading in RD, DD and TD.

Table 5.2: Plastic material parameters

	c_0 [MPa]	R_0 [MPa]	R_∞ [MPa]	b [-]
RD	313	464	147	20
DD	297	474	127	28
TD	308	445	128	25

The Lankford coefficient [73], also known as r-value, is the ratio of plastic strains in width direction to the thickness direction. Considering that the plastic volume remains constant during the plastic deformation, r-value is given as

$$r_\theta = \frac{\dot{\bar{H}}^{\mathsf{pl}}_{\theta+90^\circ}}{\dot{\bar{H}}^{\mathsf{pl}}_{z}} = \frac{-\dot{\bar{H}}^{\mathsf{pl}}_{\theta+90^\circ}}{\dot{\bar{H}}^{\mathsf{pl}}_{x} + \dot{\bar{H}}^{\mathsf{pl}}_{y}} \tag{5.2}$$

where $\dot{\bar{H}}^{\mathsf{pl}}_{x}$, $\dot{\bar{H}}^{\mathsf{pl}}_{y}$ and $\dot{\bar{H}}^{\mathsf{pl}}_{z}$ are the plastic strain rates in longitudinal, width and thickness directions, respectively. The standardized approach for calculating the r-value is found in [46]. Furthermore, following the established norm [46], the TC-specimen is not suitable for the determination of r-value. Consequently, experiments are carried out using the tensile specimens, illustrated in Fig. 5.2. The strains on the surface of the specimen loaded uniaxially in RD, DD and TD are measured and the evolution of r-values are plotted in Fig. 5.9. Then, they are fitted in the region between 5% to 20% of the equivalent plastic strain. Another possible way of fitting r-value is by using the linear equation as in [79], where r-values are continuously evolving during the loading process. As can be seen in Fig. 5.9, the fitted r-values agree well with the experi-

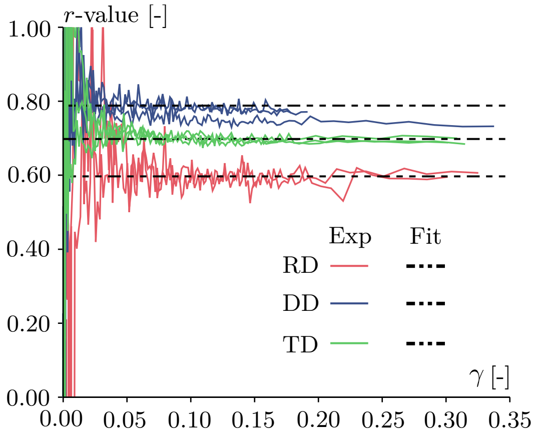

Figure 5.9: Evolution of r-value.

mental results within the specified range of the equivalent plastic strain. Hence, a constant r-value is taken for each RD, DD and TD and the identified values are given in Table. 5.3.

Table 5.3: Lankford coefficients

r_0 [-]	r_{45} [-]	r_{90} [-]
0.597	0.783	0.695

Based on the yield stresses and the r-values obtained from the experiments, the anisotropic material parameters are calibrated. Identification of anisotropic material parameters for thin metal sheets is constrained to experiments involving flat specimens cut within the plane of the sheets. In this context, plane stress conditions are considered, assuming that stresses in the z-direction are marginal. The plastic strain rate (Eq. (2.51)) in x-direction can be expressed as

$$\dot{\bar{H}}_x^{\mathsf{pl}} = \dot{\bar{\lambda}} \left[\left(C_4 + C_5 \right) \bar{T}_x - C_4 \bar{T}_y \right] \tag{5.3}$$

where

$$\dot{\bar{\lambda}} = \dot{\lambda} \frac{1}{2\sqrt{\bar{J}_2^{\mathsf{H}}}}. \tag{5.4}$$

Similarly, the plastic strain rates in other directions are

$$\dot{\bar{H}}_y^{\mathsf{pl}} = \dot{\bar{\lambda}} \left[\left(C_4 + C_6 \right) \bar{T}_y - C_4 \bar{T}_x \right], \tag{5.5}$$

$$\dot{\bar{H}}_{xy}^{\mathsf{pl}} = \dot{\bar{\lambda}} \, C_7 \bar{T}_{xy}, \tag{5.6}$$

and

$$\dot{\bar{H}}_z^{\mathsf{pl}} = - \left(\dot{\bar{H}}_x^{\mathsf{pl}} + \dot{\bar{H}}_y^{\mathsf{pl}} \right) = - \dot{\bar{\lambda}} \left(C_5 \bar{T}_x + C_6 \bar{T}_y \right). \tag{5.7}$$

For uniaxial tension tests conducted with specimens cut at an angle θ to the rolling direction of the thin sheet, the components of the stress tensor can be determined as

$$\bar{T}_x = \bar{T}_\theta \cos^2\theta,\ \bar{T}_y = \bar{T}_\theta \sin^2\theta \text{ and } \bar{T}_{xy} = \bar{T}_\theta \sin\theta\cos\theta. \tag{5.8}$$

Furthermore, transforming the plastic strain rates to the orientation θ of the specimen and its corresponding transverse direction ($\theta + 90°$) results in the following

$$\dot{\bar{H}}^{\mathsf{pl}}_\theta = \dot{\bar{H}}^{\mathsf{pl}}_x \cos^2\theta + \dot{\bar{H}}^{\mathsf{pl}}_y \sin^2\theta + 2\dot{\bar{H}}^{\mathsf{pl}}_{xy} \sin\theta\cos\theta. \tag{5.9}$$

$$\dot{\bar{H}}^{\mathsf{pl}}_{\theta+90^\circ} = \dot{\bar{H}}^{\mathsf{pl}}_y \cos^2\theta + \dot{\bar{H}}^{\mathsf{pl}}_x \sin^2\theta - 2\dot{\bar{H}}^{\mathsf{pl}}_{xy} \sin\theta\cos\theta. \tag{5.10}$$

Making use of the Eqs. (5.3), (5.5), (5.6), (5.10) and (5.2), the equation to calculate the r-value can be further expressed as

$$r_\theta = \frac{C_4 + \left(2C_7 - 4C_4 - C_5 - C_6 \cos^2\theta\sin^2\theta\right)}{C_5\cos^2\theta + C_6\sin^2\theta} \tag{5.11}$$

which facilitates the calculation of the anisotropic material parameters appearing in the Hoffman yield criterion (Eq. (2.43)). Moreover, r-value for RD, DD and TD are determined as

$$r_{0^\circ} = \frac{C_4}{C_5},\ r_{45^\circ} = \frac{C_7}{C_5 + C_6} - \frac{1}{2} \text{ and } r_{90^\circ} = \frac{C_4}{C_6}. \tag{5.12}$$

Considering the Hoffman yield criterion (Eq. (2.43)) for the tensile test in rolling direction (RD), the yield criterion can be written as

$$f^{\mathsf{pl}}_{tx} = C_1\bar{T}_{tx} + \sqrt{\frac{1}{2}(C_4 + C_5)}\bar{T}_{tx} - c_0 = 0. \tag{5.13}$$

Furthermore, $\bar{T}_{tx} = c_0$ is the initial yield stress determined from the tensile test conducted in RD (x-direction), which is taken as a reference experiment. Similarly, making use of the Eq. (2.43) for the compression test in the rolling direction

$$f^{\mathsf{pl}}_{cx} = -C_1 \bar{T}_{cx} + \sqrt{\frac{1}{2}(C_4 + C_5)\bar{T}_{cx}} - c_0 = 0 \tag{5.14}$$

where $\bar{T}_{cx}$ is the initial yield stress in compression determined from the compression test done in RD. Making use of Eq. (5.13) and Eq. (5.14), the anisotropic material parameter C_1 can be calculated as

$$C_1 = \frac{1}{2}\left(1 - \frac{\bar{T}_{tx}}{\bar{T}_{cx}}\right). \tag{5.15}$$

In addition, utilizing the yield stresses from the tension and compression tests $\bar{T}_{ty}$ and $\bar{T}_{cy}$, respectively, conducted in TD (y-direction), the coefficient C_2 can be determined as

$$C_2 = \frac{1}{2}\bar{T}_{tx}\left(\frac{1}{\bar{T}_{ty}} - \frac{1}{\bar{T}_{cy}}\right). \tag{5.16}$$

Moreover, using both the r-values (Eq. (5.12)) and the initial yield stresses in tension and compression determined from the experiments, from Eqs. (5.13) and (5.14) the remaining anisotropic material parameters appearing in the Hoffman yield criterion can be calculated as follows

$$C_5 = \frac{1}{2\,(1 + r_0)}\left(1 + \frac{\bar{T}_{tx}}{\bar{T}_{cx}}\right)^2, \tag{5.17}$$

$$C_4 = \frac{1}{2}\left(1 + \frac{\bar{T}_{tx}}{\bar{T}_{cx}}\right)^2 - C_5, \tag{5.18}$$

$$C_6 = \frac{C_4}{r_{90}} \quad \text{or} \quad C_6 = \frac{1}{2}\bar{T}^2_{tx}\left(\frac{1}{\bar{T}_{ty}} + \frac{1}{\bar{T}_{cy}}\right)^2 - C_4, \tag{5.19}$$

Table 5.4: Anisotropic material parameters

C_1	C_2	C_3	C_4	C_5	C_6	C_7	C_8	C_9
-0.042	-0.010	0.0	0.812	1.360	1.310	3.758	3.0	3.0

and

$$C_7 = \left(r_{45} + \frac{1}{2} \right) (C_5 + C_6) \,. \tag{5.20}$$

Alternatively, C_7 can be identified by using the initial yield stress from shear tests (S_{xy}) using the shear specimen shown in Fig. 5.3 as

$$C_7 = \left(\frac{\bar{T}_{tx}}{\bar{S}_{xy}} \right)^2 \,. \tag{5.21}$$

Furthermore, in the presence of additional normal stresses $\bar{T}_{tx}$ in the critical region of the specimen, C_7 can be identified as

$$C_7 = \frac{1}{\bar{S}_{xy}^2} \left[\left(\bar{T}_{tx} - C_1 \bar{T}_{tx} \right)^2 - \frac{1}{2} (C_4 + C_5) \bar{T}_{tx}^2 \right] . \tag{5.22}$$

In the present work, C_6 is taken as mean value from Eq. (5.19) and also C_7 as the mean value from Eq. (5.20) and Eq. (5.22). The calibrated plastic anisotropic material parameters are listed in Table. 5.4.

6 Numerical aspects

After having all the required elastic and plastic anisotropic parameters, numerical simulations using the elastic-plastic material model discussed above are carried out to analyze the stress-states at the onset of damage. The specimens given in Fig. 5.1, Fig. 5.3, Fig. 5.4 and Fig. 5.5 are discretized to prepare a finite element model. Especially, taking the advantage of the symmetry, only a quarter of the sample is modeled and symmetrical boundary conditions are used. Fig. 6.1 shows the finite element meshes of X0- and H-specimen, where the X0- and H-specimen are divided into 18,645 and 20,802 eight-noded elements, respectively. Element type Solid185 defined by eight nodes and the orthotropic material properties with $\bar{B}$ [100, 121] method is used. Meshes in the notched areas, where the stresses and strains are expected to localize, are refined as depicted in Fig. 6.1. The size of the mesh influences the computational time and accuracy of the FE analysis, therefore, mesh convergence investigations were carried out to determine the optimum mesh density in the notched areas. Comparing the global and local results from the FE-simulation and DIC, the notch was discritized into 28/24/18 number of elements in 1/2/3 direction (see the coordinate system in Fig. 5.6). Thus, the length of a hexahedron element in the notched area is about 0.1mm. The sample is discritized with coarser meshes other than the notched area, to reduce the computational effort as shown in Fig. 6.1.

In order to achieve the desired constant load ratio as in the experiments, in the numerical simulations, multiframe restart is implemented. Multiframe restart [5] allows to preserve analysis data at multiple substeps throughout a simulation run and subsequently resume the run from any of those saved substeps. The applied displacement ratio at the specimen arms along both axes results to the corresponding force ratio. The resulted force ratio is then compared to the desired load ratio. In cases where the deviation between the achieved force ratio and the desired value exceeds the predefined limit, the ongoing load step is restarted. The converged result from the previous iteration serves as the initial

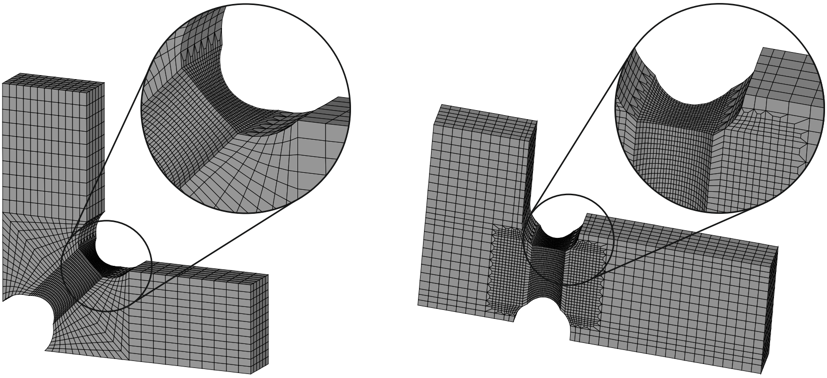

Figure 6.1: Finite element meshes of (a) the X0- and (b) the H-specimen.

value for the current displacement ratio, minimizing the computational cost. The convergence criteria for the global Newton-Raphson method is set as default Ansys value of 0.5%.

Because the specimen features four notched regions, the numerical results obtained from simulating an ideal quarter of the specimen inherently differ from the outcomes of real experiments and are not directly comparable. In the experimental setting, we observe that notches with the most significant material or geometric imperfections exhibit stronger and earlier localization, while the remaining notches experience less pronounced localization. The numerical simulation lacks the ability to reproduce this asymmetric effect. To enable more meaningful comparisons between the numerical simulations and experiments, an experimental mean value is established as a reference. This involves averaging the maximum values of the first principal strain obtained from DIC for all four notches within a given experiment, and subsequently, averaging these values across all experiments conducted with the same experimental procedure. As a result, this mean value of localization represents a scenario where all four notches simultaneously experience localization to the same extent. Hence, this mean value is suitable for comparison with the numerical results.

6.1 Identification of the damage mode parameters

The determination of stress-state dependent damage mode parameters in Eq. (2.60) is based on the identification procedure proposed by Brünig et al. [29], which is a hybrid experimental-numerical approach. The load-displacement curves from the experiments and numerical simulations based on elastic-plastic material model are compared and the damage is assumed to begin when the numerically predicted curves start to deviate from the experimental ones. Most probably, the onset of the damage takes place at the critical location, the location where the elements have the highest equivalent plastic strains. Various fracture models have also been developed [10, 91, 107], where it is considered that the fracture initiates at the critical element. Using the above mentioned approach, the generalized Hoffman stress invariants $\bar{I}_1^{\mathsf{H}}$, $\bar{J}_2^{\mathsf{H}}$ and $\bar{J}_3^{\mathsf{H}}$, the generalized stress triaxiality $\bar{\eta}^{\mathsf{H}}$ and the generalized Lode parameter $\bar{L}^{\mathsf{H}}$ are achieved at the critical element.

The experimental load-displacement curves from the uniaxial tensile tests for RD, DD and TD are compared with the numerical ones, see Fig. 6.2(a). The RD loading exhibits the highest loads, while comparatively smaller loads are evident for DD loading, with differences of approximately 7%.

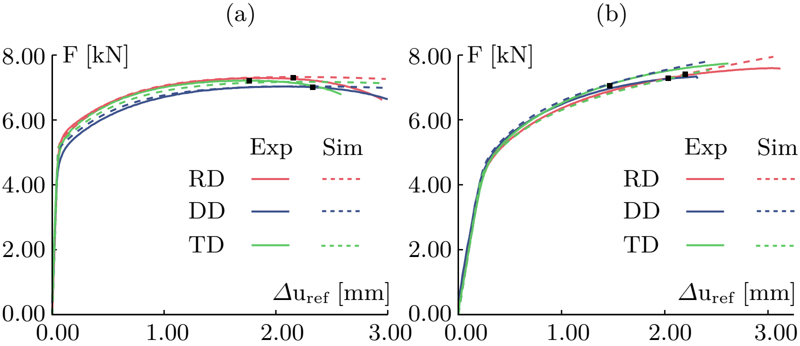

Figure 6.2: Experimental (Exp) and numerical simulations (Sim) force-displacement curves for (a) uniaxial tensile tests and (b) shear tests.

The curves agree well up to the certain value of the displacement and then start to deviate. The damage process is assumed to begin when the numerical results start to deviate from the experimental ones, which is characterized by the black colored points as shown in Fig. 6.2(a). Then, at this point, the stress state at the critical location of the specimen is analyzed in detail. The generalized Hoffman stress invariants $\bar{I}_1^{\mathsf{H}}$, $\bar{J}_2^{\mathsf{H}}$ and $\bar{J}_3^{\mathsf{H}}$, the generalized stress triaxiality $\bar{\eta}^{\mathsf{H}}$ and the generalized Lode parameter $\bar{L}^{\mathsf{H}}$ are obtained and are listed in Tab. 6.1 for loading in RD, in Tab. 6.2 for loading in DD and in Tab. 6.3 for loading in TD. Similarly, the results from the shear tests are given in Fig. 6.2(b). The load-displacement curves from numerical simulations and experiments are similar till the specific value of load but tend to veer away after further loading, which again indicate the initiation of the damage and are marked by the black points in Fig. 6.2(b). The strains and stresses localize in the notches and the stress-state is studied in detail as the generalized stress parameters are given in Tabs. 6.1, 6.2 and 6.3.
Furthermore, Fig. 6.3 illustrates the load-displacement curves of the X0-specimen subjected to biaxial loading, showcasing both experimental and numerically predicted results. The experiments are carried out for RD, DD and TD with different loading ratios (a) $\mathrm{F}_1/\mathrm{F}_2 = 1/0$, (b) $\mathrm{F}_1/\mathrm{F}_2 = 1/1$ and (c) $\mathrm{F}_1/\mathrm{F}_2 = 1/-1$ producing different stress-states in critical regions. As can be noted in Fig. 6.3, the experimental and numerical curves agree well and the discrepancies between them are marked by black points where the stress-states are analyzed. The obtained stress parameters in the critical region are listed in Tabs. 6.1, 6.2 and 6.3 for RD, DD and TD, respectively.

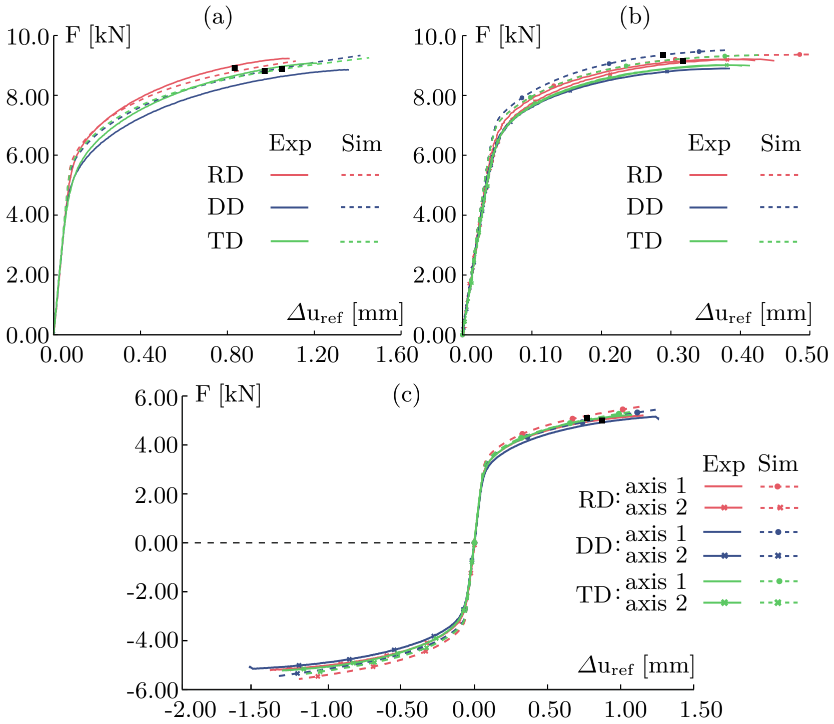

Figure 6.3: Experimental and numerical load-displacement curves using X0-specimen for the load ratio (a) $F_1/F_2 = 1/0$, (b) $F_1/F_2 = 1/1$ and (c) $F_1/F_2 = 1/-1$.

In addition, Fig. 6.4 presents both experimental and numerically predicted load-displacement curves for the biaxially loaded H-specimen in different rolling directions. The curves depict various load ratios:(a) $F_1/F_2 = 0/1$, (b) $F_1/F_2 = 1/0$, (c) $F_1/F_2 = 1/0.5$, (d) $F_1/F_2 = 1/1$ and (e) $F_1/F_2 = 1/-2$. Once again, the experimental and numerical curves exhibit good agreement until the black points, beyond which they begin to deviate from each other. Initiation of damage is assumed to occur at the steps marked by the black points.

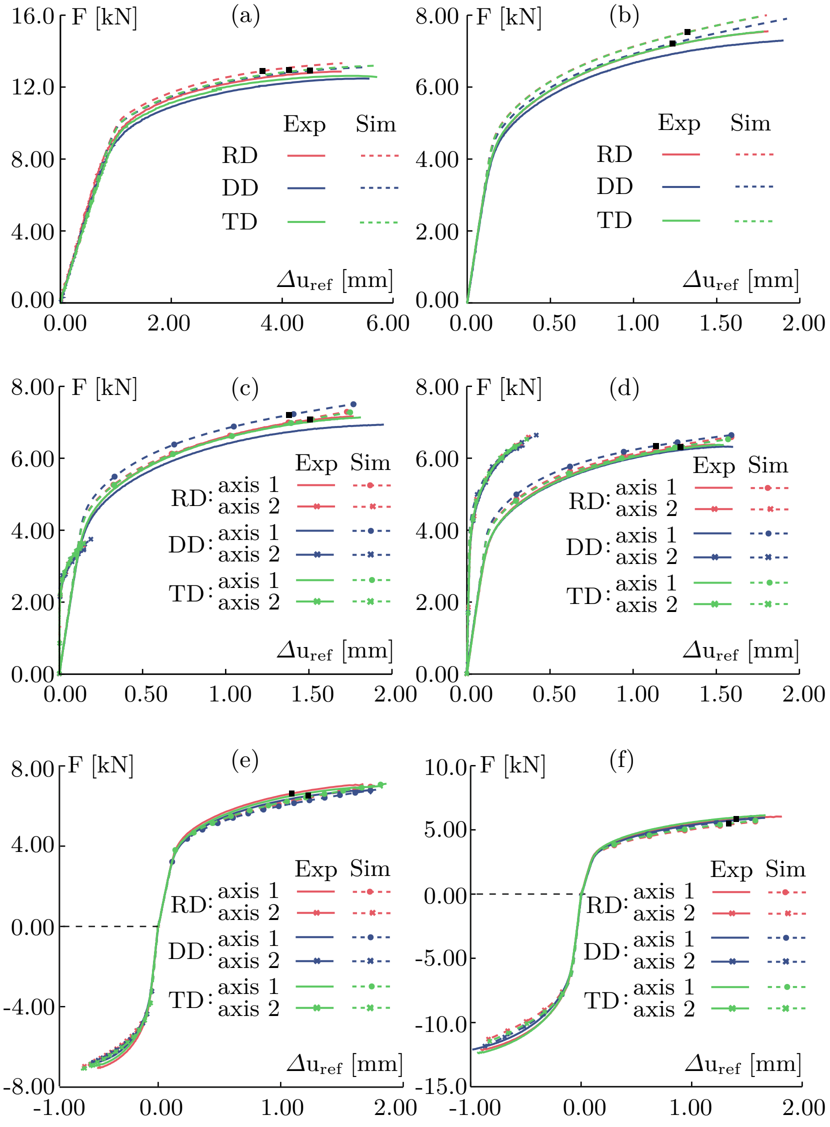

Figure 6.4: Experimental and numerical load-displacement curves using H-specimen for the load ratio (a) $F_1/F_2 = 0/1$, (b) $F_1/F_2 = 1/0$, (c) $F_1/F_2 = 1/0.5$, (d) $F_1/F_2 = 1/1$, (e) $F_1/F_2 = 1/-1$ and (f) $F_1/F_2 = 1/-2$.

Respective stress parameters are determined at these specific loading stages in the critical regions of the H-specimens and are shown in Tabs. 6.1, 6.2 and 6.3 for RD, DD and TD, respectively.

Table 6.1: Generalized stress parameters for RD

Tests	I_1^{H} [MPa]	$\sqrt{J_2^{\mathsf{H}}}$ [MPa]	J_3^{H} [MPa^3]	η^{H} [-]	L^{H} [-]
Tensile	1100	557	4.82E+07	0.38	-0.72
Shear	260	528	1.05E+07	0.09	-0.18
H 0/1	1480	456	9.60E+06	0.62	-0.26
H 1/0	88	521	4.35E+06	0.03	-0.08
H 1/0.5	521	541	2.11E+07	0.18	-0.34
H 1/1	890	551	3.61E+07	0.311	-0.56
H 1/-1	-579	523	-2.16E+07	-0.21	0.39
H 1/-2	-1001	547	-3.73E+07	-0.35	-0.59
X0 1/0	725	481	2.65E+07	0.29	-0.61
X0 1/1	1132	514	6.40E+06	0.43	-0.12
X0 1/-1	332	493	5.77E+06	0.13	-0.13

The outcomes of numerical simulations from the experiments involving uniaxially and biaxially loaded specimens provide ample data (refer to Tabs. 6.1 - 6.3) to support the establishment of a quantitative framework for the stress-state dependent damage mode parameters α and β featured in the damage criterion Eq. (2.60). This criterion is articulated in the context of stress and loading direction space. Specifically, within the domain of negative or nearly zero stress triaxialities, damage primarily emerges due to the formation and evolution of micro-shear cracks. These cracks are evident as a consequence of shear stresses being dominant. Therefore, the parameter α is assumed to be 0 and the parameter β is equal to 1. Looking at the uniaxial tensile tests (Fig. 5.8), the damage is assumed to initiate at $\sigma = 480$MPa. The parameter α is selected as the value for isotropic plastic behavior determined through the micro-scale numerical simulations [30], which is same and valid for all the loading

Table 6.2: Generalized stress parameters for DD

Tests	I_1^{H} [MPa]	$\sqrt{J_2^{\mathsf{H}}}$ [MPa]	J_3^{H} [MPa^3]	η^{H} [-]	L^{H} [-]
Tensile	755	538	5.05E+07	0.27	-0.84
Shear	667	588	2.05E+07	0.21	-0.26
H 0/1	1322	466	8.60E+06	0.54	-0.21
H 1/0	376	523	6.34E+06	0.13	-0.11
H 1/0.5	698	561	2.70E+07	0.24	-0.39
H 1/1	956	575	4.33E+07	0.32	-0.59
H 1/-1	-143	531	-1.87E+07	-0.05	0.32
H 1/-2	-532	537	-3.31E+07	-0.19	0.55
X0 1/0	414	483	2.42E+07	0.16	-0.55
X0 1/1	1270	500	7.26E+06	0.48	-0.15
X0 1/-1	345	482	2.59E+06	0.13	-0.06

Table 6.3: Generalized stress parameters for TD

Tests	I_1^{H} [MPa]	$\sqrt{J_2^{\mathsf{H}}}$ [MPa]	J_3^{H} [MPa^3]	η^{H} [-]	L^{H} [-]
Tensile	458	500	3.14E+07	0.18	-0.65
Shear	138	518	8.80E+06	0.05	-0.16
H 0/1	1134	453	7.78E+06	0.48	-0.21
H 1/0	11	522	3.31E+06	0.04	-0.06
H 1/0.5	255	542	1.84E+07	0.09	-0.30
H 1/1	461	516	2.53E+07	0.17	-0.47
H 1/-1	-432	527	-2.03E+07	-0.15	0.36
H 1/-2	-753	547	-3.50E+07	-0.26	0.55
X0 1/0	224	474	2.22E+07	0.09	-0.54
X0 1/1	1106	501	6.35E+06	0.42	-0.12
X0 1/-1	270	468	1.04E+06	0.11	0.02

directions.

$$\alpha\left(\eta^{\mathsf{H}}\right)=\begin{cases}0 \;\text{ for }\; \eta^{\mathsf{H}}\leq 0\\[1ex] \frac{1}{3} \;\text{ for }\; \eta^{\mathsf{H}}>0\end{cases}. \tag{6.1}$$

Examining the stress parameters across all experiments involving specimens loaded in the RD direction reveals

$$\beta\left(\eta^{\mathsf{H}}\right)=\begin{cases}1 \;\text{ for }\; \eta^{\mathsf{H}}\leq 0\\[1ex] 1-1.697\,\eta^{\mathsf{H}} \;\text{ for }\; \eta^{\mathsf{H}}>0\end{cases} \tag{6.2}$$

demonstrating good agreement with the data points shown in Fig. 6.5(a). Similarly, according to the experiments conducted on specimens loaded in DD, the function

$$\beta\left(\eta^{\mathsf{H}}\right)=\begin{cases}1 \;\text{ for }\; \eta^{\mathsf{H}}\leq 0\\[1ex] 1-1.595\,\eta^{\mathsf{H}} \;\text{ for }\; \eta^{\mathsf{H}}>0\end{cases} \tag{6.3}$$

has been formulated which is in good agreement with the data points shown in Fig. 6.5(b). Likewise, the results obtained from the experiments involving specimens subjected to loading in TD are utilized to propose the function as

$$\beta\left(\eta^{\mathsf{H}}\right)=\begin{cases}1 \;\text{ for }\; \eta^{\mathsf{H}}\leq 0\\[1ex] 1-1.467\,\eta^{\mathsf{H}} \;\text{ for }\; \eta^{\mathsf{H}}>0\end{cases} \tag{6.4}$$

also displaying good agreement with the data points as can be seen in Fig. 6.5(c). It's important to highlight that from the available data, a noticeable correlation between the parameter β and the generalized stress triaxiality η^{H} can be observed. Also, it is evident that the parameter β depends on the angle of loading direction as different β has been formulated for the loading of the specimens in RD, DD and TD. Analyzing Eqs. (6.2), (6.3) and (6.4), a function dependent on the generalized stress triaxiality η^{H} and the angle of loading direction θ is formulated as

$$\beta\left(\eta^{\mathsf{H}},\theta\right)=\begin{cases}1 \;\text{ for }\; \eta^{\mathsf{H}}\leq 0\\ k(\theta)\,\eta^{\mathsf{H}}+1 \;\text{ for }\; \eta^{\mathsf{H}}>0\end{cases} \tag{6.5}$$

where the loading direction dependent factor is given as

$$k(\theta)=-0.167\cos^{2}\theta-0.062\cos\theta-1.467\;. \tag{6.6}$$

The relationship of the damage parameter β with both the generalized stress triaxiality η^{H} and the angle of the loading direction θ is depicted in Fig. 6.5(d), displaying a good alignment with the existing data points. When, according to above equations, a negative value is obtained, the parameter β is set to zero. This situation arises in conditions of high hydrostatic tensile stress (high I_1^{H}), where the damage mechanism is driven by growth of voids and the impact of J_2^{H} is minimal.

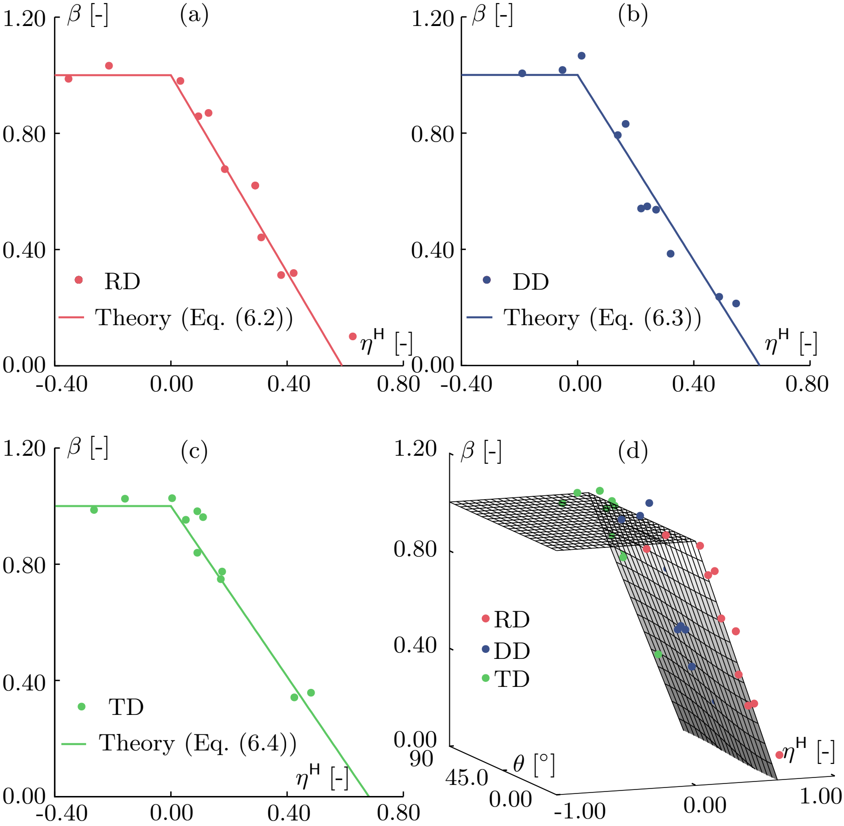

Figure 6.5: Dependence of parameter β on the generalized Hoffman stress triaxiality η^{H} and the loading direction θ.

6.2 Identification of parameters in the damage evolution equation

Due to the absence of experimental techniques at the micro-scale, identifying the micromechanically driven parameters $\tilde{\alpha}$ and $\tilde{\beta}$ in the damage rule (Eq. (2.62)) is particularly difficult. One potential approach to address this limitation is to conduct finite element analyses of unit-cells containing initial void, subjected to different stress-states to study the damage and fracture behavior. Three-dimensional finite element analyses of microscopic cell models have been suggested as a means to gain insight into damage and fracture processes in isotropic ductile materials. These analyses are utilized to investigate the evolution, growth, and deformation of micro-defects under various loading conditions, as documented in [13, 49, 70]. Their research demonstrated that void growth, the macroscopic deformation response of unit-cells, and the failure strain value were sensitive to the stress triaxiality. Research has also illustrated that the current stress-state has a significant impact on damage mechanisms at the microscale and, consequently, influences the corresponding macroscopic failure behavior.

Recently, Bryhni Dæhli et al. [41] performed the unit-cell simulations for plastically anisotropic materials using phenomenological anisotropic yield criteria Yld2004-18p developed by Barlat et al. [12]. They showed that the material anisotropy significantly influences the mechanical response of the unit-cell and the shape of the void evolves in distinct ways based on the orientation of the major principal stress relative to the material axes. Their analyses were further extended by Hosseini et al. [61] in which unit-cell simulations were performed where one of the loading directions is parallel to one of the material's symmetry axes and the other two making certain angle with the second and third orthotropic axes. It was found that the misalignment between loading and material axes results in changes of void growth and shapes throughout the loading process, and the material orientation affects the onset of localization and fracture in anisotropic metal products. Furthermore, the outcomes of the numerical simulations of isotopic ductile material on the unit-cell [30, 31], were utilized to discuss different damage and failure mechanisms. Phenomenological damage criteria and damage evolution equations were proposed and also the results were used to identify stress-state dependent parameters of the proposed continuum model.

In the following, similar approach of numerical studies on the unit-cell is used. A representative volume element (RVE) containing initial void is numerically simulated using the Hoffman yield criteria. The progression of macroscopic damage strains is examined through the unit-cell calculations conducted under various three-dimensional loading scenarios. The numerical findings are then employed to introduce a damage rule for anisotropic metals, while also identifying the corresponding material parameters.

6.2.1 Numerical analysis of the unit-cell

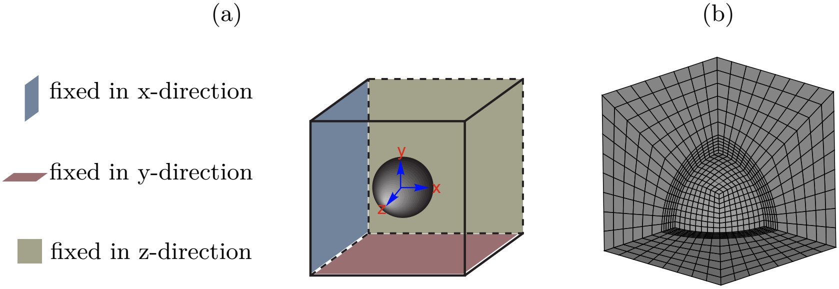

Figure 6.6: (a) Boundary conditions for the unit-cell and (b) cut view of one eighth of the unit-cell.

The finite element mesh of one-eighth of a RVE containing a spherical void at the center is shown in Fig. 6.6(b). The numerical simulations are performed using the commercial finite element software Ansys (APDL) version 18.0, which has been enhanced by UMAT taking the proposed phenomenological anisotropic material model into account. Eight noded solid element type Solid185 with orthotropical material properties is used. The origin of the coordinate system is at the origin of the pore, see Fig. 6.6(a) and the initial dimensions of the unit-cell are $l_x = 1\text{mm}$, $l_y = 1\text{mm}$ and $l_z = 1\text{mm}$. As was reported in [102], most of the pores in a cast iron with initial porosities between 0.3% to 3.7% were nearly spherical in shape. In the case of larger porosities, many of these pores were not spherical in shape. Furthermore, in [31] and [30], numerical simulations considering different shapes and sizes of pores with initial porosity ranging from 1% to 10% were conducted and studied in detail. It was shown that the results were not so different when compared to the results considering spherical shaped void with 3% initial porosity and it also lead to the good approximation for the determination of the state-

state-dependent parameters. As a result, this current study focuses on analyzing a spherical void with an initial void volume fraction of 3%.
The previous studies have already addressed the impact of various boundary conditions on numerical calculation outcomes [112, 113]. So, numerical simulations of the unit-cell with symmetrical and periodic boundary conditions were carried out and analyzed in detail by Hagenbrock [56]. It was concluded that the numerical investigation with periodic boundary conditions leads to almost no change in the results of the damage parameters of the damage model, so that the selected symmetry boundary conditions are sufficient for the analysis of the stress-states and identification of damage parameters. Hence, in the context of this work symmetrical boundary conditions, assuming that the material displays a regular porous microstructure, are used as shown in Fig. 6.6(a), where the yz-surface, xz-surface, and xy-surface of the unit-cell containing an initial void, as marked with different colors are fixed in x-, y-, and z-directions, respectively. The loads are applied in the form of displacements u_x, u_y and u_z. The displacements of the nodes of the outer surfaces located at the edges are coupled with the displacements of nodes located at the opposite edges, so that the displacements of the opposite pair of nodes are identical and the plane surfaces remain plane at the end of the numerical simulation. Depending upon the desired value of η^{H} and L^{H}, as in [56], the displacement u is scaled with the corresponding factors in the three main directions as,

$$u_1 = x_1 u, \quad u_2 = y_2 u, \quad u_3 = z_3 u, \tag{6.7}$$

where x_1, y_2 and z_3 are the scaling factors. For example, to achieve the stress-state $\eta^{\mathsf{H}} = 3/4$ and $L^{\mathsf{H}} = 0.23$, the value of the scaling factors reads $x_1 = 1$, $y_2 = 0.63$ and $z_3 = 0.27$. During the entire loading process, η^{H} and L^{H} are kept constant in order to study their influence on the damage and failure behavior. Thus, it is possible to analyze the damage and failure behavior of a unit-cell containing a void for wide range of η^{H} and L^{H}.
Based on the considered kinematics of the continuum damage model described in Chapter 2, the total strain rate tensor of the unit-cell is decomposed into elastic $\dot{\mathbf{H}}^{\mathsf{el}}$, effective plastic $\dot{\bar{\mathbf{H}}}^{\mathsf{pl}}$, and the damage part $\dot{\mathbf{H}}^{\mathsf{da}}$. This results in an additive decomposition of the macroscopic strain

rate tensor components along the principal directions (i) as

$$\dot{H}^{\mathsf{RVE}}_{(i)} = \dot{H}^{\mathsf{el}}_{(i)} + \dot{\bar{H}}^{\mathsf{pl}}_{(i)} + \dot{H}^{\mathsf{da}}_{(i)}. \tag{6.8}$$

While the unit-cell is under loading, the finite solid elements experience only elastic and plastic strain rates at the micro-level, denoted as $\dot{\mathbf{h}}^{\mathsf{el}}$ and $\dot{\mathbf{h}}^{\mathsf{pl}}$, respectively. Consequently, this gives rise to the corresponding elastic-plastic macroscopic strain rates

$$\dot{\mathbf{H}}^{\mathsf{ep}} = \dot{\mathbf{H}}^{\mathsf{el}} + \dot{\mathbf{H}}^{\mathsf{pl}} = \frac{1}{V}\int_{V_{matrix}} (\dot{\mathbf{h}}^{\mathsf{el}} + \dot{\mathbf{h}}^{\mathsf{pl}})\, dv \tag{6.9}$$

where V is the current volume of the unit-cell and V_{matrix} represents the current volume of the undamaged matrix material (solid elements). With Eq. (6.8) and Eq. (6.9), the macroscopic damage strain rate tensor is given by

$$\dot{\mathbf{H}}^{\mathsf{da}} = \dot{\mathbf{H}}^{\mathsf{RVE}} - \dot{\mathbf{H}}^{\mathsf{ep}}. \tag{6.10}$$

Using Eq. (2.21) and Eq. (2.22) leads to the calculation of damage strain tensor as

$$\mathbf{A}^{\mathsf{da}} = \int \dot{\mathbf{H}}^{\mathbf{da}}\, dt. \tag{6.11}$$

In the numerical investigations, the magnitude of strains and strain rates can be characterized using scalar-valued measures, such as the equivalent strain rate

$$\dot{\varepsilon}_{\mathsf{eq}} = \sqrt{\frac{2}{3}\dot{\mathbf{H}} \cdot \dot{\mathbf{H}}} \tag{6.12}$$

which is then used to calculate the equivalent strain given by

$$\varepsilon_{\mathsf{eq}} = \int \dot{\varepsilon}_{\mathsf{eq}}\, dt. \tag{6.13}$$

In addition the void volume fraction f is determined using

$$f = \frac{V - V_{matrix}}{V}. \tag{6.14}$$

6.2.2 Results of the numerical analysis of the unit-cell

The numerical study investigates the impact of loading on representative volume elements (RVE) containing voids under various load ratios $\mathrm{F}_x/\mathrm{F}_y/\mathrm{F}_z$ in different loading directions and examines their deformation and damage behavior in depth. Different loading scenarios are analyzed through numerical simulations using the elastic-plastic material model. Furthermore, the obtained results from the numerical simulations are compared with existing experimental observations derived from tests involving specimens subjected to biaxial loading conditions.

Fig. 6.7(a) shows the evolution of the principal components of damage strain tensor for the load ratio $\mathrm{F}_x/\mathrm{F}_y/\mathrm{F}_z$ in RD, DD and TD. As deformation increases, the damage strain A_x^{da} exhibits an upward trend, reaching up to 0.032 under loading in RD and TD, with slightly smaller values observed for loading in DD. The damage strain A_y^{da} attains -0.006 for loading in RD and TD whereas A_y^{da} for loading in DD is about 15% higher than in RD and TD. Furthermore, the damage strain A_z^{da} reaches upto -0.010 and is almost equal for all of the loading directions. The load ratio $\mathrm{F}_x/\mathrm{F}_y/\mathrm{F}_z = 1/0/0$ corresponds to the uniaxial loading, resulting in stress triaxiality $\eta^{\mathsf{H}} = 0.44$ and Lode parameter $L^{\mathsf{H}} = -0.70$ based on the Hoffman yield criterion.

The results for the load ratio $\mathrm{F}_x/\mathrm{F}_y/\mathrm{F}_z = 1/0/-1$ corresponding to shear loading conditions is presented in Fig. 6.7(b). The damage strain A_x^{da} increases up to 0.017 as the deformation of the RVE increases, while A_z^{da} decreases to -0.032, A_y^{da} remains nearly unchanged at 0.0. In this case, the effect of the loading direction on the formation of the principal damage strain is very small. The resulting Hoffman stress parameters are $\eta^{\mathsf{H}} = 0.21$ and $L^{\mathsf{H}} = 0.00$. Following the respective experiments involving the X0- and H-specimen done in [32, 37] under shear loading conditions, shear deformation at the micro-level, characterized by only very few initial voids, has been observed through scanning electron microscopy (SEM). This observation aligns with the numerically predicted components of the damage strain tensor, and notably, only a marginal influence of the loading direction has been observed.

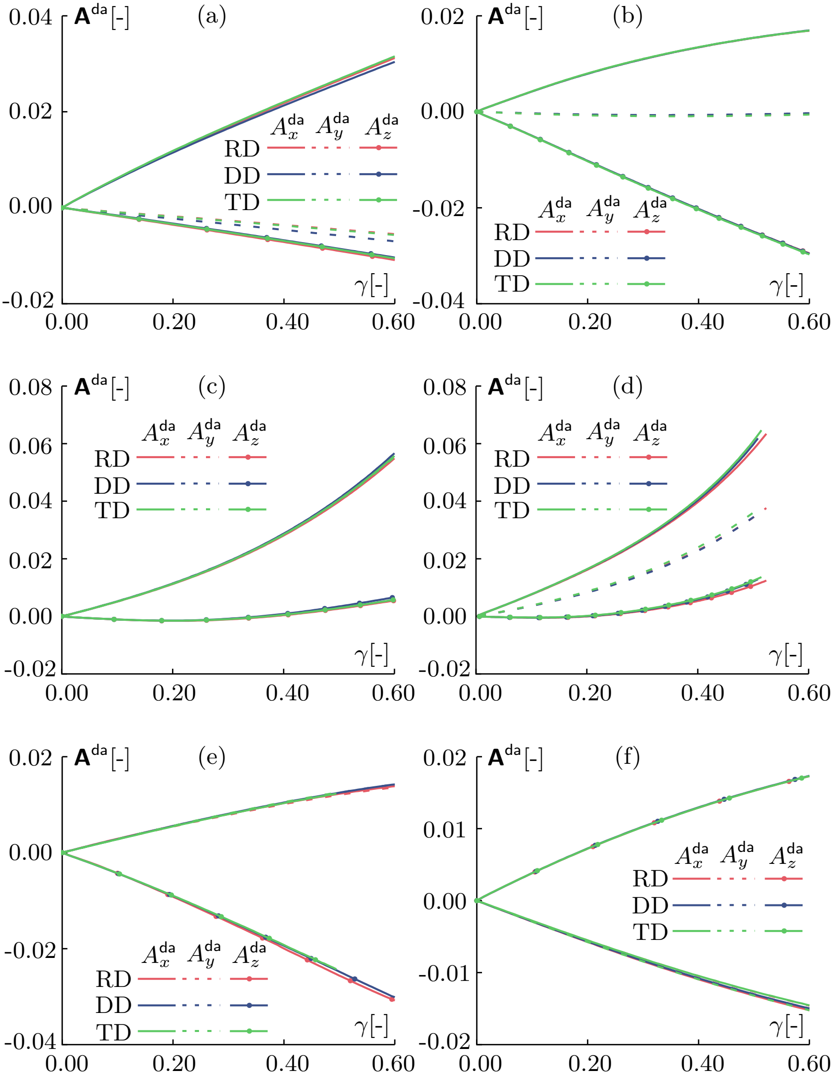

Figure 6.7: Evolution of principal damage strain tensors for (a) $\eta^{\mathsf{H}} = 0.44$ and $L^{\mathsf{H}} = -0.70$ (b) $\eta^{\mathsf{H}} = 0.21$ and $L^{\mathsf{H}} = 0.00$ (c) $\eta^{\mathsf{H}} = 0.66$ and $L^{\mathsf{H}} = 1.00$ (d) $\eta^{\mathsf{H}} = 0.75$ and $L^{\mathsf{H}} = 0.23$ (e) $\eta^{\mathsf{H}} = 0.33$ and $L^{\mathsf{H}} = 1.00$ and (f) $\eta^{\mathsf{H}} = -0.34$ and $L^{\mathsf{H}} = -1.00$.

Similarly, the formation of principal damage strains under the load ratio $\mathrm{F}_x/\mathrm{F}_y/\mathrm{F}_z = 1/1/0.25$ leading to the Hoffman stress parameters $\eta^{\mathsf{H}} = 0.66$ and $L^{\mathsf{H}} = 1.00$ is depicted in Fig. 6.7(c). The damage strain components A_x^{da} and A_y^{da}, for loading in RD, DD and TD, are nearly equal and attains a value of 0.057. The damage strain A_z^{da} is nearly 0.0 for all of the loading directions. In the experiment involving the X0-specimen under biaxial tension loading, a similar stress-state is attained [32]. Scanning electron microscopy (SEM) images (Fig. 7.6(a)) reveal a notable growth of voids for loading in all directions, while slightly smaller voids appearing after loading in RD as compared to loading in DD and TD.

Furthermore, Fig. 6.7(d) illustrates the increase of the principal damage strains with an increasing equivalent strain measure. In this case, the load ratio $\mathrm{F}_x/\mathrm{F}_y/\mathrm{F}_z = 1/0.63/0.27$ results in the stress triaxiality $\eta^{\mathsf{H}} = 0.75$ and Lode parameter $L^{\mathsf{H}} = 0.23$ based on the Hoffman yield criterion. The damage strain A_x^{da} increases up to 0.065 for the loading in TD but for loading in DD and RD the damage strain A_x^{da} is slightly smaller. Conversely, the damage strain components A_y^{da} and A_z^{da} show smaller increases, up to 0.04 and 0.01, respectively, with a similar dependence on the loading direction with respect to the rolling direction. Similar stress-state is achieved in the experiment with H-specimen under tensile loading condition [37], where SEM pictures (Fig. 7.13) reveal that the remarkable growth of the voids leads to the fracture of the specimen but the size of the voids are relatively smaller for loading in DD as compared to loading in RD and TD.

In addition, the damage strains under the load ratio $\mathrm{F}_x/\mathrm{F}_y/\mathrm{F}_z = 1/1/-0.5$ are shown in Fig. 6.7(e). The evolution of A_x^{da} and A_y^{da} is almost same for all loading directions and reaches a value of 0.014 while A_z^{da} decreases up to -0.030. The Hoffman stress parameters are $\eta^{\mathsf{H}} = 0.33$ and $L^{\mathsf{H}} = 1.00$, which are similar to the shear combined with tension loading in H-specimen [37]. The SEM images (Fig. 7.14(a)) depict the presence of small voids in combination with micro-shear-cracks leading to the fracture of the specimen.

Moreover, for the load ratio $\mathrm{F}_x/\mathrm{F}_y/\mathrm{F}_z = -1/-1/0.5$, the formation of damage strain components are shown in Fig. 6.7(f). As the loading increases, the damage strain components A_x^{da} and A_y^{da} decrease, reaching up to -0.015, while A_z^{da} increases up to 0.017. Importantly, this deformation behavior remains nearly unaffected by the loading direction. The

Hoffman stress parameters read $\eta^{\mathsf{H}} = -0.34$ and $L^{\mathsf{H}} = -1.00$.

Table 6.4: Generalized stress parameters for unit-cell

Load ratio $(F_x/F_y/F_z)$	L^{H} [-]	η^{H} [-]
• $-0.6/-0.4/-1$	• 0.75	• -0.6
• $-1/0.63/0.35$	• 0	• -0.9
• $-1/-1/0.5$	• -1	• -0.34
• $0.5/0.5/-1$	• 1	• 0.16
• $-1/0/-1$	• 0	• 0.21
• $1/-0.5/-0.5$	• -0.68	• 0.28
• $1/1/-0.5$	• 1	• 0.33
• $1/0.37/-0.27$	• 0.32	• 0.40
• $1/0/0$	• -0.7	• 0.44
• $1/1/0.25$	• 1	• 0.66
• $1/0.63/0.27$	• 0.23	• 0.75
• $1/0.4/0.4$	• -0.68	• 0.80

The Table 6.4 illustrates the total number of numerical simulations conducted, encompassing various loading ratios and the corresponding stress triaxialities and Lode parameters for loading in the RD. Based on the numerical results of the unit-cell, the stress-state dependent damage parameters $\tilde{\alpha}$ and $\tilde{\beta}$ in damage evolution equation Eq. (2.62) are identified. As can be seen in Fig. 6.7, the impact of the loading direction on the formation of damage strain components appears to be minimal. Therefore, this effect will be neglected while identifying $\tilde{\alpha}$ and $\tilde{\beta}$. This yields the function $\tilde{\alpha}$ as

$$\tilde{\alpha}\left(\eta^{\mathsf{H}}\right) = \begin{cases} 0.0672\eta^{\mathsf{H}} - 0.2421 & \text{for } \eta^{\mathsf{H}} < 0.21 \\ 2.5161\eta^{\mathsf{H}} - 0.7563 & \text{for } 0.21 \leq \eta^{\mathsf{H}} \leq 0.65 \\ 0.3067\eta^{\mathsf{H}} + 0.6797 & \text{for } \eta^{\mathsf{H}} > 0.65\,. \end{cases} \tag{6.15}$$

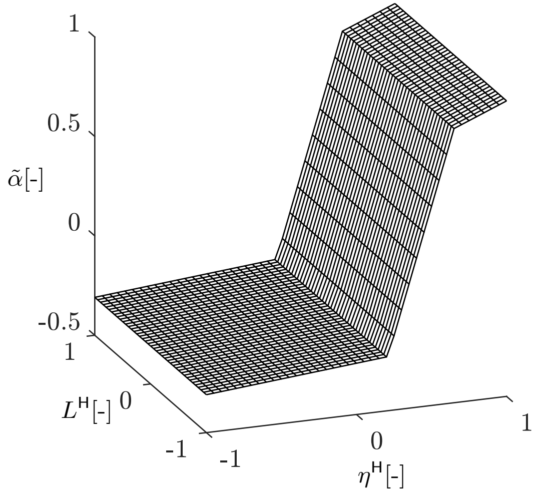

Figure 6.8: Dependence of the strain rate parameter $\tilde{\alpha}$ on the generalized Hoffman stress triaxiality η^{H} and the Lode parameter L^{H}.

As illustrated in Fig. 6.8, the parameter $\tilde{\alpha}$ is negative within the range of negative triaxialities and increases with increasing triaxiality. $\tilde{\alpha}$ is related to the volumetric part of the damage strain tensor. With an increase in triaxiality, the influence of the first invariants of the stress tensor $\mathbf{T}$ increases. It follows that the damage mechanism is dominated by isotropic growth of voids. The numerical simulations at the micro-scale have not revealed any dependence of $\tilde{\alpha}$ on the Lode parameter L^{H}.

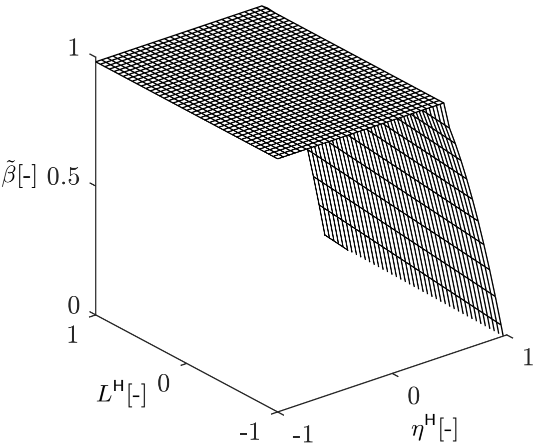

Figure 6.9: Dependence of the strain rate parameter $\tilde{\beta}$ on the generalized Hoffman stress triaxiality η^{H} and the Lode parameter L^{H}.

In addition, analyzing the numerical results, the parameter $\tilde{\beta}$ is determined as a function of stress triaxiality η^{H} and Lode parameter L^{H} as

$$\tilde{\beta}\left(\eta^{\mathsf{H}}, L^{\mathsf{H}}\right) = \begin{cases} 0.9821 \text{ for } \eta^{\mathsf{H}} < 0.45 \\ 1.2442 \; - \; 1.2735(\eta^{\mathsf{H}})^2 + f_{\tilde{\beta}}(L^{\mathsf{H}}) \text{ for } \eta^{\mathsf{H}} \geq 0.45 \end{cases} \tag{6.16}$$

with $f_{\tilde{\beta}}(L^{\mathsf{H}}) = 0.0447 L^{\mathsf{H}}$.

Examining the graphical representation (Fig. 6.9) of the function $\tilde{\beta}$ given in Eq. (6.16) reveals the contrary behavior compared to the parameter $\tilde{\alpha}$. The influence of $\tilde{\beta}$ decreases as the stress triaxiality η^{H} increases. For small triaxialities, $\tilde{\beta}$ is nearly equal to one, which indicates that the damage mechanism is characterized by the evolution of micro-shear-cracks. Additionally, in the regime of higher positive stress triaxialities, the micro-mechanical numerical calculations have identified an additional dependence on the Lode parameter, which is modeled by the term $f_{\tilde{\beta}}(L^{\mathsf{H}})$.

Numerical studies of the unit-cell containing an initial void have been carried out for a wide range of stresses with stress triaxiality η^{H} and Lode parameter L^{H} based of the Hoffman yield criteria. The numerical results have been utilized to discuss general mechanisms of damage and failure in ductile materials. Furthermore, the RVE is loaded with different load ratios in different directions, namely in RD, DD and TD, with respect to the RD. Based on these studies, the evolution of components of the damage strain tensors are analyzed in detail demonstrating the effect of the stress state. In addition, the influence of the loading direction on the formation of damage strain tensors is also shown, although the effect was found to be minimal. Based on the numerical results, the functions for the stress-state-dependent damage parameters $\tilde{\alpha}$ and $\tilde{\beta}$ appearing in the damage evolution equation (Eq. (2.62)) of macroscopic damage strains associated with anisotropic evolution of micro-defects are identified.

With all of the stress-state-dependent parameters α, β, $\tilde{\alpha}$ and $\tilde{\beta}$, the proposed continuum damage model taking plastic anisotropy into account must be validated. Thus, in the following Chapter the experimental results from the biaxially loaded specimens are compared with the numerical results.

7 Experimental and numerical results from biaxially loaded specimens

In this Chapter the experimental and the corresponding numerical results of the tests with the biaxial test specimens are presented. The numerical simulations are carried out taking elastic-plastic-damage material model into account. Through the comparison of global and local results, it can be ensured that meaningful insights into the damage and failure behavior are obtained. This allows for drawing the conclusions regarding the modeling approach and the quality of the calibrated material parameters.

7.1 X0-specimens

7.1.1 Global force-displacement diagrams

Fig. 7.1 presents the load-displacement curves obtained from the experiments with different load ratios for different loading directions, along with corresponding numerical simulations. For the load case $\mathrm{F}_1/\mathrm{F}_2 = 1/0$ (Fig. 7.1(a)), the specimen fails after attaining the maximum load of $\mathrm{F}_1 = 9.26\mathrm{kN}$ and the displacement $\mathit{\Delta}\mathrm{u}_{\mathrm{ref}} = 1.08\mathrm{mm}$ after loading the specimen in RD. Similarly, the maximum load for TD reaches up to $\mathrm{F}_1 = 9.12\mathrm{kN}$ and failure occurs at the displacement of $\mathit{\Delta}\mathrm{u}_{\mathrm{ref}} = 1.21\mathrm{mm}$. The lowest attained load is observed after loading in DD, which is approximately 4% less than that one for RD. However, the displacement at fracture, $\mathit{\Delta}\mathrm{u}_{\mathrm{ref}} = 1.35\mathrm{mm}$, for DD is the highest among all three loading directions. The disparity in the material's mechanical response clearly highlights the influence of the loading directions relative to the principal directions of anisotropy. These experimental results suggest that loading in RD results in a more brittle behavior, while loading in DD leads to a more ductile behavior. The observed experimental behavior is successfully replicated by the numerical simulations, particularly for loading in RD and TD. The load–displacement curves from both experimental and numerical data closely align, with minor differences becoming apparent after loading in DD. Nonetheless, the primary trends are accurately captured in the simulations.

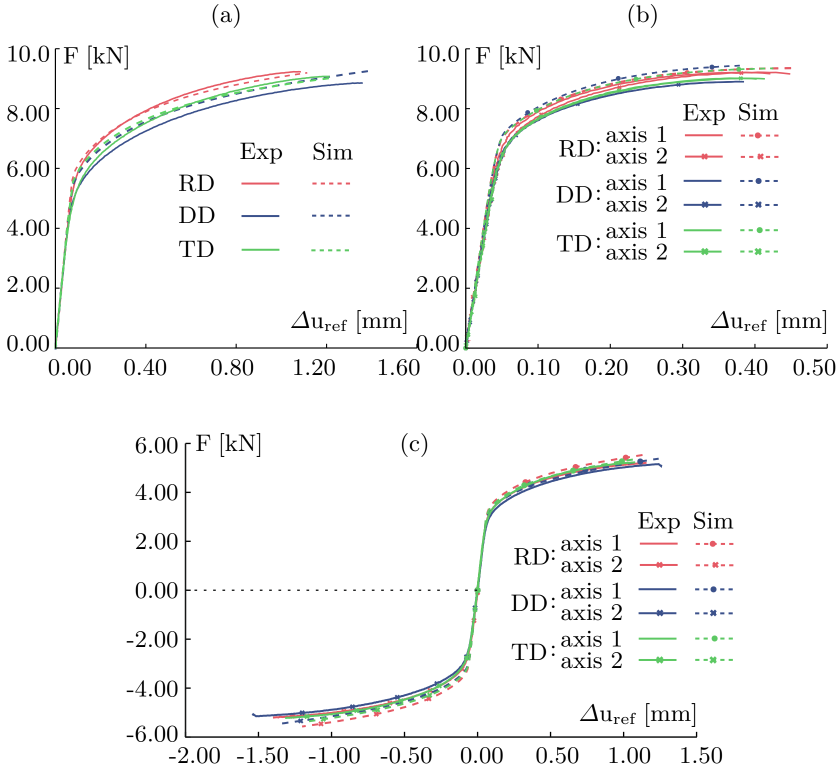

Figure 7.1: Experimental and numerical load-displacement curves using X0-specimen for the load ratio (a) $F_1/F_2 = 1/0$, (b) $F_1/F_2 = 1/1$ and (c) $F_1/F_2 = 1/-1$.

For the load ratio $F_1/F_2 = 1/1$ (Fig. 7.1(b)), in case of RD, the maximum attained loads in both axes are $F_1 = F_2 = 9.24\mathrm{kN}$ and the failure occurs at the displacement of $\Delta u_{ref.1} = 0.42\mathrm{mm}$ and $\Delta u_{ref.2} = 0.45\mathrm{mm}$ in axis

1 and axis 2, respectively. Again, for TD, the fracture occurred at the displacements of $\Delta u_{ref.1} = 0.40$mm and $\Delta u_{ref.2} = 0.41$mm and the corresponding maximum loads are $F_1 = F_2 = 9.01$kN, respectively. In each case, slight non-symmetric behavior is observed in the values of displacements at the specimen's failure. This could be attributed to minimal inaccuracies during the experiments or the inhomogeneities in the geometry of the specimen arising from the manufacturing processes. After loading in DD, the load reaches up to $F_1 = F_2 = 8.92$kN and the specimen fails after reaching the displacements of $\Delta u_{ref.1} = \Delta u_{ref.2} = 0.38$mm for both axes. Compared to the load ratio $F_1/F_2 = 1/0$, for $F_1/F_2 = 1/1$, all of the specimens failed earlier after loading in RD, DD and TD. Once again, the loading direction with respect to the principal directions of anisotropy influences the maximum loads and displacements at the onset of fracture. The observed experimental behavior is effectively reproduced by the numerical simulations, particularly for loading in RD, the experimental and numerical load–displacement curves closely match. However, for loading in DD and TD, the maximum loads are slightly overpredicted with the difference around 5%.

The load–displacement curves, in case of loading in RD, obtained from experiments with the load ratio $F_1/F_2 = 1/-1$ (Fig. 7.1(c)) show nearly identical load maxima for both axes at failure, with $F_1 = 5.27$kN and $F_2 = -5.14$kN. However, minor differences in the final value of the displacements are observed among the loading directions. For instance, after loading in DD, the maximum displacements at fracture are $\Delta u_{ref.1} = 1.25$mm and $\Delta u_{ref.2} = -1.5$mm. For loading in TD, these displacements are approximately 17% and 14% less than those observed in DD. Similarly, the final values of the displacements for RD lie between those of DD and TD. Again, noticeable differences are observed in the values of the displacements reached at the onset of fracture, indicating the influence of the loading direction with respect to the principal directions of anisotropy. They once again demonstrate that the behavior for loading in DD is more ductile compared to the other loading directions. Additionally, the numerical simulations agree well with the experimental results. Specifically, for loading in DD and TD, the numerically predicted curves closely match the experimental ones. Although the maximum load for loading in RD is slightly overpredicted, the overall trends are well captured by the numerical simulations.

7.1.2 First principal strain fields

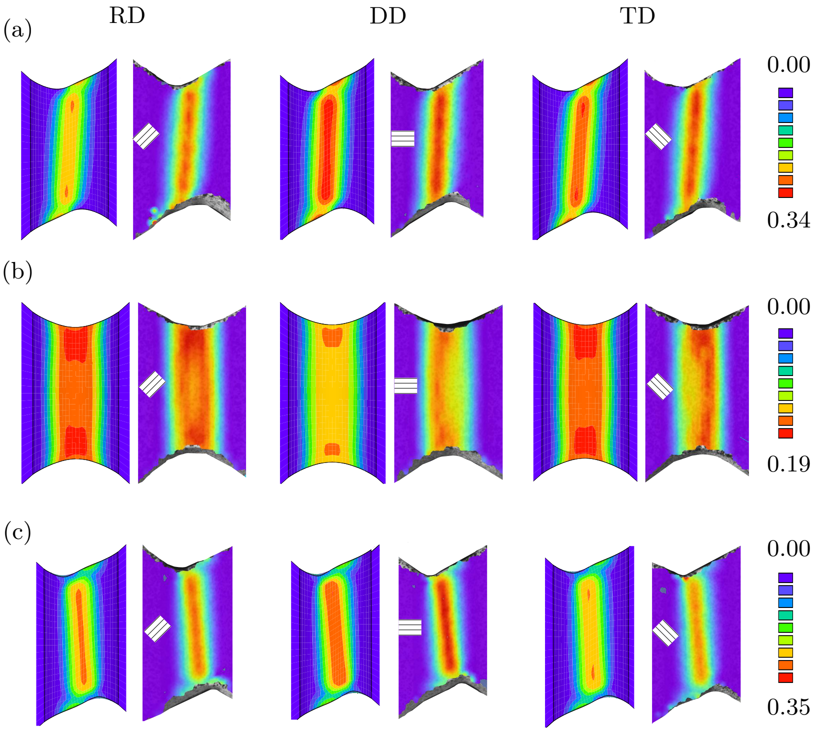

Figure 7.2: First principal strains from the DIC (right) and the numerical simulations (left) for the load ratios (a) $F_1/F_2 = 1/0$, (b) $F_1/F_2 = 1/1$ and (c) $F_1/F_2 = 1/-1$.

Fig. 7.2 displays the distribution of the first principal strains (A_1) obtained from the DIC and the respective numerical simulations. The local first principal strains are captured shortly before the final failure of the specimen, considering different load ratios and orientations with respect to the principal directions of anisotropy. On each of the results obtained from the experiments, the black lines in a rectangular box show the rolling direction.

For the loading ratio $\mathrm{F}_1/\mathrm{F}_2 = 1/0$ (Fig. 7.2(a)), small strain bands are formed and they are diagonally oriented from top right to the bottom left making an angle of about 4° with respect to the vertical axis.
A_1 is distributed more uniformly along the shear band for DD than those in RD and TD and its maximum value $A_1 = 0.34$ is also significantly greater than for the loading in RD and DD. The principal strains are numerically well predicted if compared to the experimental ones, for all loading directions. Moreover, in the loading case of $\mathrm{F}_1/\mathrm{F}_2 = 1/1$ which is depicted in Fig. 7.2(b), the principal strains are vertically widespread forming an elliptical-shaped vertical band. The maximum value of A_1 is observed for RD and TD, reaching up to 0.19, while the principal strain for DD is relatively lower which is about 0.15. Both the values and the form of the principal strain bands are numerically well captured for the respective experiments.
In addition, the strain bands are localized diagonally from top left to the bottom right forming a band with width about 3mm for the load ratio $\mathrm{F}_1/\mathrm{F}_2 = 1/-1$, which is shown in Fig. 7.2(c). In this case the maxima are $A_1 = 0.30$ and $A_1 = 0.28$, for loading in RD and TD, respectively, whereas A_1 for DD is maximum among all and reaches up to 0.35. The numerical results for RD and TD match well with the experiment but the value of A_1 for DD is numerically underpredicted compared to the corresponding experimental value.

7.1.3 Stress-state

From the numerical simulations of the respective experiments, it is possible to analyze the stress-state, both the attained magnitudes and the distribution, using the stress triaxiality η^{H} based on the Hoffman yield condition. For this purpose, Fig. 7.3 shows the stress triaxiality on the surface (S) and in the cross section (C) of the notches of the X0-specimen, which are evaluated at the last load step of the numerical simulations.
For the load ratio $\mathrm{F}_1/\mathrm{F}_2 = 1/0$ (Fig. 7.3(a)), the stress triaxiality for RD in the cross-section (C) is nearly homogeneously distributed with $\eta^{\mathsf{H}} = 0.62$.

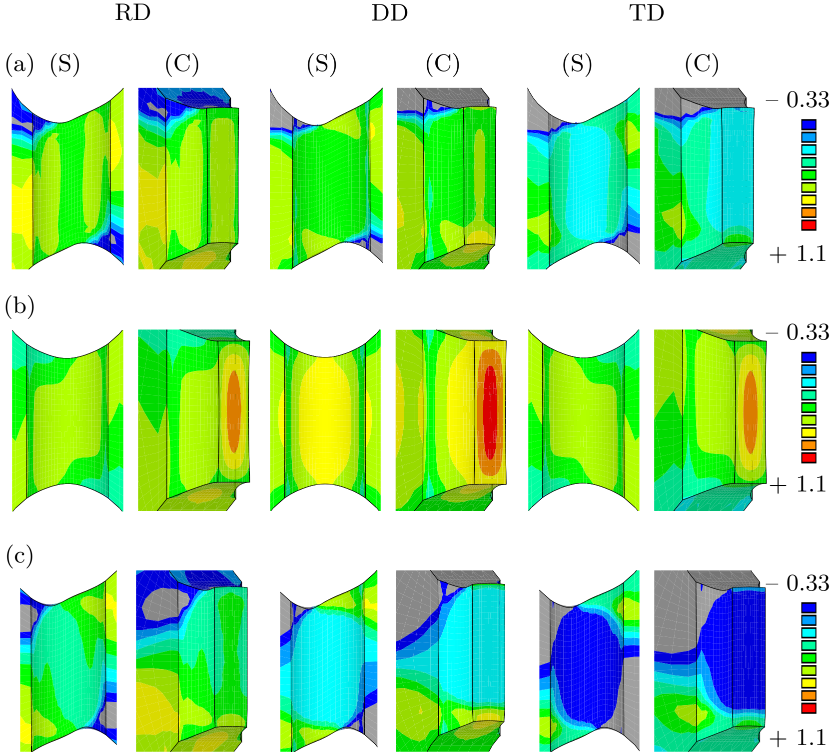

Figure 7.3: Stress triaxialities for the load ratios (a) $F_1/F_2 = 1/0$, (b) $F_1/F_2 = 1/1$ and (c) $F_1/F_2 = 1/-1$.

In the case of loading in DD, $\eta^{H} = 0.62$ at the center, but small gradients can be observed on the bottom, top, as well as on the right and left sides from the center. But for TD, $\eta^{H} = 0.30$ and evenly distributed over the cross-section. A clear influence of the loading direction on the stress triaxialities is observed for this loading.
In case of $F_1/F_2 = 1/1$, higher gradients of the stress triaxiality can be seen in the cross-section (C) with η^{H} reaching up to 1.1 for loading in DD. Similarly, for RD and TD, $\eta^{H} = 0.94$ in the center with higher gradients across the cross-section, whereas $\eta^{H} = 0.62$ and the distribution is

quite homogeneous for the larger part on the surface (S). The influence of the loading direction on the stress triaxialities for this loading case is marginal.
Furthermore, the stress triaxialites for the load ratio $\mathrm{F}_1/\mathrm{F}_2 = 1/-1$ are shown in Fig. 7.3(c). Again, η^{H} is nearly uniformly distributed in the cross-section (C), with small gradients on the top and bottom. For loading in TD, $\eta^{\mathsf{H}} = -0.33$ is numerically predicted both in the cross-section and on the surface. Contrarily, for loading in DD, both in the cross-section and on the surface, the numerically predicted stress triaxiality η^{H} is nearly equal to 0, whereas the value of $\eta^{\mathsf{H}} = 0.20$ for RD is slightly higher than that of DD and TD. The influence of the loading direction on the prediction of stress triaxialities is clearly evident.

7.1.4 Inelastic strains

The distributions and magnitudes of the numerically predicted equivalent plastic strains γ on the surface (S) of the notched region and in the cross-section (C) are shown in Fig. 7.4, which are taken at the final load steps. In particular, for the load ratio $\mathrm{F}_1/\mathrm{F}_2 = 1/0$ (Fig. 7.4(a)), the maximum $\gamma = 0.41$ occurs for loading in DD on the surface (S) of the notch in a localized band with a slightly diagonal orientation from top right to bottom left. Similarly, for TD, γ is nearly equal to that one in DD, but for loading in RD, γ is about 7% lower than that of other loading directions. The distribution of the equivalent plastic strains in the cross-section for RD and TD is almost similar, whereas $\gamma = 0.41$ has a higher value for DD along the right and left edges of the cross-section than those in RD and TD.

Furthermore, in the case of $\mathrm{F}_1/\mathrm{F}_2 = 1/1$ (Fig. 7.4(b)), the equivalent plastic strains on the surface (S) are widespread, forming a vertical band for all the loading directions. In the cross-section, the distribution of γ is nearly homogeneous, with γ reaching up to 0.27 at the center for RD and TD, whereas γ is only 0.22 for loading in DD.
In addition, as shown in Fig. 7.4(c), for the loading ratio $\mathrm{F}_1/\mathrm{F}_2 = 1/-1$, the equivalent plastic strains form a band from top left to the bottom right on the surface of the notch. The equivalent plastic strain band for DD is more wider than those for RD and TD, with a maximum $\gamma = 0.41$. For RD and TD, $\gamma = 0.34$ is reached in the cross-section

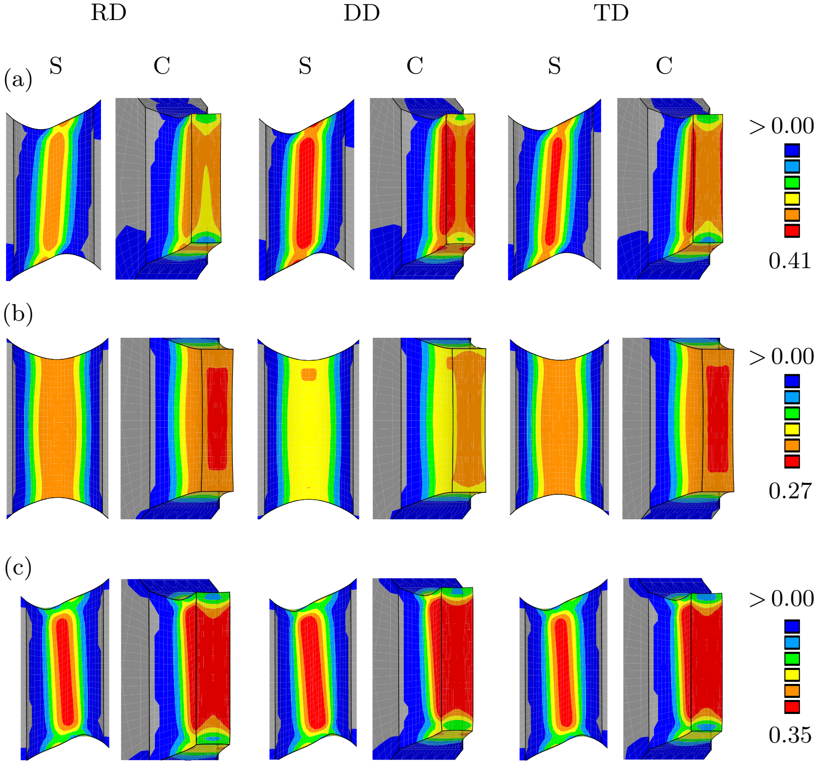

Figure 7.4: Numerically predicted equivalent plastic strains γ for the load ratios (a) $F_1/F_2 = 1/0$, (b) $F_1/F_2 = 1/1$ and (c) $F_1/F_2 = 1/-1$.

with small gradients at the top and the bottom. Similar behavior can be observed for DD, with its maximum $\gamma = 0.35$ across the center with slight gradients at the top and bottom part of the cross-section (C) of the notch.

Similarly, the equivalent damage strains μ from the numerical simulations are illustrated in Fig. 7.5. The equivalent damage strains on the surface (S) also form a localized shear band inclined from top right to the bottom left for the load ratio $F_1/F_2 = 1/0$ (Fig. 7.5(a)). The shear bands for RD and DD are more narrower, with their maximum in two points reaching $\mu = 0.25\%$ and $\mu = 0.31\%$, respectively, compared to those for TD. Moreover, μ is distributed nearly uniformly across the cross-section for all loading directions and its maximum $\mu = 0.31\%$ is predicted for TD at the central area in the cross-section.

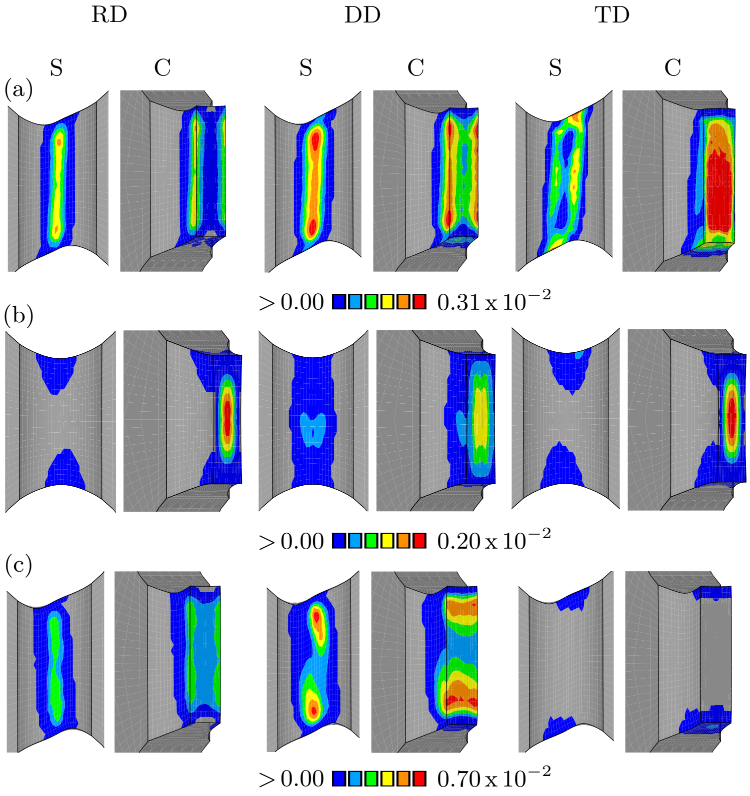

Figure 7.5: Numerically predicted equivalent damage strains μ for the load ratios (a) $F_1/F_2 = 1/0$, (b) $F_1/F_2 = 1/1$ and (c) $F_1/F_2 = 1/-1$.

For the load ratio $F_1/F_2 = 1/1$ (Fig. 7.5(b)), the equivalent damage strains in the cross-section are distributed in the ellipsoidal form showing a maximum value of $\mu = 0.20\%$ in the center for RD and TD, whereas μ reaches only up to 0.13% for loading in DD. On the surface, μ is numerically predicted, but the magnitude is far less compared to that in the cross-section for all loading directions.

Moreover, for the load ratio $F_1/F_2 = 1/-1$ (Fig. 7.5(c)), only in the case of RD, a localized uniform band of μ oriented diagonally is formed. But for DD, the equivalent damage strains are not uniform and are strongly localized on the top and bottom part of the surface with the maximum $\mu = 0.70\%$ among all of the loading directions, as can be observed in Fig. 7.4(c). On the other hand, μ is predicted only on the top and bottom edges of the surface for TD. The equivalent damage strains for RD in the cross-section are almost homogeneously distributed, while the distribution for DD is uneven, with $\mu = 0.70\%$ at the lower area of the cross-section.

7.1.5 SEM images and fracture behavior

The images in Fig. 7.6 and Fig. 7.7 display the fractured X0-specimens from all load cases, along with the results of the examinations of the fracture surfaces using the scanning electron microscope. The specimens failed abruptly in all experiments, and no development of a fracture process over time could be observed with the DIC system. In the majority of cases, the specimens fractured in two opposing notches as shown. For almost all the load ratios and loading directions, the localized bands of the first principal strain (Fig. 7.2) correspond to the fracture lines. In particular, for the load ratio $F_1/F_2 = 1/0$ (Fig. 7.6(a)), the fracture lines are slightly inclined from top-left to bottom-right making about 5° with the horizontal axis. This type of fracture mode is typical for low positive stress triaxialites (Fig. 7.3(a)) where the failure of the specimens result due the combination of the growth of micro-shear cracks and micro-voids. The fracture lines are nearly parallel to the horizontal axis in the case of $F_1/F_2 = 1/1$ (Fig. 7.6(b)) for all loading directions. Moreover, the fracture modes resemble to the cup-cone ductile fracture caused by tensile-dominated loading. Similarly, for the load ratio $F_1/F_2 = 1/-1$ (Fig. 7.7), the fracture lines are slightly diagonally oriented from bottom-left to top-right forming nearly 7° with the horizontal axis, indicating typical shear-dominated fracture modes with smooth fracture surfaces.

These experimental findings demonstrate that fracture patterns at the macroscopic level are influenced by the load ratios, while the impact of the loading direction (RD, DD, or TD) is marginal.

The pictures of the fracture surfaces taken from the SEM for the load ratio $F_1/F_2 = 1/0$ (Fig. 7.6(a)) after loading in RD reveal numerous sheared micro-voids, resulting in sheared dimples. But for loading in DD, fewer small micro-voids are present, and they appear to be more sheared, leading to the formation of micro-shear cracks. However, for loading in TD, there is a notable presence of both micro-voids and micro-shear mechanisms in comparison to RD and DD. This observation for TD could explain the numerical results (Fig. 7.5(a)), in which the maximum equivalent damage strain in the cross-section is predicted for loading in TD.

On the contrary, in the case of the load ratio $F_1/F_2 = 1/1$ (Fig. 7.6(b)), loading in RD results in significant void growth, characterized by large pores and distinct dimples. Again, large pores and coarse dimples similar to those observed for RD can be seen after loading in TD. However, smaller voids resulting in dimples, of a reduced scale than those in RD and TD, are observed for loading in DD. These observed differences in SEM images seem to be consistent with the numerically predicted equivalent damage strains (Fig. 7.5(b)), where the maximum value of μ in the cross-section of the notch is higher for RD and TD than for DD.

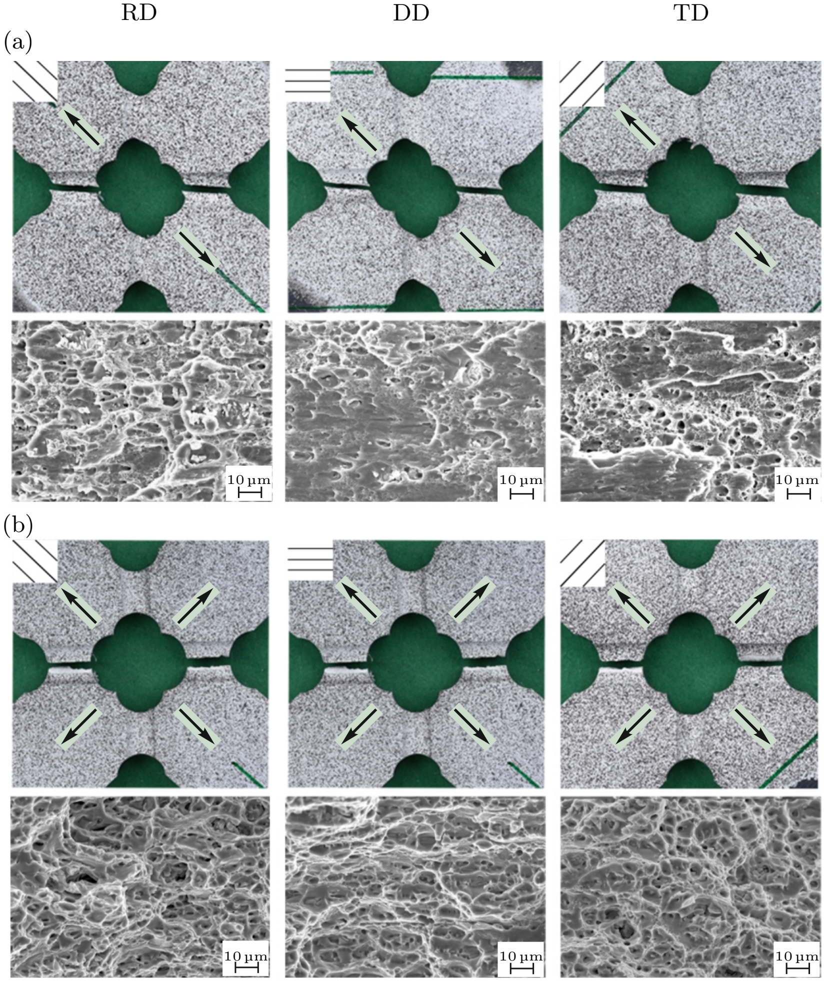

Figure 7.6: Fractured X0-specimens and the corresponding SEM pictures of the fracture surfaces for the load ratios (a) $F_1/F_2 = 1/0$ and (b) $F_1/F_2 = 1/1$.

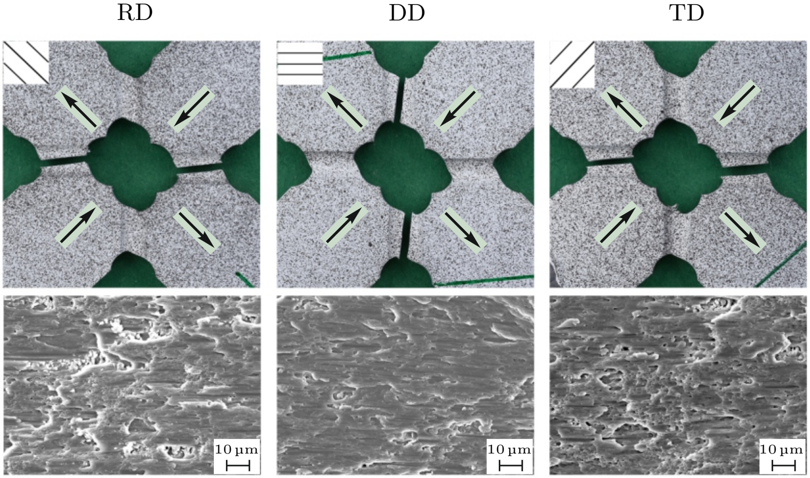

Figure 7.7: Fractured X0-specimens and the corresponding SEM pictures of the fracture surfaces for the load ratio $F_1/F_2 = 1/-1$.

For the load ratio $F_1/F_2 = 1/-1$, as depicted in Fig. 7.7, after loading in RD, a relatively small number of micro-voids, which are distinctly sheared and overlaid with micro-shear cracks, are observed. For loading in TD, similar to RD, only a few sheared micro-voids, superimposed with micro-shear cracks, are present. But in case of DD, almost no voids are observed, and the failure is attributed to the accumulation of micro-shear cracks, resulting in a notably smooth and flat failure surface. This fracture mode is characteristic for stress triaxialities with nearly zero or negative values (Fig. 7.3(b)). The equivalent damage strains from the numerical analysis is maximum for loading in DD both in the cross-section and in the surface as compared to RD and TD (Fig. 7.5(c)). These numerical results once again correspond to the fracture images, as the presence of micro-shear cracks for DD exceeds those of RD and TD.

In summary, while the dependence of macroscopic fracture lines on the loading direction is not evident in the experimental analysis, minor differences are clearly observable in the influence of the loading direction on the images captured by SEM. Moreover, slight variations can be observed in the load-displacement diagrams. For example, for loading ratios $F_1/F_2 = 1/0$ and $F_1/F_2 = 1/-1$ resulting in moderate, low positive, zero or negative stress triaxialities, loading in DD leads to larger displacements, indicating more ductile behavior corresponding to shear-dominated behavior at the micro-level. Similarly, the experimental and numerical observations of the first principal strains in Fig.7.2 clearly illustrate the influence of both loading direction and load ratio. For instance, just before the final failure of the specimen, the distribution and values of the accumulated first principal strains after loading in RD differ from those after loading in DD and TD (Fig. 7.2(b)). The numerically predicted values and distribution of the equivalent plastic strains (Fig. 7.4) and the equivalent damage strains (Fig. 7.5) also predict the effect of loading directions in the specimen, which tends to align with the experimental results.

7.2 H-specimens

7.2.1 Global force-displacement diagrams

The experimentally obtained load-displacement diagrams involving H-specimen under various load ratios and loading directions are compared in Fig. 7.8. For the load ratio $F_1/F_2 = 0/1$ depicted in Fig. 7.8(a), the H-specimen undergoes failure upon reaching a maximum load of $F_2 =$ 12.89kN and a displacement of $\varDelta u_{ref} = 0.50$mm after loading in RD. Likewise, for TD, the maximum load is nearly equal to that of RD, but the specimen failed at the displacement $\varDelta u_{ref} = 0.57$mm. For the specimen loaded in DD, F_2 reaches up to 12.48kN and the displacement at fracture is $\varDelta u_{ref} = 0.56$mm. The difference in the maximum attained load between the highest (in RD) and the lowest (in DD) orientations is about 3%, whereas a difference of approximately 12% in the value of displacements at failure is observed between loading in TD and RD. These differences indicate that the specimens loaded in TD and DD, with respect to the rolling direction, exhibit more ductile behavior compared to the specimen loaded in RD. The corresponding numerical simulations were conducted, demonstrating good agreement with the experimental load–displacement curves. Although a slight over-prediction in loads is evident for this load ratio, the primary trends are well captured.

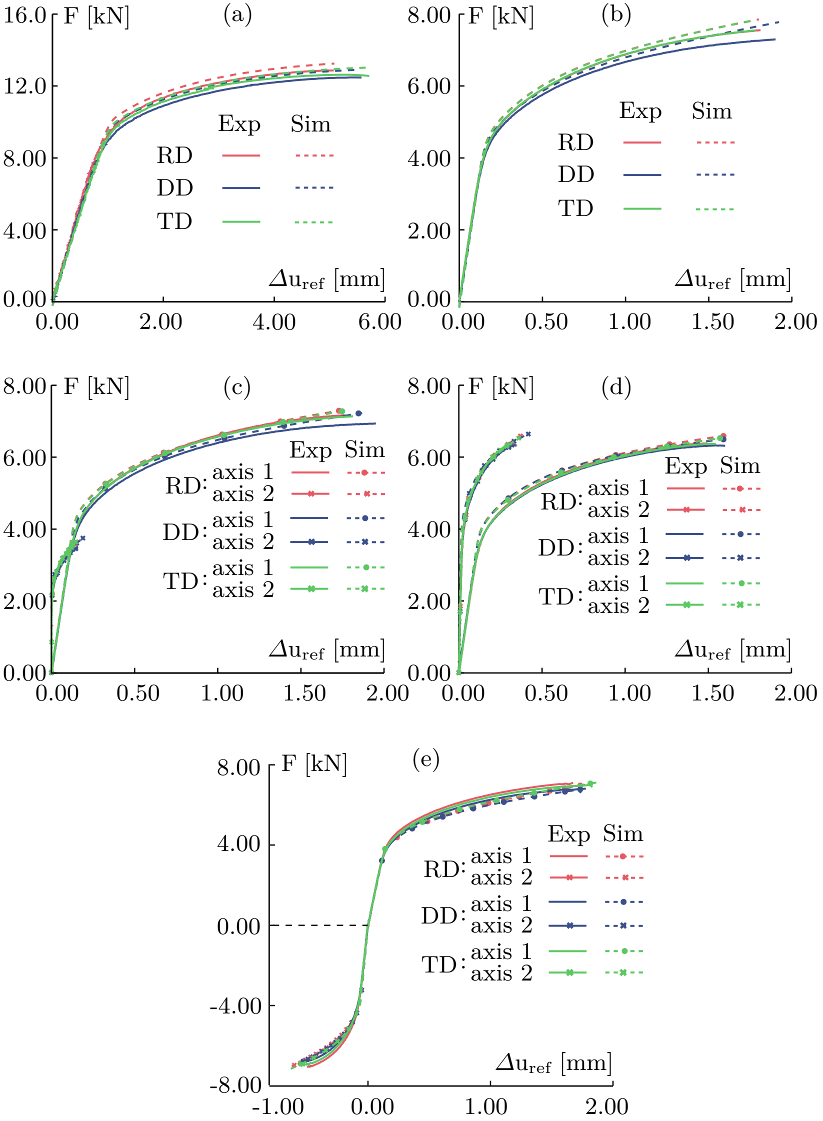

Figure 7.8: Experimental and numerical load-displacement curves using H-specimen for the load ratios (a) $F_1/F_2 = 0/1$, (b) $F_1/F_2 = 1/0$, (c) $F_1/F_2 = 1/0.5$, (d) $F_1/F_2 = 1/1$ and (e) $F_1/F_2 = 1/-1$.

Furthermore, in case of $F_1/F_2 = 1/0$ (Fig. 7.8(b)), the maximum load at specimen's failure after loading in RD and TD are almost the same, measuring $F_1 = 7.57$kN, whereas the measured displacements are $\Delta u_{ref} = 1.81$mm and $\Delta u_{ref} = 1.78$mm, respectively. However, the maximum load for DD is around 3% less than those of RD and TD. Conversely, the highest value of displacement, $\Delta u_{ref} = 1.90$mm at failure, is reached after loading in DD compared to the other loadings. Once again, these observations indicate that the specimens show slightly brittle behavior after loading in TD and RD, while loading in DD shows more ductile behavior. The numerical simulations agree well with the corresponding experimental results, with slight differences observed in the load maxima.

For the load ratio $F_1/F_2 = 1/0.5$ (Fig. 7.8(c)), after loading in RD and TD in axis 1, the maximum attained loads $F_1 = 7.18$kN and the displacements $\Delta u_{ref} = 1.77$mm at specimen's failure are equal for both. Similarly, in the case of RD and TD, the maximum loads and the displacements at the onset of fracture in axis 2 are identical, with values of $F_1 = 3.60$kN and $\Delta u_{ref} = 0.14$mm, respectively. Loading in DD in axis 1 yields the lowest, measuring $F_1 = 6.97$kN, while achieving the maximum displacement of $\Delta u_{ref} = 1.97$mm at the onset of failure of the specimen. The behavior after loading in DD is again slightly more ductile compared to loading in RD and TD. In addition, the numerically predicted load-displacement curves align well with the corresponding experimental curves.

The load maxima in the case of $F_1/F_2 = 1/1$, for all loading directions, are nearly similar with $F_1 = F_2 = 6.35$kN. Nevertheless, there are differences in the displacements at the onset of failure. In RD the specimen failed at $\Delta u_{ref.1} = 1.40$mm and $\Delta u_{ref.2} = 0.34$mm, while loading in TD resulted in displacements of $\Delta u_{ref.1} = 1.54$mm and $\Delta u_{ref.2} = 0.34$mm. Moreover, in DD , the maximum displacement of $\Delta u_{ref.1} = 1.61$mm is reached, once again marking the highest value among all loading directions. Therefore, loading the H-specimen in DD exhibits more ductile behavior compared to loading in RD and TD. The load-displacement curves are in good agreement with the experimental ones as seen in Fig. 7.8(d)).

Moreover, for the load ratio $F_1/F_2 = 1/-1$, the maximum attained load after loading in RD and TD are nearly equal, measuring $F_1 = F_2 = 7.15$kN and $F_1 = F_2 = -7.01$kN. However, the displacements at the onset of failure vary with $\Delta u_{ref.1} = 1.67$mm and $\Delta u_{ref.1} = 1.80$mm, respectively. In addition, loading in DD yields in a load of $\mathrm{F}_1 = 6.75\mathrm{kN}$ along with a displacement of $\Delta \mathrm{u}_{\mathrm{ref.1}} = 1.70\mathrm{mm}$ at the onset of specimen's fracture. In this loading case, the specimens loaded in TD show more ductile behavior, whereas those loaded in RD exhibit brittle behavior compared to other (DD and TD). For all loading directions, the numerical simulations slightly underpredict the load-displacement curves compared to the experiments, but the overall trend is well captured.

7.2.2 First principal strain fields

The first principal strain (A_1) fields from the DIC and the corresponding numerical simulations are shown in Fig. 7.9. The local first principal strains are taken shortly before the final fracture of the specimen for different load ratios and for different orientations with respect to the principal directions of anisotropy. As already mentioned, the experimental values are the mean values of the four notches of all experiments corresponding to the specific load case and the rolling direction.

For the load case $\mathrm{F}_1/\mathrm{F}_2 = 0/1$ (Fig. 7.9(a)), broad vertical bands of principal strains are formed for all directions and the vertical bands appear elliptical in shape for loading in RD and DD. A_1 is maximum for DD, reaching up to 0.18, but the principal strains for RD and DD are approximately 22% and 11% lower than DD, respectively. The corresponding numerical results are in good agreement with the experimental ones. As depicted in Fig. 7.9(b), for all the loading directions, the principal strain bands for $\mathrm{F}_1/\mathrm{F}_2 = 1/0$ are diagonally orientated from top right to bottom left and the bands are not broadly spread like in load case $\mathrm{F}_1/\mathrm{F}_2 = 0/1$. Among the three loading directions, A_1 reaches its maximum value of 0.35 for DD, while the bands are narrower compared to loading in RD and TD. The principal strains for RD and TD are nearly equal, measuring 0.33. The orientation of principal strain bands from the numerical simulations agree well with the experimental results, but there is approximately a 10% difference in the maximum attained value of principal strains between the experimental and numerical ones for all loading directions.

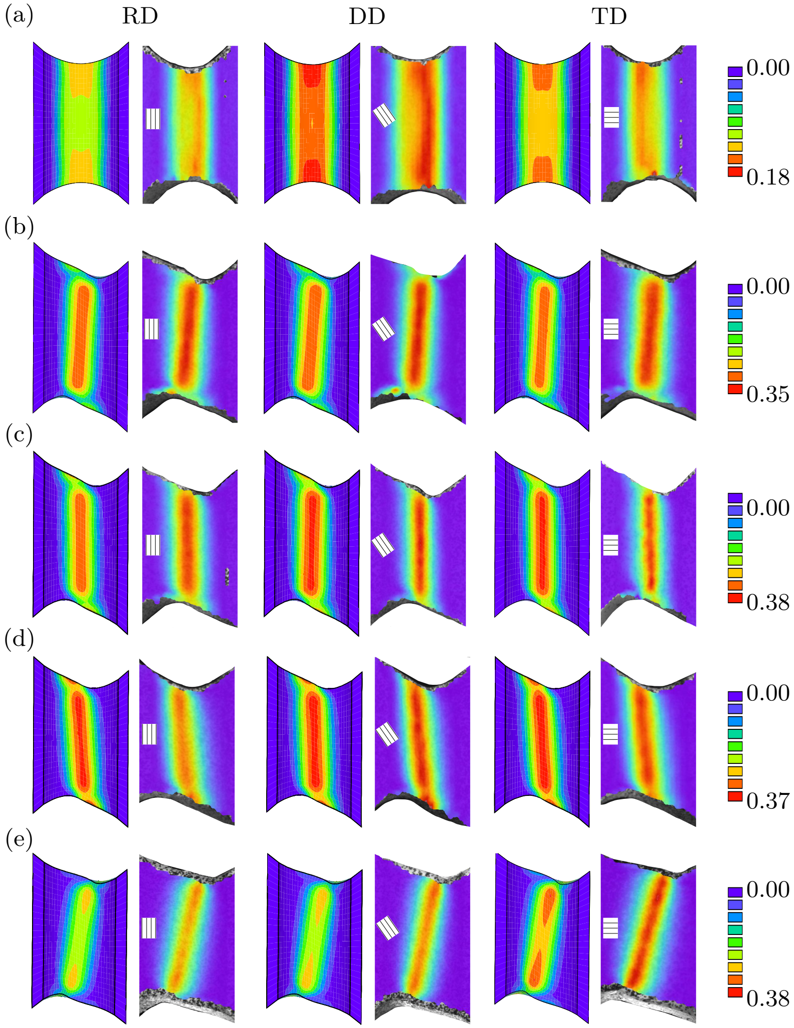

Figure 7.9: First principal strain fields from the DIC (right) and the numerical simulations (left), just before the final fracture for the load ratio (a) $F_1/F_2 = 0/1$, (b) $F_1/F_2 = 1/0$, (c) $F_1/F_2 = 1/0.5$, (d) $F_1/F_2 = 1/1$ and (e) $F_1/F_2 = 1/-1$.

Furthermore, the principal strains are almost vertically aligned for all the loading directions in case of load ratio $\mathrm{F}_1/\mathrm{F}_2 = 1/0.5$, which can be seen in Fig. 7.9(c). The principal strain bands are narrower for loading in DD and TD compared to those in RD. A_1 is nearly equal for DD and TD, reading 0.38, but is around 14% less for loading in RD. Again, the principal strain bands are numerically well reproduced and agree well to the principal strains obtained from DIC for all loading directions.

Moreover, for the load ratio $\mathrm{F}_1/\mathrm{F}_2 = 1/1$ (Fig. 7.9(d)), the principal strains are localized in small bands arranged diagonally from bottom right to top left with a width of about 2mm. In the case of loading in axis 1 in DD, the maxima are $A_1 = 0.36$, whereas A_1 reaches up to 0.35 and 0.32 for TD and RD, respectively. The values and the orientation of the principal strain bands are numerically well predicted for loading in DD and TD, while for RD, the numerical simulation overestimates the localized principal strain.

Similarly, Fig. 7.9(e) illustrates the principal strains for the load ratio $\mathrm{F}_1/\mathrm{F}_2 = 1/-1$. These strains are concentrated within very narrow bands, approximately 2mm in width, with a diagonal orientation of around 14° from the top left to the bottom right. For loading in TD, the maxima are $A_1 = 0.38$, while $A_1 = 0.35$ is reached for diagonal direction (DD). In the case of loading in RD, $A_1 = 0.32$ is measured shortly before the final failure of the specimen. Once again, the numerical simulation effectively replicates the principal strain bands, showcasing a close agreement with the principal strains acquired from DIC for all loading directions.

7.2.3 Stress-state

For the load ratio $\mathrm{F}_1/\mathrm{F}_2 = 0/1$ (Fig. 7.10(a)), higher gradients of the stress triaxiality can be seen in the cross section (C) of the notched part of the H-specimen, whereas η^{H} is relatively homogeneously distributed across the surface (S). The highest stress-state is obtained for loading in TD, where η^{H} reaches up to 1.1 at the center of the cross section. Conversely, on the boundaries of the cross section and on the surface, it is only 0.78. The stress triaxialities for RD and DD, in the cross section go up to 0.78 and 0.94, respectively. On the surface, η^{H} for loading in

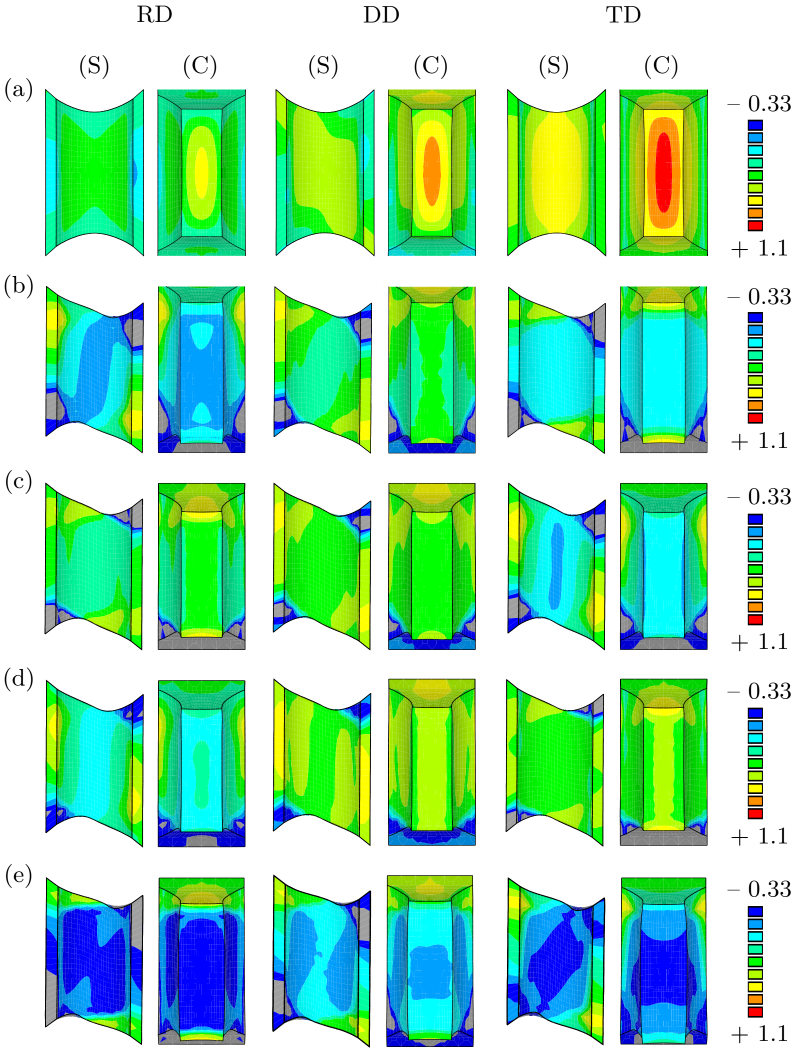

Figure 7.10: Stress triaxialities η^{H} for the load ratio (a) $F_1/F_2 = 0/1$, (b) $F_1/F_2 = 1/0$, (c) $F_1/F_2 = 1/0.5$, (d) $F_1/F_2 = 1/1$ and (e) $F_1/F_2 = 1/-1$.

RD and DD is 0.46 and 0.62, respectively.

Furthermore, the stress triaxiality for the load case $F_1/F_2 = 1/0$ is depicted in Fig. 7.10(b). η^{H} is nearly homogeneously distributed over the cross section, with small gradients on the bottom and the top. For loading in RD, η^{H} is nearly 0.00, signifying nearly a pure shear stress-state. In contrast, for loading in DD and TD, η^{H} is 0.14 and 0.30, respectively, indicating a small presence of hydrostatic stress. On the surface, for all the loading directions, the distribution and the values of stress triaxiality are nearly similar to that observed in the cross section. The effect of the specimen's orientation (RD, DD, or TD) on the stress triaxialities for this loading case is marginal when compared to the load case $F_1/F_2 = 0/1$.

Similarly, Fig. 7.10(c) illustrates the stress triaxiality for the load ratio $F_1/F_2 = 1/0.5$. Similar to the load case $F_1/F_2 = 1/0$, the distribution of the stress triaxiality is almost homogeneous over the cross section with slight gradients on the bottom and the top. For loading in RD and DD, η^{H} measures 0.46 in the cross-section. However, the numerical prediction yields a slightly lower value of $\eta^{\mathsf{H}} = 0.14$ in both the cross-section and on the surface after loading in TD. Influence of the loading direction is evident in this particular loading case, with notable variations between the loading directions (RD, DD, and TD).

For the load ratio $F_1/F_2 = 1/1$, the numerically predicted stress triaxiality is shown in Fig. 7.10(d). The distribution of the stress triaxiality in cross-section after loading in DD and TD is nearly identical with η^{H} measuring 0.62, which is typical value for the mixed loading (tension combined with shear loading). However, slightly lesser value of $\eta^{\mathsf{H}} = 0.46$ is numerically predicted at the center of the cross-section in RD.

In addition, in the case of $F_1/F_2 = 1/-1$ (Fig. 7.10(e)), the stress triaxialites in the cross-section for RD and TD are negative, reaching up to -0.33. Likewise, for both the loading directions (RD and TD), $\eta^{\mathsf{H}} = -0.33$ covers a significant portion of the surface. However, in DD, the value of stress triaxiality η^{H} at the center of the cross-section is -0.17 with slight gradients on the top and bottom. On the central part of the surface, the numerically predicted η^{H} is nearly 0.00. The observed values of stress triaxiality are typical for this kind of loading ratio (shear loading combined with compression), where the damage is caused by micro-shear cracks. The impact of the specimen's orientation with respect to the principal axes of anisotropy is evident.

7.2.4 Inelastic strains

Fig. 7.11(a) illustrates the equivalent plastic strains γ for the load ratio $F_1/F_2 = 0/1$ in the cross-section (C) and on the surface (s) of the notch of the H-specimen. The magnitude and distribution of γ are nearly similar in both the cross-section and on the surface is nearly similar after loading in DD and TD, reaching a maximum value of $\gamma = 0.22$. But, slightly lower value of $\gamma = 0.18$ is numerically predicted for loading in RD.
For the load ratio $F_1/F_2 = 1/0$ (Fig. 7.11(b)), very minimal differences are observed in γ between RD, DD and TD. In all cases, γ is more concentrated on the left and right edges of the cross-section with a maximum value of $\gamma = 0.40$. On the surface, it is localized forming a diagonal band from the top right to the bottom left.
Again, for the load ratio $F_1/F_2 = 1/0.5$ (Fig. 7.11(c)) the distribution of γ is almost the same for all loading cases, reaching $\gamma = 0.44$ and localized more at the either side of the edges of the cross-section. Similarly, on the surface, nearly vertical shear bands are formed after loading in RD, DD and TD. Furthermore, for the load ratio $F_1/F_2 = 1/1$ (Fig. 7.11(d)), the equivalent plastic strains in the corss-section for RD and TD are nearly homogeneously distributed with small gradients on the top and the bottom with γ reaching up to 0.35. But for DD, the numerical prediction shows the maximum value of $\gamma = 0.43$ among all the loading directions and is concentrated more towards the left and right edges of the cross-section. On the surface, for DD, localized shear bands with a width of about 4mm are formed, inclined from top left to the bottom right, whereas the shear bands are relatively narrower for RD and TD with the same inclination.
In addition, Fig. 7.11(e) displays the equivalent plastic strains for the load ratio $F_1/F_2 = 1/-1$. Across the cross-section, the distribution of γ for RD and TD is the same with its maximum value of 0.47 concentrated on both the left and the right edges. But for DD, γ measures less than that of RD and TD, with a value of 0.39 in the cross-section. Moreover, they form a localized shear bands diagonally orientated form top right to the bottom left making about 12° with the vertical axis. For TD, the shear bands are approximately 3mm wide, while but for RD and DD, they are slightly narrower.

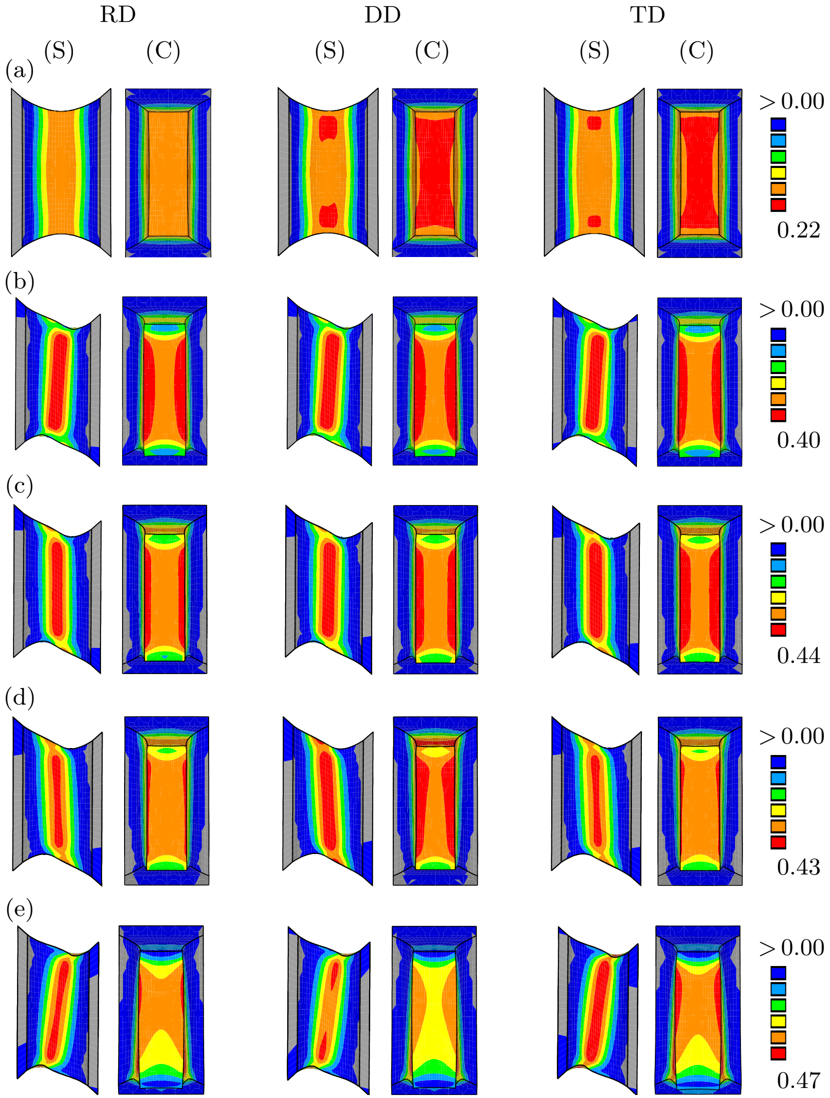

Figure 7.11: Equivalent plastic strains γ for the load raitos (a) $F_1/F_2 = 0/1$, (b) $F_1/F_2 = 1/0$, (c) $F_1/F_2 = 1/0.5$, (d) $F_1/F_2 = 1/1$ and (e) $F_1/F_2 = 1/-1$.

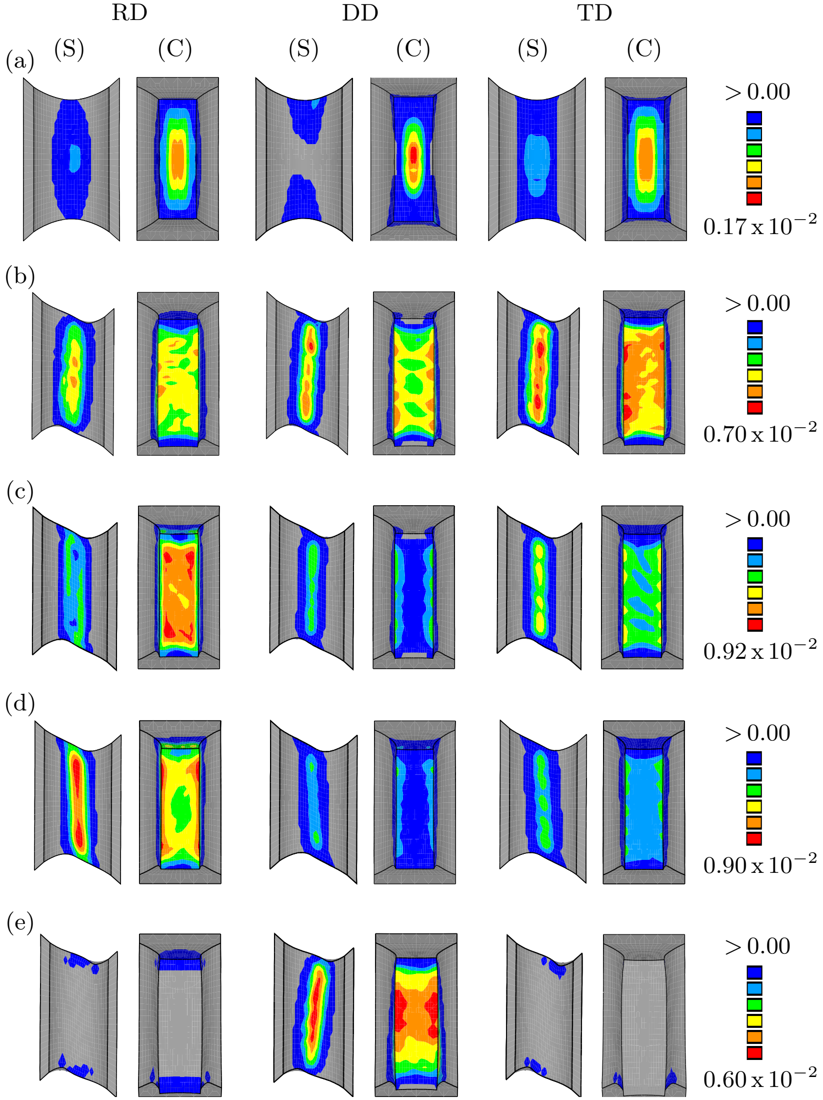

Figure 7.12: Equivalent damage strains μ for the load raitos (a) $F_1/F_2 = 0/1$, (b) $F_1/F_2 = 1/0$, (c) $F_1/F_2 = 1/0.5$, (d) $F_1/F_2 = 1/1$ and (e) $F_1/F_2 = 1/-1$.

The equivalent damage strains (μ) in the cross-section and on the surface of the notch of the H-specimen are depicted in Fig. 7.12. Particularly, for the load case $F_1/F_2 = 0/1$ (Fig. 7.12(a)), the equivalent damage strains appear to be initially concentrated at the center of the cross-section (C) and then gradually propagate across the cross-section, which is typical for tension-dominated loading. In the cross-section, the numerical predictions show a maximum $\mu = 0.17\%$ for DD, strongly localized at the center. In contrast, for RD and TD, although the maximum $\mu = 0.15\%$ is slightly lower than DD, it is more widespread across the center. On the surface, the distribution of μ is similar for RD and TD, forming a broad vertical band. However, for DD, μ is more concentrated on the top and bottom edges of the surface (S) of the notch.

For the load ratio $F_1/F_2 = 1/0$ (Fig. 7.12(b)), in all loading directions, the distribution of equivalent damage strains in the cross-section is not homogeneous, with strain gradients across the surface. The maximum $\mu = 0.70\%$ is observed for TD compared to others. Similarly, on the surface, a localized diagonally orientated shear band is formed, where the band for DD appears to be narrower than RD and TD.

For DD, the maximum value of μ is strongly concentrated towards the top edge of the surface, whereas for TD, the maximum μ is almost uniformly concentrated over the shear band. It is worth mentioning that, for this type of shear-dominated loading, the maximum equivalent damage strain always appears on the surface of the notch, unlike tension-dominated loading ($F_1/F_2 = 0/1$), where the maximum equivalent damage strain always develops at the center of the cross-section.

Furthermore, in the case of $F_1/F_2 = 1/0.5$, visible in Fig. 7.12(c), the equivalent damage strains on the surface form nearly a vertical narrow zone of shear band, with maximum $\mu = 0.46\%$ predicted after loading in TD. However, $\mu = 0.92\%$ is the maximum in the cross-section for loading in RD, while for DD, the numerically analyzed μ is around 0.60% lower than that of RD.

Again, similar to the previous loading case, for $F_1/F_2 = 1/1$ (Fig. 7.12(d)), the distribution of the equivalent damage strains in the cross-section is predicted to be maximum for loading in RD. For RD, μ reaches up to 0.90% and is more localized on the left and right side of the edges of the cross-section. A similar trend is observed for DD and TD, with the value of μ being around half of that for RD. On the surface, an inclined band of equivalent damage strain is formed for all the loading cases, running

from the top left to the bottom right. The maximum $\mu = 0.90\%$, localized on top and bottom part of the surface, is observed for loading in RD.
In addition, for the load ratio $\mathrm{F}_1/\mathrm{F}_2 = 1/{-1}$ (Fig. 7.12(e)), the equivalent damage strains are distributed throughout the surface of the cross-section for DD, with a maximum $\mu = 0.60\%$ among all others. For TD, damage is not predicted in the cross-section, whereas damage is predicted at both the edges of the surface of the notch where strong localized deformation is seen during the experiments. Similar predictions of the equivalent damage strains are observed after loading in RD, with μ reaching up to around 0.15%. However, for DD, a localized narrow shear band, which is diagonally oriented from top right to the bottom left, is formed with $\mu = 0.60\%$ on the surface of the notch.

7.2.5 SEM images and fracture behavior

The pictures of the fracture lines on the surface of the notch of the H-specimen are presented in Fig. 7.13 and Fig. 7.14. It is noteworthy that the black lines within a small box denote the rolling directions. Once again, the fracture lines correspond to the localized bands of the first principal strain (Fig. 7.9) evaluated at the end of the respective experiments and the numerical simulations. For the load ratio $\mathrm{F}_1/\mathrm{F}_2 = 0/1$ (Fig. 7.13(a)), vertical fracture lines with a cup-cone fracture mode are visible. This type of fracture mode occurs due to the excessive tensile-dominated loading. In the case of $\mathrm{F}_1/\mathrm{F}_2 = 1/0$ shown in Fig. 7.13(b), for all the loading directions, the fracture lines are inclined from top right to the bottom left, indicating a typical shear-dominated fracture mode. Furthermore, the fracture lines are slightly diagonally oriented from top left to the bottom right after loading in RD, DD and TD for the load ratio $\mathrm{F}_1/\mathrm{F}_2 = 1/0.5$ (Fig. 7.13(c)). In this case, the fracture lines are somewhat wider than the previous loading case and are clearly visible. In addition, for combined loading case (tension and shear) $\mathrm{F}_1/\mathrm{F}_2 = 1/1$ (Fig. 7.14(a)), the orientation of the fracture lines resembles the load ratio $\mathrm{F}_1/\mathrm{F}_2 = 1/0.5$, but they make a greater angle with the vertical axis and are more wider.

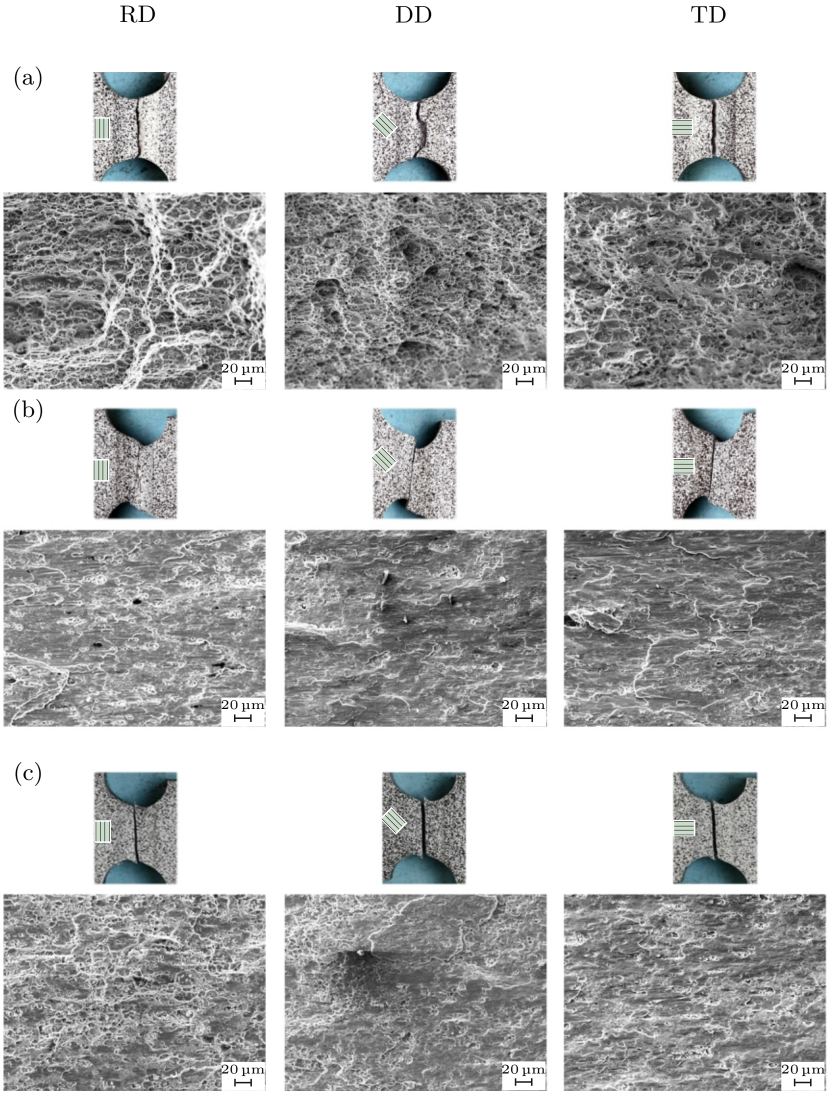

Figure 7.13: Fracture lines and the corresponding SEM images of the fracture surfaces for the load raitos (a) $F_1/F_2 = 0/1$, (b) $F_1/F_2 = 1/0$ and (c) $F_1/F_2 = 1/0.5$.

For the load ratio $F_1/F_2 = 1/-1$ (Fig. 7.14(b)), the fracture lines are diagonally oriented from bottom left to top right, which again is the indication of shear-dominated fracture mode. The experimental results clearly indicate that the fracture lines at the macroscopic level are influenced by the load ratios, while the impact of the loading direction (RD, DD, or TD) is marginal.

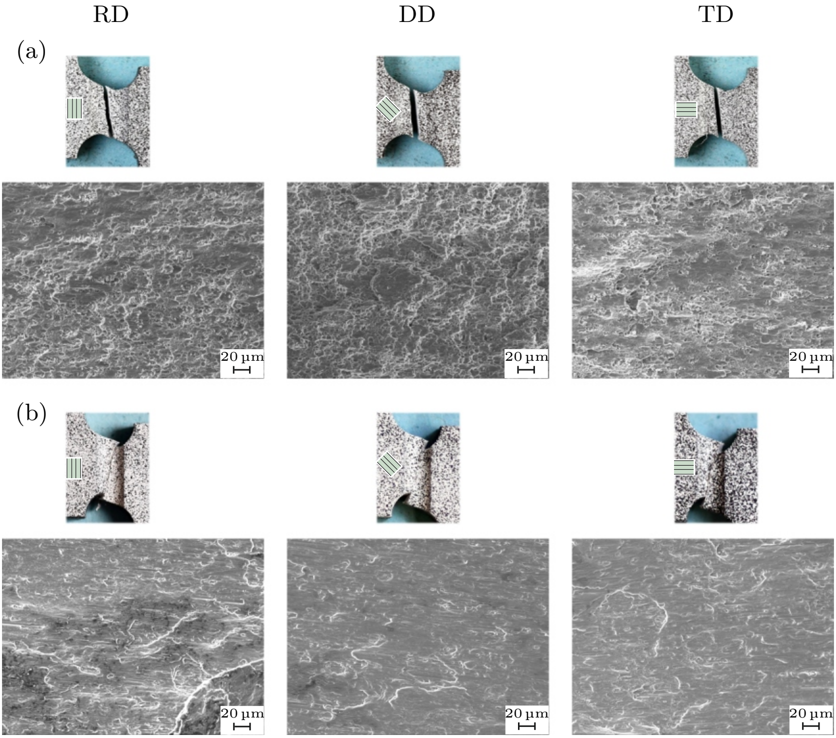

Figure 7.14: Fracture lines and the corresponding SEM images of the fracture surfaces for the load raitos (a) $F_1/F_2 = 1/1$ and (b) $F_1/F_2 = 1/0$ and (c) $F_1/F_2 = 1/-1$.

The micro-level analysis of the fracture surfaces using scanning electron microscopy (SEM) reveals distinct damage mechanisms, as illustrated in

Fig. 7.13 and Fig. 7.14. For example, for the load ratio $F_1/F_2 = 0/1$ (Fig. 7.13(a)) remarkable growth of the voids leading to larger pores and dimples are clearly visible after loading in RD, DD and TD. The fracture surfaces for RD and TD exhibit considerable similarity. However, for DD, while the voids and pores are smaller, there are some spots where the depth of the dimples appears to be shallower than that observed for RD and DD. This observation could provide an explanation for the distribution of the equivalent damage strain (μ) in the cross-section as shown in (Fig. 7.12(a)). In this case μ is maximum for DD and is strongly localized at the center, which might be due to the presence of the shallow dimples. Even though μ is slightly lower for RD and TD compared to DD, the equivalent damage strains exhibit greater dispersion around the center and across the cross-section, which is not observed in the case of DD.

For the load ratio $F_1/F_2 = 1/0$ (Fig. 7.13(b)), the SEM analysis reveals shear mechanisms with a few small voids leading to micro-shear cracks after loading in RD. Conversely, loading in DD and TD results in a reduced number of small sheared voids, accompanied by prominent shear mechanisms compared to RD, ultimately causing the failure of the specimen. The numerically predicted equivalent damage strains (Fig. 7.12(b)), both on the surface and in the cross-section, have higher values for DD and TD compared to RD. These numerical results are consistent with the SEM images, where micro-shear cracks are more dominant after loading in DD and TD than in RD.

In the case of the load ratio $F_1/F_2 = 1/0.5$, depicted in Fig. 7.13(c), numerous small voids are superimposed with shear mechanisms, leading to a higher number of sheared dimples. Compared to RD, the number of small voids combined with shear mechanisms resulting in sheared dimples is less after loading in DD and TD. Furthermore, the distribution of equivalent damage strains (Fig. 7.12(c)) aligns with these images of the fracture surface, as the equivalent damage strain for loading in RD has higher values across the cross-section than the other loading directions.

Moreover, for the load ratio $F_1/F_2 = 1/1$ (Fig. 7.14(a)), plenty of micro-voids are sheared resulting in shallow sheared dimples after loading in RD. For loading in DD, the size and number of micro-voids, combined with shear mechanisms leading to shallow sheared dimples, are less. Similarly, for loading in TD, only a few number of micro-voids, but remarkable micro-shear cracks develop with sheared dimples. The combination of micro-voids and shear mechanisms leading to the failure is typical for this type of loading. Once again, higher values of the equivalent damage strains (Fig. 7.12(d)), both in the cross-section and on the surface, are predicted for RD, which again align with the observation that a prominent combination of micro-voids and shear mechanisms is visible for RD compared to TD and DD.

In addition, in the case of $F_1/F_2 = 1/-1$ (Fig. 7.14(b)), for example, loading in RD shows some small voids that are sheared and superimposed by micro-shear-cracks. However, for DD, almost no presence of voids is observed and the failure is caused by the accumulation of micro-shear-cracks, leading to a very smooth and flat failure surface. Similarly, after loading in TD, only very few voids can be seen, which are sheared and superimposed by micro-shear-cracks. In the case of DD, pronounced shear mechanisms with fewer voids than in the case of RD and TD can be observed in the SEM pictures.

In summary, distribution, localization, and orientation of the principal strain bands are primarily influenced by the load ratio, whereas the orientation of the H-specimen during loading (RD, DD, or TD) affects the maximum values of the first principal strains. For nearly every load case, the value of the first principal strain is higher for loading in DD compared to those in RD and TD, suggesting that the specimens cut in DD exhibit a more ductile behavior than those in RD and TD. This is also visible in the load-displacement diagrams for most of the load ratios, as the displacement to the failure is more for the specimens loaded in DD compared to RD and TD. Additionally, the differences in the initial yield stress between the loading directions are also evident in the load-displacement diagram. The influence of loading directions on the fracture lines is not clearly evident, but the analysis of the fracture surface reveals a significant impact of the specimen's orientation on the damage and fracture mechanisms at the micro-scale. For instance, in all the examined load ratios, the presence and growth of voids are more pronounced after loading in the RD direction compared to other loading directions. Similarly, for the negative or nearly zero stress triaxialites, micro-shear cracks are more predominant after loading in DD than RD and TD. Furthermore, for nearly every examined load cases and specimens orientation, the distribution and magnitude of the equivalent plastic strains and equivalent damage strains from the numerical simulations align with the experimental results.

8 Conclusions and future works

8.1 Concluding remarks

The primary objective of this doctoral thesis is to explore the impact of plastic anisotropy on the damage and failure behavior of ductile metals through a combination of experimental investigations and corresponding numerical simulations. The study focuses on elucidating various damage mechanisms under diverse stress-states and loading directions, particularly concerning their orientation relative to the rolling direction. The analysis of experimental and numerical data highlights the intricate interplay of factors influencing the material's response. Additionally, three-dimensional micro-mechanical numerical analyses are conducted on unit-cells containing a micro-void to gain deeper insights into the complex stress-state and loading-direction-dependent damage behavior. The development of a novel experimental methodology is a significant contribution, providing a robust foundation for validating modeling approaches. Furthermore, the continuum damage model is adapted to incorporate the influence of plastic anisotropy on the damage behavior of aluminum alloy EN AW-2017A. This modified damage model serves as an efficient framework for numerically simulating the anisotropic behavior of materials, offering valuable insights for various engineering applications.

The anisotropic plastic behavior of the investigated material is modeled using the Hoffman yield criterion taking the strength-differential (SD) effect into account as has been observed in uniaxial tension and compression tests. The evolution of isochoric plastic strains is determined by Hill's plastic potential function, resulting in a non-associated flow rule. Generalized anisotropic stress invariants along with the generalized stress triaxiality and the generalized Lode parameter have been introduced based on the Hoffman yield criterion. Moreover, the Hoffman yield criterion is incorporated into the continuum damage model developed by Brünig [22, 24, 25], where the kinematic description of the damage is considered introducing the damage tensors. The damage condition for anisotropic ductile metals has been formulated in terms of the generalized stress invariants, where the weighting parameters are both stress-state and loading-direction dependent. Similarly, numerical simulations of the unit-cell containing a micro-void under different load ratios in different directions with respect to the rolling direction have been performed. This helps to understand the different damage and failure mechanisms acting on the micro-scale. The quasi-experimental results provide clear evidence of the impact of stress-state and loading-direction on damage evolution. Based on these findings, stress-state-dependent functions for the damage rule, which describe the development of macroscopic damage strains, have been proposed and parameters in the damage law are identified.

The constitutive equations of the continuum model are numerically integrated by an inelastic predictor-elastic corrector method and implemented in the FE program Ansys via user material subroutine (UMAT). To enhance the numerical accuracy of this explicit method, adjustments have been made in the estimation of the normalized deviator directions. Furthermore, distinct consistent tangent moduli corresponding to the numerical integration approach are explicitly provided to fulfill the demands of the global Newton-Raphson scheme.

From the experimental point of view, a series of experiments with uniaxially loaded tension/compression and shear specimens as well as with the biaxially loaded X0- and H-specimens are conducted. The experiments focus on different load ratios and loading directions with respect to the principal axes of anisotropy. The experimental results are then evaluated using the digital image correlation (DIC) and the global force-displacement diagrams as well as the local strain fields are determined. The biaxial loading experiments with X0- and H-specimens have shown that both the load ratios and the loading directions with respect to the rolling direction, have an impact on the magnitude of strains, the localization behavior, and the orientation of principal strain bands. Additionally, the fractured surfaces are analyzed with scanning electron microscopy (SEM). The pictures from SEM reveal that the damage and fracture processes at the micro-level are influenced by the load ratio and loading direction. Loading in DD results in more pronounced micro-shear-crack mechanisms, while loading in the RD exhibits more sheared voids. Similarly, the specimens in DD are more ductile in behavior than those in RD and TD.

Moreover, by utilizing the results obtained from uniaxially loaded tension/compression and shear tests, the Lankford coefficients (or r-values) and the yield stresses for specimens cut in the rolling direction (RD), transverse direction (TD), and diagonal direction (DD) are determined. A combined method is proposed, incorporating both the r-values and the yield stresses to identify anisotropic material parameters. This method demonstrates improved accuracy in the numerical prediction of both yield stresses and r-values for specimens with different loading directions compared to using only yield stresses or Lankford coefficients.

8.2 Future works

The results of this work demonstrate that the proposed modified continuum damage model is capable of capturing the damage and failure behavior of anisotropic ductile metals. However, there are opportunities for further enhancement of the damage model in the future and some of them are listed below:

- For instance, in addition to plastic anisotropy, the dependence of damage and failure behavior on the loading path or loading history can be further explored. Experiments on the investigated aluminum alloy, specifically focusing on non-proportional loading, such as shear to tension or tension to shear, should be conducted. Subsequently, the damage model can be refined to incorporate the damage behavior of anisotropic material under different loading paths, providing a valuable foundation for industrial applications.
- The effectiveness of the enhanced continuum model to characterize the damage behavior for other ductile metals like steel or titanium can be further investigated.
- Additionally, integrating other advanced yield criteria to account for plastic anisotropic behavior into the damage model and comparing their performance with the current numerical simulation results can provide additional validation and strengthen the findings of this study. Moreover, there are opportunities for enhancing numerical integration methods, making implementation more user-friendly for better understanding by different users. Furthermore, considering a non-local material formulation could be contemplated.

Bibliography

[1] M. Achouri, G. Germain, P. Dal Santo, and D. Saidane. “Experimental characterization and numerical modeling of micromechanical damage under different stress states”. *Materials & Design* 50 (2013), 207–222.

[2] L. Anand and W. A. Spitzig. “Initiation of localized shear bands in plane strain”. *Journal of the Mechanics and Physics of Solids* 28 (1980), 113–128.

[3] F. M. Andrade Pires, J. César de Sá, L. Costa Sousa, and R. M. Natal Jorge. “Numerical modelling of ductile plastic damage in bulk metal forming”. *International Journal of Mechanical Sciences* 45 (2003), 273–294.

[4] Ansys, Inc. “ANSYS USER Material Subroutine USERMAT”. *ANSYS USER Material Subroutine USERMAT* (1999).

[5] Ansys, Inc. “ANSYS Mechanical APDL Theory Reference 15.0”. *ANSYS Mechanical APDL Theory Reference* (2013).

[6] H. Aretz. “Numerical analysis of diffuse and localized necking in orthotropic sheet metals”. *International Journal of Plasticity* 23 (2007), 798–840.

[7] H. Badreddine and K. Saanouni. “On the full coupling of plastic anisotropy and anisotropic ductile damage under finite strains”. *International Journal of Damage Mechanics* 26 (2017), 1080–1123.

[8] H. Badreddine, K. Saanouni, and A. Dogui. “On non-associative anisotropic finite plasticity fully coupled with isotropic ductile damage for metal forming”. *International Journal of Plasticity* 26 (2010), 1541–1575.

[9] Y. Bai and T. Wierzbicki. “A new model of metal plasticity and fracture with pressure and Lode dependence”. *International Journal of Plasticity* 24 (2008), 1071–1096.

[10] Y. Bao and T. Wierzbicki. “On fracture locus in the equivalent strain and stress triaxiality space”. *International Journal of Mechanical Sciences* 46 (2004), 81–98.

[11] Y. Bao and T. Wierzbicki. “On the cut-off value of negative triaxiality for fracture”. *Engineering Fracture Mechanics* 72 (2005), 1049–1069.

[12] F. Barlat, H. Aretz, J. W. Yoon, M. E. Karabin, et al. “Linear transfomation-based anisotropic yield functions”. *International J-ournal of Plasticity* 21 (2005), 1009–1039.

[13] I. Barsoum and J. Faleskog. “Micromechanical analysis on the influence of the Lode parameter on void growth and coalescence”. *International Journal of Solids and Structures* 48 (2011), 925–938.

[14] K.-J. Bathe. *Finite element procedures.* 2nd ed. Englewood Cliffs, N.J: Prentice-Hall, 2014.

[15] A. A. Benzerga and J. Besson. “Plastic potentials for anisotropic porous solids”. *European Journal of Mechanics - A/Solids* 20 (2001), 397–434.

[16] J. Betten. “Damage tensors in continuum mechanics”. *Journal de Mécanique Théorique et Appliquée* 2 (1983), 13–32.

[17] J.-P. Boehler, ed. *Mechanical Behavior of Anisotropic Solids/Comportment Méchanique des Solides Anisotropes.* Springer Netherlands, 1983.

[18] N. Bonora. “A nonlinear CDM model for ductile failure”. *Engineering Fracture Mechanics* 58 (1997), 11–28.

[19] N. Bonora, D. Gentile, A. Pirondi, and G. Newaz. “Ductile damage evolution under triaxial state of stress: theory and experiments”. *International Journal of Plasticity* 21 (2005), 981–1007.

[20] M. Brünig. “Large strain elastic-plastic theory and nonlinear finite element analysis based on metric transformation tensors”. *Computational Mechanics* 24 (1999), 187–196.

[21] M. Brünig. “Numerical simulation of the large elastic–plastic deformation behavior of hydrostatic stress-sensitive solids”. *International Journal of Plasticity* 15 (1999), 1237–1264.

[22] M. Brünig. “A framework for large strain elastic–plastic damage mechanics based on metric transformations”. *International Journal of Engineering Science* 39 (2001), 1033–1056.

[23] M. Brünig. “Numerical analysis and elastic–plastic deformation behavior of anisotropically damaged solids”. *International Journal of Plasticity* 18 (2002), 1237–1270.

[24] M. Brünig. “An anisotropic ductile damage model based on irreversible thermodynamics”. *International Journal of Plasticity* 19 (2003), 1679–1713.

[25] M. Brünig. “Numerical analysis of anisotropic ductile continuum damage”. *Computer Methods in Applied Mechanics and Engineering* 192 (2003), 2949–2976.

[26] M. Brünig, D. Albrecht, and S. Gerke. “Modeling of ductile damage and fracture behavior based on bifferent micromechanisms”. *International Journal of Damage Mechanics* 20 (2011), 558–577.

[27] M. Brünig, D. Brenner, and S. Gerke. “Modeling of Stress-State-Dependent Damage and Failure of Ductile Metals”. *Applied Mechanics and Materials* 784 (2015), 35–42.

[28] M. Brünig, D. Brenner, and S. Gerke. “Stress state dependence of ductile damage and fracture behavior: experiments and numerical simulations”. *Engineering Fracture Mechanics* 141 (2015), 152–169.

[29] M. Brünig, O. Chyra, D. Albrecht, L. Driemeier, and M. Alves. “A ductile damage criterion at various stress triaxialities”. *International Journal of Plasticity* 24 (2008), 1731–1755.

[30] M. Brünig, S. Gerke, and V. Hagenbrock. “Micro-mechanical studies on the effect of the stress triaxiality and the Lode parameter on ductile damage”. *International Journal of Plasticity* 50 (2013), 49–65.

[31] M. Brünig, S. Gerke, and V. Hagenbrock. “Stress-state-dependence of damage strain rate tensors caused by growth and coalescence of micro-defects”. *International Journal of Plasticity* 63 (2014), 49–63.

[32] M. Brünig, S. Gerke, and S. Koirala. “Biaxial experiments and numerical analysis on stress-state-dependent damage and failure behavior of the anisotropic aluminum alloy EN AW-2017A”. *Metals* 11 (2021), 1214.

[33] M. Brünig, S. Gerke, and M. Schmidt. “Biaxial experiments and phenomenological modeling of stress-state-dependent ductile damage and fracture”. *International Journal of Fracture* 200 (2016), 63–76.

[34] M. Brünig, S. Gerke, and M. Schmidt. “Damage and failure at negative stress triaxialities: experiments, modeling and numerical simulations”. *International Journal of Plasticity* 102 (2018), 70–82.

[35] M. Brünig, S. Gerke, and M. Zistl. “Einfluss nicht-proportionaler Lastpfade auf das Schädigungs- und Versagensverhalten duktiler Metalle”. *DVM-Bericht* 250 (2018), 19–28.

[36] M. Brünig, S. Gerke, and M. Zistl. “Experiments and numerical simulations with the H-specimen on damage and fracture of ductile metals under non-proportional loading paths”. *Engineering Fracture Mechanics* 217 (2019), 106531.

[37] M. Brünig, S. Koirala, and S. Gerke. “Analysis of damage and failure in anisotropic ductile metals based on biaxial experiments with the H-specimen”. *Experimental Mechanics* 62 (2022), 183–197.

[38] M. Brünig, S. Koirala, and S. Gerke. “A stress-state-dependent damage criterion for metals with plastic anisotropy”. *International Journal of Damage Mechanics* (2023), 811–832.

[39] M. Brünig, M. Zistl, and S. Gerke. “Biaxial experiments on characterization of stress-state-dependent damage in ductile metals”. *Production Engineering* 14 (2020), 87–93.

[40] M. Brünig, M. Zistl, and S. Gerke. “Analysis of Damage and Fracture Mechanisms in Steel Sheets: Biaxial Experiments and Numerical Simulations”. In: *NUMISHEET 2022*. Ed. by K. Inal, J. Levesque, M. Worswick, and C. Butcher. The Minerals, Metals & Materials Series. Cham: Springer International Publishing, 2022, 423–431.

[41] L. E. Bryhni Dæhli, J. Faleskog, T. Børvik, and O. S. Hopperstad. “Unit cell simulations and porous plasticity modelling for strongly anisotropic FCC metals”. *European Journal of Mechanics - A/Solids* 65 (2017), 360–383.

[42] C. L. Chow and J. Wang. “An anisotropic theory of continuum damage mechanics for ductile fracture”. *Engineering Fracture Mechanics* 27 (1987), 547–558.

[43] C. L. Chow and J. Wang. “A finite element analysis of continuum damage mechanics for ductile fracture”. *International Journal of Fracture* 38 (1988), 83–102.

[44] J. P. Cordebois and F. Sidoroff. “Damage induced elastic anisotropy”. In: *Mechanical Behavior of Anisotropic Solids / Comportment Méchanique des Solides Anisotropes*. Ed. by J.-P. Boehler. Vol. 2. Dordrecht: Springer Netherlands, 1983, 761–774.

[45] E. de Souza Neto, D. Perić, and D. Owen. “A model for elastoplastic damage at finite strains: algorithmic issues and applications.” *Engineering Computations* 11 (1994), 257–281.

[46] Deutsches Institut für Normung e. V. *DIN EN ISO 10113:2021-06, Metallische Werkstoffe - Blech und Band - Bestimmung der senkrechten Anisotropie; Deutsche Fassung EN ISO 10113:2020*. Berlin.

[47] I. Doghri. “Numerical implementation and analysis of a class of metal plasticity models coupled with ductile damage”. *International Journal for Numerical Methods in Engineering* 38 (1995), 3403–3431.

[48] G. U. Fonseka and D. Krajcinovic. “The continuous damage theory of brittle materials, part 2: uniaxial and plane response modes”. *Journal of Applied Mechanics* 48 (1981), 816–824.

[49] X. Gao, T. Wang, and J. Kim. “On ductile fracture initiation toughness: effects of void volume fraction, void shape and void distribution”. *International Journal of Solids and Structures* 42 (2005), 5097–5117.

[50] S. Gerke. “Damage and fracture of ductile metals under dynamic loading conditions”. Universität der Bundeswehr München, 2013.

[51] S. Gerke, P. Adulyasak, and M. Brünig. “New biaxially loaded specimens for the analysis of damage and fracture in sheet metals”. *International Journal of Solids and Structures* 110-111 (2017), 209–218.

[52] J. I. Goldstein, D. E. Newbury, J. R. Michael, N. W. Ritchie, et al. *Scanning Electron Microscopy and X-Ray Microanalysis*. 4th ed. 2018. New York, NY: Springer New York, 2018.

[53] M. Gologanu, J.-B. Leblond, and J. Devaux. “Approximate models for ductile metals containing non-spherical voids—Case of axisymmetric prolate ellipsoidal cavities”. *Journal of the Mechanics and Physics of Solids* 41 (1993), 1723–1754.

[54] M. Gologanu, J.-B. Leblond, and J. Devaux. “Approximate Models for Ductile Metals Containing Nonspherical Voids—Case of Axisymmetric Oblate Ellipsoidal Cavities”. *Journal of Engineering Materials and Technology* 116 (1994), 290–297.

[55] A. L. Gurson. “Continuum theory of ductile rupture by void nucleation and growth: part I—yield criteria and flow rules for porous ductile media”. *Journal of Engineering Materials and Technology* 99 (1977), 2–15.

[56] V. Hagenbrock. “Ein Kontinuumsschädigungsmodell basierend auf mikromechanischen numerischen Berechnungen”. Universität der Bundeswehr München, 2016.

[57] R. Hill. “A theory of the yielding and plastic flow of anisotropic metals”. *Proceedings of the Royal Society of London. Series A. Mathematical and Physical Sciences* 193 (1948), 281–297.

[58] O. Hoffman. “The brittle strength of orthotropic materials”. *Journal of Composite Materials* 1 (1967), 200–206.

[59] W. F. Hosford. *The mechanics of crystals and textured polycrystals*. Vol. 32. Oxford Engineering Science Series. New York: Oxford Univ. Press, 1993.

[60] A. Hosokawa, D. S. Wilkinson, J. Kang, and E. Maire. “Effect of triaxiality on void growth and coalescence in model materials investigated by X-ray tomography”. *Acta Materialia* 60 (2012), 2829–2839.

[61] N. Hosseini, J. C. Nieto-Fuentes, M. Dakshinamurthy, J. A. Rodríguez-Martínez, and G. Vadillo. “The effect of material orientation on void growth”. *International Journal of Plasticity* 148 (2022), 103149.

[62] J. Huang, Y. Jiang, F. Jiang, and C. Xu. “The Improved Mechanical Anisotropy of a Commercial Al–Cu–Mg–Mn–Si (2017) Aluminum Alloy by Cross rolling”. *Advanced Engineering Materials* 24 (2022), 863.

[63] T. J. R. Hughes. “Numerical Implementation of Constitutive Models: Rate-Independent Deviatoric Plasticity”. In: *Theoretical foundation for large-scale computations for nonlinear material behavior.* Ed. by S. Nemat-Nasser, R. J. Asaro, and G. A. Hegemier. Vol. 48. Dordrecht: Springer Netherlands, 1984, 29–63.

[64] T. J. Hughes and K. S. Pister. “Consistent linearization in mechanics of solids and structures”. *Computers & Structures* 8 (1978), 391–397.

[65] B. Hutchinson. “Critical Assessment 16: Anisotropy in metals”. *Materials Science and Technology* 31 (2015), 1393–1401.

[66] L. M. Kachanov. “On rupture time under condition of creep”. *Otd. Techn. Nauk* 8 (1958), 26–31.

[67] L. M. Kachanov. “Continuum model of medium with cracks”. *Journal of Engineering Mechanics Division* 106 (1980), 1039–1051.

[68] S. M. Keralavarma and A. A. Benzerga. “A constitutive model for plastically anisotropic solids with non-spherical voids”. *Journal of the Mechanics and Physics of Solids* 58 (2010), 874–901.

[69] S. M. Keralavarma and A. A. Benzerga. “An approximate yield criterion for anisotropic porous media”. *Comptes Rendus. Mécanique* 336 (2008), 685–692.

[70] J. Kim, X. Gao, and T. S. Srivatsan. “Modeling of crack growth in ductile solids: a three-dimensional analysis”. *International Journal of Solids and Structures* 40 (2003), 7357–7374.

[71] D. Krajcinovic. “Constitutive equations for damaging materials”. *Journal of Applied Mechanics* 50 (1983), 355–360.

[72] R. D. Krieg and D. B. Krieg. “Accuracies of Numerical Solution Methods for the Elastic-Perfectly Plastic Model”. *Journal of Pressure Vessel Technology* 99 (1977), 510–515.

[73] W. T. Lankford, S. C. Snyder, and J. A. Bausher. “New criteria for predicting the press performance of deep drawing sheets”. *Trans. ASM* (1950), 1197–1205.

[74] T. Lehmann. “Some thermodynamical considerations on inelastic deformations including damage processes”. *Acta Mechanica* 79 (1989), 1–24.

[75] T. Lehmann. “Thermodynamical foundations of large inelastic deformations of solid bodies including damage”. *International Journal of Plasticity* 7 (1991), 79–98.

[76] J. Lemaitre. “A continuous damage mechanics model for ductile fracture”. *Journal of Engineering Materials and Technology* 107 (1985), 83–89.

[77] J. Lemaitre. *A Course on Damage Mechanics.* Springer, Berlin, 1996.

[78] J. Lemaitre and J. Dufailly. “Damage measurements”. *Engineering Fracture Mechanics* 28 (1987), 643–661.

[79] J. Lian, F. Shen, X. Jia, D.-C. Ahn, et al. “An evolving non-associated Hill48 plasticity model accounting for anisotropic hardening and r-value evolution and its application to forming limit prediction”. *International Journal of Solids and Structures* 151 (2018), 20–44.

[80] E. Maire, S. Zhou, J. Adrien, and M. Dimichiel. “Damage quantification in aluminium alloys using in situ tensile tests in X-ray tomography”. *Engineering Fracture Mechanics* 78 (2011), 2679–2690.

[81] A. MAY. “On the origins of the anisotropic mechanical behaviour of extruded AA2017 aluminium alloy”. *Bulletin of Materials Science* 40 (2017), 395–406.

[82] F. A. McClintock. “A Criterion for Ductile Fracture by the Growth of Holes”. *Journal of Applied Mechanics* 35 (1968), 363–371.

[83] L. Morin, J.-B. Leblond, and D. Kondo. “A Gurson-type criterion for plastically anisotropic solids containing arbitrary ellipsoidal voids”. *International Journal of Solids and Structures* 77 (2015), 86–101.

[84] L. Morin, J.-B. Leblond, D. Mohr, and D. Kondo. “Prediction of shear-dominated ductile fracture in a butterfly specimen using a model of plastic porous solids including void shape effects”. *European Journal of Mechanics - A/Solids* 61 (2017), 433–442.

[85] S. Murakami. “Mechanical modeling of material damage”. *Journal of Applied Mechanics* 55 (1988), 280–286.

[86] K. Nahshon and J. W. Hutchinson. “Modification of the Gurson model for shear failure”. *European Journal of Mechanics - A/Solids* 27 (2008), 1–17.

[87] A. Needleman. “Void Growth in an Elastic-Plastic Medium”. *Journal of Applied Mechanics* 39 (1972), 964–970.

[88] S. Nemat-Nasser and Y.-F. Li. “A new explicit algorithm for finite-deformation elastoplasticity and elastoviscoplasticity: Performance evaluation”. *Computers & Structures* 44 (1992), -937–963.

[89] T. Nicholas. *High cycle fatigue: A mechanics of materials perspective.* Elsevier, Amsterdam, 2006.

[90] N. Park, H. Huh, and J. W. Yoon. “Anisotropic fracture forming limit diagram considering non-directionality of the equi-biaxial fracture strain”. *International Journal of Solids and Structures* 151 (2018), 181–194.

[91] Peng, Wang, Dai, Liu, and Zhang. “Effect of stress triaxiality on plastic damage evolution and failure mode for 316L notched specimen”. *Metals* 9 (2019), 1067.

[92] A. Pineau, A. A. Benzerga, and T. Pardoen. “Failure of metals I: brittle and ductile fracture”. *Acta Materialia* 107 (2016), 424–483.

[93] K. E. Puttick. “Ductile fracture in metals”. *Philosophical Magazine* 4 (1959), 964–969.

[94] Y. N. Rabotnov. “Paper 68: On the Equation of State of Creep”. *Proceedings of the Institution of Mechanical Engineers, Conference Proceedings* 178 (1963), 117–122.

[95] J. R. Rice and D. M. Tracey. “On the ductile enlargement of voids in triaxial stress fields”. *Journal of the Mechanics and Physics of Solids* 17 (1969), 201–217.

[96] F. Rickhey and S. Hong. “Stress Triaxiality in Anisotropic Metal Sheets-Definition and Experimental Acquisition for Numerical Damage Prediction”. *Materials* 15 (2022).

[97] C. C. Roth, T. F. Morgeneyer, Y. Cheng, L. Helfen, and D. Mohr. “Ductile damage mechanism under shear-dominated loading: In-situ tomography experiments on dual phase steel and localization analysis”. *International Journal of Plasticity* 109 (2018), 169–192.

[98] G. Rousselier. “Ductile fracture models and their potential in local approach of fracture”. *Nuclear Engineering and Design* 105 (1987), 97–111.

[99] K. Saï, L. Taleb, and G. Cailletaud. “Numerical simulation of the anisotropic behavior of 2017 aluminum alloy”. *Computational Materials Science* 65 (2012), 48–57.

[100] J. C. Simo and R. L. Taylor. “Consistent tangent operators for rate-independent elastoplasticity”. *Computer Methods in Applied Mechanics and Engineering* 48 (1985), 101–118.

[101] W. A. Spitzig and O. Richmond. “The effect of pressure on the flow stress of metals”. *Acta Metallurgica* 32 (1984), 457–463.

[102] W. A. Spitzig, R. E. Smelser, and O. Richmond. “The evolution of damage and fracture in iron compacts with various initial porosities”. *Acta Metallurgica* 36 (1988), 1201–1211.

[103] W. A. Spitzig, R. J. Sober, and O. Richmond. “Pressure dependence of yielding and associated volume expansion in tempered martensite”. *Acta Metallurgica* 23 (1975), 885–893.

[104] W. Suaris and S. P. Shah. “Rate–sensitive damage theory for brittle solids”. *Journal of Engineering Mechanics* 110 (1984), 985–997.

[105] M. A. Sutton. “Digital Image Correlation for Shape and Deformation Measurements”. In: *Springer Handbook of Experimental Solid Mechanics.* Ed. by W. N. Sharpe. Springer Handbooks. Boston, MA: Springer US, 2008, 565–600.

[106] W. H. Tai and B. X. Yang. “A new microvoid-damage model for ductile fracture”. *Engineering Fracture Mechanics* 25 (1986), 377–384.

[107] H. Talebi-Ghadikolaee, H. Moslemi Naeini, M. J. Mirnia, M. A. Mirzai, et al. “Experimental and numerical investigation of failure during bending of AA6061 aluminum alloy sheet using the modified Mohr-Coulomb fracture criterion”. *The International Journal of Advanced Manufacturing Technology* 105 (2019), 52-17–5237.

[108] T. Tancogne-Dejean, C. C. Roth, T. F. Morgeneyer, L. Helfen, and D. Mohr. “Ductile damage of AA2024-T3 under shear loading: Mechanism analysis through in-situ laminography”. *Acta Materialia* 205 (2021), 116556.

[109] A. E. Tekkaya, P.-O. Bouchard, S. Bruschi, and C. C. Tasan. “Damage in metal forming”. *CIRP Annals - Manufacturing Technology* 69 (2020), 600–623.

[110] V. Tvergaard. “On localization in ductile materials containing spherical voids”. *International Journal of Fracture* 18 (1982), 237–252.

[111] V. Tvergaard. “Material failure by void growth to coalescence”. *Advances in Applied Mechanics* 27 (1989), 83–151.

[112] V. Tvergaard. “Behaviour of voids in a shear field”. *International Journal of Fracture* 158 (2009), 41–49.

[113] V. Tvergaard. “Effect of stress-state and spacing on voids in a shear-field”. *International Journal of Solids and Structures* 49 (2012), 3047–3054.

[114] E. Voce. “A practical strain-hardening function”. *Metallurgia* 51 (1955), 219–226.

[115] A. Weck and D. S. Wilkinson. “Experimental investigation of void coalescence in metallic sheets containing laser drilled holes”. *Acta Materialia* 56 (2008), 1774–1784.

[116] Z. Wei, M. Zistl, S. Gerke, and M. Brünig. “Analysis of ductile damage and fracture under reverse loading”. *International Journal of Mechanical Sciences* (2022), 107476.

[117] J. Wen, Y. Huang, K. C. Hwang, C. Liu, and M. Li. “The modified Gurson model accounting for the void size effect”. *International Journal of Plasticity* 21 (2005), 381–395.

[118] M. L. Wilkins. “Calculation of elastic-plastic flow”. *Methods in Computational Physics* 3 (1964), 211–262.

[119] C. D. Wilson. “A critical reexamination of classical metal plasticity”. *Journal of Applied Mechanics* 69 (2002), 63–68.

[120] L. Xue. “Constitutive modeling of void shearing effect in ductile fracture of porous materials”. *Engineering Fracture Mechanics* 75 (2008), 3343–3366.

[121] O. C. Zienkiewicz and R. L. Taylor. *The Finite Element Method.* Vol. 1. Butterworth-Heinemann, Oxford, 2002.

[122] M. Zistl. “Modellbildung und experimentell-numerische Untersuchungen zur Schädigung und zum Versagen duktiler Metalle unter nichtproportionaler Belastung”. Universität der Bundeswehr München, 2022.